Metasurfaces for bioimaging

Antu Nehuen Gortari

NNT : 2019SACLS416

Thèse de doctorat

Metasurfaces for bioimaging

Thèse de doctorat de l'Université Paris-Saclay
préparée à l'Université Paris-Sud au C2N

Ecole doctorale n°572 Ecole Doctorale Ondes et Matière (EDOM)
Spécialité de doctorat : Physique

Thèse présentée et soutenue à Palaiseau, le 15/11/2019, par

ANTU NEHUEN GORTARI

Composition du Jury :

Nathalie Westbrook PR, Institut d'Optique (Palaiseau)	Président
Anne Sentenac Directrice de Recherche CNRS, Institut Fresnel (Marseille)	Rapporteur
Gilles Tessier Professor, Institut de la Vision (Paris)	Rapporteur
Jörg Enderlein Professor, Gottingen University (Allemagne)	Examinateur
Patrice Genevet Chercheur CNRS, CRHEA (Nice)	Examinateur
Alejandro Giacomotti Chercheur CNRS, C2N (Palaiseau)	Directeur de thèse
Sophie Bouchoule Directrice de recherche CNRS, C2N (Palaiseau)	Co-directrice de thèse

Acknowledgments

This thesis would not have been possible if it wasn't for the support, help and guidance provided by many people. From the very beginning, I would like to thank my supervisor *Alejandro Giacomotti* for giving me the opportunity to participate in this wonderful collaborative project along with the trust he put on me and my abilities. His valuable support and advice, specially on several key moments were undoubtedly essential for the results we got. When I was not in the lab or running simulations, I was dealing with nanofabrication challenges and that would have been close to unfathomable without *Sophie Bouchoule*. For me she's the definition of 'hard-working' and 'knowledgeable' and I cannot thank enough how she managed to find time for me in one of the busiest of schedules. During my clean-room time, I also received plenty of support, time and teaching by *Edmond Cambril* and *Andrea Cattoni*, with their input visible in each of the samples we fabricated. When it came to put our samples to the test, I also found unvaluable support by *Jörg Enderlein* and his group, in particular *Soheil Mojiri* and *Oleksii Nevskyi*. The biological samples, conceived and perfectly prepared by *Florian Rehfeldt* and *Lara Hauke*, played a significant role in this work and for that I'm also very grateful. And then, there is all the people that not only helped me in several occasions but who simply by being there made this journey way more enjoyable: *Avishek Chowdhury* (I hope I have your name right), *Rui Zhu*, *Quentin Chateiller*, *Guilhem Madiot*, *Anirudh Pammi*, *Raul Quiñonez Uribe*, *Tommaso Alterini*, *Ana Rodriguez*, *Donatus Halpaap*, *Mariano Gonzalez Pisfil* and the list goes on.. colleagues from the lab and the project that quickly became friends and made all the difference. I would also use this space to thank the Argentinian State for providing me and many others with high quality free public education at all levels. I believe that the importance of accessible public education cannot be overstated, and that our current system should be protected and continuously improved, as it has been and still is one of the most important elements for promoting the development of the country and ensuring that the majority of its population has equal opportunities of social mobility and improving their quality of life. In this context, la Maison de l'Argentine in Paris is a great example of this support. There I found a welcoming and warm environment, which served as a home and helped me and other students, artists and academics to continue to develop our careers in a new and different environment. Sadly, since the year 2017 and under the direction of Juan Manuel Corvalan Espina, the residence has been undergoing a rapid and steady decline, and the welcoming environment I had first found became authoritarian, oppressive, and outright hostile towards the residents. I'm convinced this space can and should play an important and positive role in the careers of its residents. I'm grateful for the place I had there and I sincerely hope the Argentinian House will soon recover the nurturing atmosphere it had when I first arrived and needs so much in order to fulfill its mission. Last but not least, my parents, my brother, my girlfriend and my old and new friends were all enormously important these few years, I want to give a big hug to everyone. Big thanks to Mullero too, for his corrections on my manuscript.

Contents

Chapter 1

Introduction

1.1 Total Internal Reflection Fluorescence Microscopy (TIRFM)

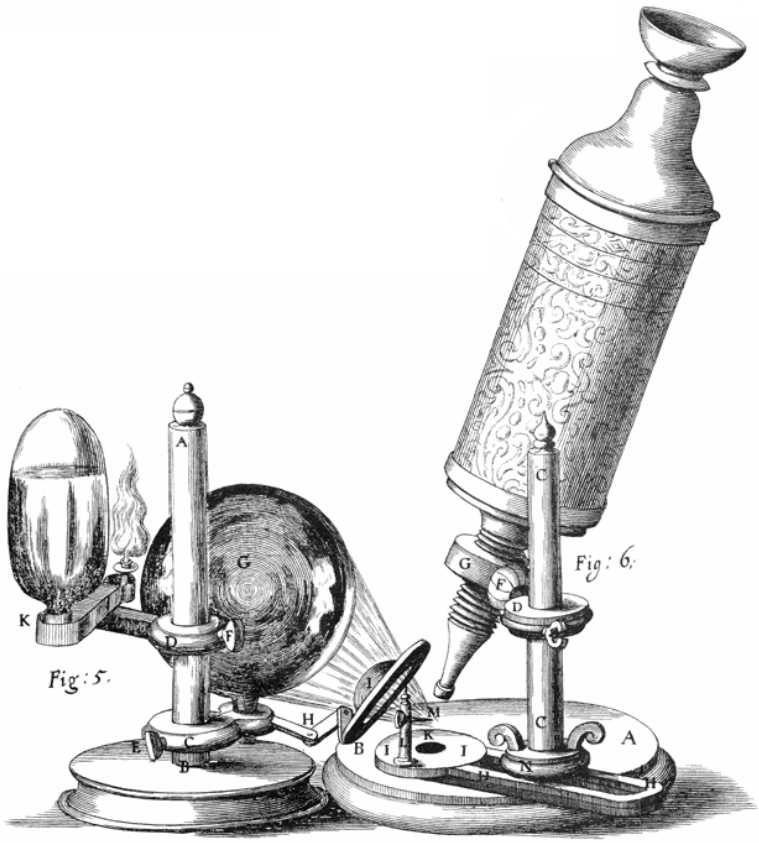

Figure 1.1 – Robert Hooke's microscope as described in '*Micrographia*'.

Ever since the term "cell" was coined in the book '*Micrographia*' by Robert Hooke in 1665 there has been a constant, uninterrupted pursue to develop and continue to refine the technologies that enable us to grasp a better understanding of the inner workings of those remarkably complex while elementary bricks of the living world.

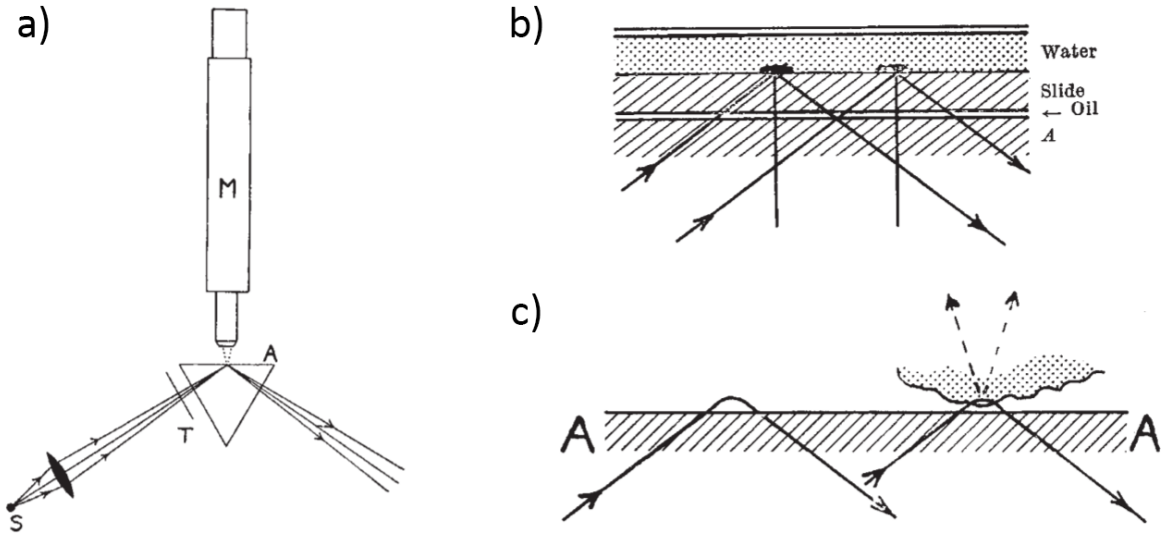

Figure 1.2 – First initial concept for TIRF imaging proposed in 1956, original drawings from [1]. It relied on a mercury arc, a slit and a prism (center of **a**). On top of it and sealed with immersion oil, cells suspended in water in between two glass substrates(**b**) allowed the incident light to strike the interface A at an angle greater than the critical angle(**c**), generating an evanescent field.

Hooke had been assisted by one of the earliest instruments resembling today's notion of an optical microscope, which was based on a recent *at the time* invention by Zacharias Janssen in the early 1600, who had figured out how to utilize more than one convex lens to attain higher magnification and resolution than what was currently possible.

From that point on, the evolution of the microscope has closely accompanied the study of cell biology[1] and albeit the advancements were modest and primitive for the first few centuries, the field has vigorously thrived during the last 70 years[2] to become one of the most powerful tools of contemporary science.

Among the increasingly wider variety of microscope types and microscopy techniques and still motivated by a deeper comprehension of cell's processes, in particular how they interact with their medium, in 1956 it was theorized the idea of using total internal reflection to illuminate fluorescent-marked cells in regions of close contact with a glass substrate[1] (Figure 1.2). This reflection would generate an evanescent electromagnetic field that decays exponentially inside the aqueous specimen medium, exclusively exciting the first $\sim$ 100nm and avoids the emission from the fluorophores bound to the surface from being overwhelmed by the background fluorescence[3]. This work in conjunction with its experimental implementation in 1981[2] gave birth to what today we call Total Internal Reflection Fluorescence (TIRF) Microscopy, a powerful high axial resolution technique to study a broad range of events taking place in cellular surfaces such as cell adhesion[3] and migration[4], protein interactions[5], membrane trafficking[6] among others[7, 8, 9].

[1] Although not called 'Biology' until the late 1700.

[2] Arbitrarily marked by the beginning of confocal optical systems.

[3] The original publication describes it as "*...those portions (of the specimen) which make close contact with the surface of the glass will enter the penetrating beam and will scatter the light, owing to the presence of minute inhomogeneities in their structure*"

1.1.1 TIRF Advantages

The advantageous characteristics that have kept TIRF microscopy relevant even after 60 years of its invention are twofold:

- Very high axial resolution: The intrinsic properties of an evanescent electromagnetic field in the visible range mean that only a very narrow sim100nm plane is excited, leaving the bulk of the specimen in the dark. While this may sound very restrictive, in practice its utility is strongly supported by the large number of cellular events that can be studied on that single plane, and the relative simplicity of the method in comparison with other techniques offering similar resolution.

- Virtually no out-of-focus signal and minimal photo-toxicity: Differently to most other microscopy techniques, that rely on either a selective collection of the fluorescence emission after a larger-than-necessary volume has been excited (e.g. confocal, spinning disk, structured illumination, etc.), depletion of an already excited volume (e.g. STED) or deactivation (e.g. SMLM) of the fluorophores, in TIRF microscopy there is simply no light reaching unwanted sections of the specimen.

1.1.2 Current state

TIRF setups have continuously evolved since its inception using a bulky prism, growing increasingly popular for cellular microscopy as more and easier-to-use solutions became available. A notable milestone took place when the first 'prismless' TIRF setup was introduced to the scientific community in 1989, replacing the original prism by a high-NA objective instead[10], and just a decade later the first TIRF-specific objective based systems started to roll out[11]. Since then, a plethora of variations were tested an implemented, often combining other techniques better suited for lateral resolution with TIRF's axial capabilities, such as TIRF-Structured Illumination Microscopy[12, 13, 14, 15, 16, 17] or TIRF-Single Molecule Localization Microscopy[18, 19, 20].

These hybrid techniques combined with the advent of increasingly higher numerical aperture objectives propelled the development of off-the-shelf objective-based TIRF systems from major microscopy companies (Leica, Nikon, Olympus and Zeiss) as well as third-party suppliers (Imagxcell StarSCAN, BioVision iLas, Mad City Labs MicroMirror, 3i VectorTIRF, Chroma OptoTIRF, ONI Nanoimager). Some notable exceptions to the objective-based systems include the use of waveguides (TIRF-Labs uTIRF[4]), elliptical mirrors[21] and even self-illuminating LED TIRF substrates[22]. While the vast majority of these techniques and systems rely on fluorescent labels to image the sample, some label-free strategies have been developed[23, 24, 25] for those cases where regular dyes are not compatible with the measurements, e.g. long term studies.

While these objective-less modern TIRF techniques exist, they do not represent a significant portion of the TIRF systems in use, that are largely dominated by commercial systems with high-NA objectives. Having this element in common, most of these systems also share some common weaknesses associated to it, most notably the need of direct physical contact with the sample, the small field-of-view (FOV), the evanescent

[4]This system uses either a waveguide, a prism or an objective for the illumination.

field inhomogeneity and the intrinsic cost of the objectives and illuminators[5]. These limitations, that we aim to tackle in this work, rule out or make significantly less convenient use cases such as cryogenic TIRFM (no direct contact possible), large surface studies or biopsies, or the sporadic implementation of TIRFM in environments were a dedicated TIRF system is not justifiable (e.g. small labs, educational, etc.).

1.2 Optical Metasurfaces

1.2.1 Generalities

Despite the myriad of technological advances that have pushed optical microscopy from a simple pair of lenses up to the current state-of-the-art, it is remarkable to realize the extremely close similarities between many, or even most, of the elements that we use to manipulate light today, in relation to those optical elements used centuries ago for similar purposes. When it comes to alter the amplitude, polarization or phase of a beam, e.g. to focus it, conventional optics relying on absorption, refraction and diffraction are still our preferred choice, obtaining the desired effect by a gradual accumulation of one or several properties along the light's propagation through the element's media. While unarguably effective, these 'traditional' approach to optical elements is turning progressively more restrictive as their relative large size and weight is often not suitable for the ongoing high integration and miniaturization of present-day devices.

Metamaterials, named after the Greek words for 'beyond' and 'matter', refers to a wide group of materials engineered to showcase properties that are "beyond" what we see on naturally occurring substances. These artificially created materials, and their two-dimensional counterpart termed Metasurfaces (MS or MSs) derive their unusual properties not from the chemical composition but mainly from the internal micro or nanostructure.

They usually consist of thin and dense arrays of optical nanoscale elements with subwavelength separations acting like 'phase-shifters' to generate the desired high resolution phase profile, by means of varying geometric parameters, ultimately molding an arbitrary wavefront. Contrary to traditional optical components, metasurfaces accomplish this arbitrary wavefront shaping within a distance inferior to the wavelength.

While technically not the first metamaterial ever made, it was only after the early 2000s when researchers started fabricating negative refractive index mediums for the microwave spectrum[26], becoming the first experimental demonstration of theoretical work done 33 years earlier[27], that the field thrived with frequent new demonstrations and applications going well beyond the microwave range. Contrary to three-dimensional metamaterials that generally pose a significant challenge for their fabrication, metasurfaces have largely benefited from existing surface-lithography technologies developed for the semiconductor industry, leading to a higher interest and more research resources poured into it[28], reflected on the 3000% increase on the use of the term 'Metasurface' on scientific publications during the last decade (Figure 1.3).

[5]Dedicated TIRFM optoelectronics to improve the homogeneity of the excitation field or control multiple color lines.

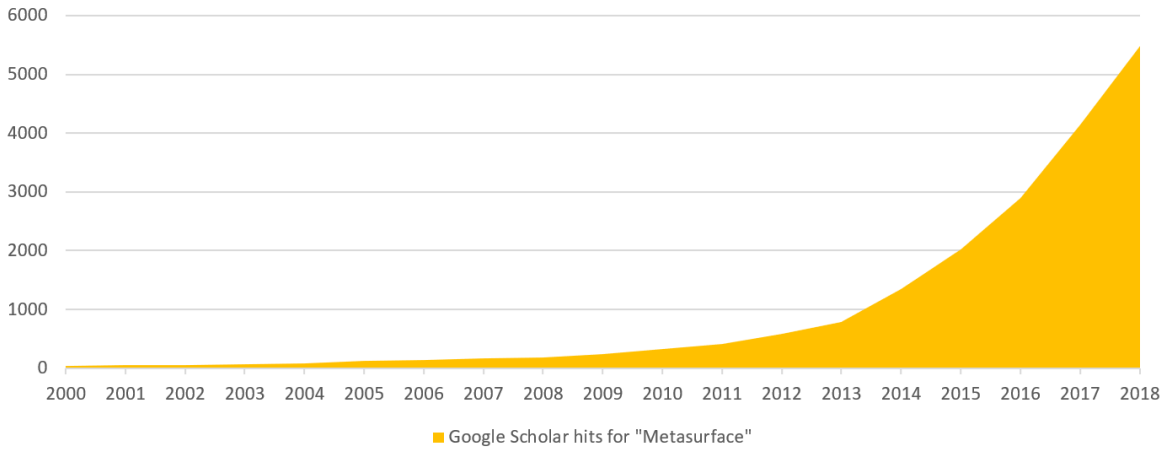

Figure 1.3 – Yearly Google Scholar hits for the term '*Metasurface*' in scientific publications since the year 2000.

In modern metasurfaces the most common underlying physics behind these array elements consist of anisotropic waveguides[29, 30, 31], Mie resonators[32], plasmonic resonators[33] and dielectric transmit arrays[34], all providing different methods to realize the necessary phase manipulation. Applications for these novel devices range from spectroscopy[35] to integrated optics[36], optical filtering[37], sensors[38], holography[39, 40], and microscopy[41] as ultrathin forms of optical couplers, waveplates, lenses[30, 31, 42, 43, 44, 45, 46], focusing mirrors[47, 48], collimators[49], beam deflectors[50, 51, 52], among others[53].

In particular, while not referred to as a metamaterial yet, subwavelength diffractive gratings that generate a quasi-linear phase profile for beam steering in the visible or near-visible have been proposed and fabricated using dielectrics materials (TiO_2) as early as 1998[58, 51] with efficiencies as high as 83% although at very low angles (6.6° in glass, Figure 1.4(a)) largely due to fabrication constraints. Similar phase profiles have also been later achieved using metallic metasurfaces, with arrays of gold plasmonic antennas[55, 59] in the mid and far infrared (Fig. 1.4b). While these structures can successfully achieve a phase coverage of 2π, the strong absorption in the visible range has largely limited its use at shorter wavelengths. For this purpose, dielectric metasurfaces with low absorption at near-infrared frequencies were proposed and demonstrated using silicon nanodisks on glass substrates that offer a diameter-dependent local phase[60], nanoposts of different sizes[52] (efficiencies as high as 77% at 39° and λ=741nm), freeform geometries[57, 56] (86% at 75° and λ=1050nm, Fig. 1.4c-d) and polarization splitting nanobricks at λ=1500nm [61]. Silicon, having a very high refractive index ($\sim$ 3.5) and being transparent at communication frequencies has been the preferred choice for such wavelength range. When moving towards visible light the high intrinsic losses of silicon[30] prevent its use for MS thicknesses above just a few hundred nanometers, under which the absorption can be offset with the high performance achieved by its high refractive index. Examples of this approach are the Si 75nm-thick light deflection MS[50] with a reported 1^{st} transmission diffraction order efficiency of 30% at λ=520 (TM polarized), stating material losses as the limiting factor for higher diffraction efficiencies, and a 250nm-thick silicon on glass NA 0.8 (53° in air) metalens with a measured absolute efficiency of 67%, stating that absorption losses can be

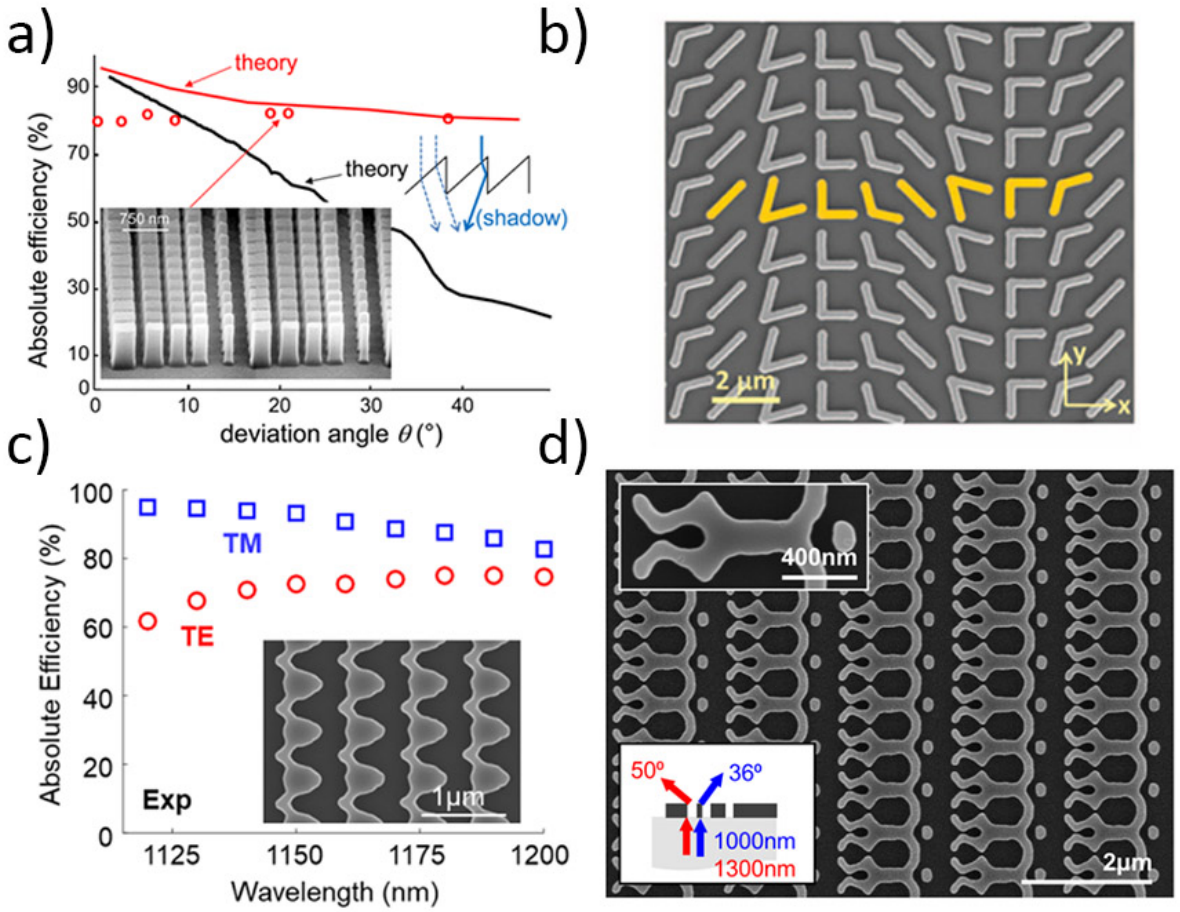

Figure 1.4 – Different techniques to achieve beam steering metasurfaces, using a TiO_2 blazed binary diffractive grating,(a) plasmonic V-shaped gold resonators,(b) and polycrystalline silicon nanoridges and freeform geometries on a SiO_2 substrate (c-d) . Figures adapted from [54, 55, 56, 57] respectively.

minimized using longer wavelengths. To avoid this performance degradation, titanium dioxide has been one of the most common materials found on metasurfaces operating in the visible in recent years, with widespread applications such as holography[62], color printing[53] and more noticeably an extensive variety of metalenses[30, 31, 42, 43, 44, 45, 46]. Titanium dioxide also offers the additional advantage of a superior biocompatibility compared to alternative materials, a highly desirable feature when targeting live cell microscopy as a potential application.

In the context of optical microscopy for biomedical applications, up to this date we have not found ongoing or recent implementations, testing or proofs of concept of any of the aforementioned metasurfaces developments, metalenses included, for biological imaging.

1.3 This thesis

1.3.1 Goal

The main goal of this work consists on achieving TIRF microscopy utilizing a dielectric metasurface as the light coupling element. This goal involved the design of said MS, the development and application of a suitable fabrication process for it, and finally the testing and analysis of its performance as TIRF microscopy device. The motivation behind this goal is to provide TIRF Microscopy capabilities to a wider audience, by making those necessary tools more accessible technically and economically, and to expand the range of suitable applications by improving certain aspects of the current solutions, such as the field of view or field homogeneity. Going well beyond the reach of this project, we can only envision the potential of an inexpensive, replaceable, all-in-one TIRF solution that could be used in any ordinary widefield microscope.

1.3.2 Strategy

Although some key differences could be mentioned between the approach chosen for this work and a generic strategy for product development, we did adopt a simplified version of such strategies which consisted on the following iterative loop:

- Design optimization: Once a starting point was defined based on current literature and in-house knowledge of the materials, processes and fabrication technologies we chose a set of parameters that would define a "base design" and optimized all their values as described in Chapter 2. Depending on the specific purpose of each design, a different figure of merit guided us to the optimal parameters which were later used for the ensuing nanofabrication phase. Any finding resulting from this iterative loop on the following steps is re-incorporated on this phase during the next iteration.

- Nanofabrication: Similarly to the design optimization, the fabrication process for a these kind of patterned nanostructures also involves a large number of parameters that define the behavior of the tools used and in consequence, the characteristics

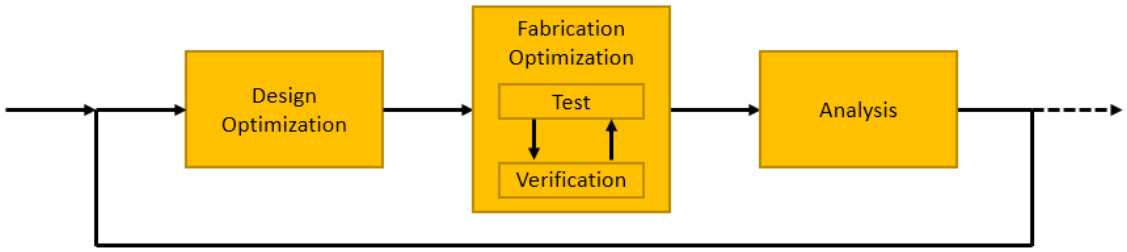

Figure 1.5 – Development strategy of the metasurface-based total internal reflection microscopy device.

of the structures being fabricated. Because of this, and the large variability of results observable with even the slightest alteration of certain fabrication parameters, this phase can and has included secondary iterative loops, that allow us to fine-tune in individual sub-process of the overall nanofabrication process for a given metasurface design. We expected and confirmed that the progress made in this phase on each iteration remains valid within a reasonable range of minor modifications on the design at the beginning of the subsequent iteration, which is a key aspect to be able to converge on a successful prototype.

- Analysis: This phase, which consist on a wide range of studies, is the main source of feedback for the next iterative loop. It allowed us to modify the design to increase its performance as well as to make adjustments exclusively aimed to simplify the fabrication process. When an unavoidable fabrication constraint is found, e.g. the structure's edges are smoothed up, this step also provides the necessary information to include that particular characteristic into the simulations to further improve the accuracy of the model.

Chapter 2

Metasurface design

2.1 Generalities

As described in section 1.2, we introduced the concept of metasurfaces as virtually bidimensional optical elements, whose size in the third dimension is on the order of the wavelength in use and can achieve abrupt changes on the properties of an incoming EM wavefront. In contrast to traditional optical components that rely largely on refraction and long propagation lengths to gradually achieve those changes, the optical behavior of a MS is almost exclusively defined by the design of the structures, sub-wavelength in size, fabricated on the substrate-air interface. By adjusting their size, geometry, orientation or spacing, the intrinsic characteristics of the MS can be adapted to a specific need.

Ever since TIRF microscopy was envisioned more than half a century ago, the different techniques used up to this day differentiate almost exclusively by the way light is coupled into the substrate in contact with the sample. The ease and efficiency of this key element partially dictates the real-world usability and feasibility of the technique as a whole and with that in mind we sought to incorporate metasurfaces as light couplers. Ideally, an optimal MS design will be one that manages to inject the maximum possible fraction of the incident light into the microscopy substrate.

Due to the diffractive characteristics of the metasurface's structure, the most straightforward approach to obtain such desired behavior is to cleverly tune the periodic elements in order to maximize the relative efficiency of one order against the others, while simultaneously adjusting its transmission angle. If this output angle is higher than the total internal reflection angle between two media given by

$$\theta_{TIR} = \arcsin\left(\frac{n_1}{n_2}\right) \tag{2.1}$$

then the diffracted beam will be continuously reflected inside the microscopy substrate acting as a planar multimode waveguide as visualized on Figure 2.1 c). A glass-air interface has a $\theta_{TIR} = 41^\circ$ and this number climbs to $\theta_{TIR} = 61^\circ$ for a glass-water boundary, with slight variations depending on the specific glass type and composition used.

When choosing the material to fabricate the MS, its refractive index will be one of the most important factors and its combination with the different structure's shapes and

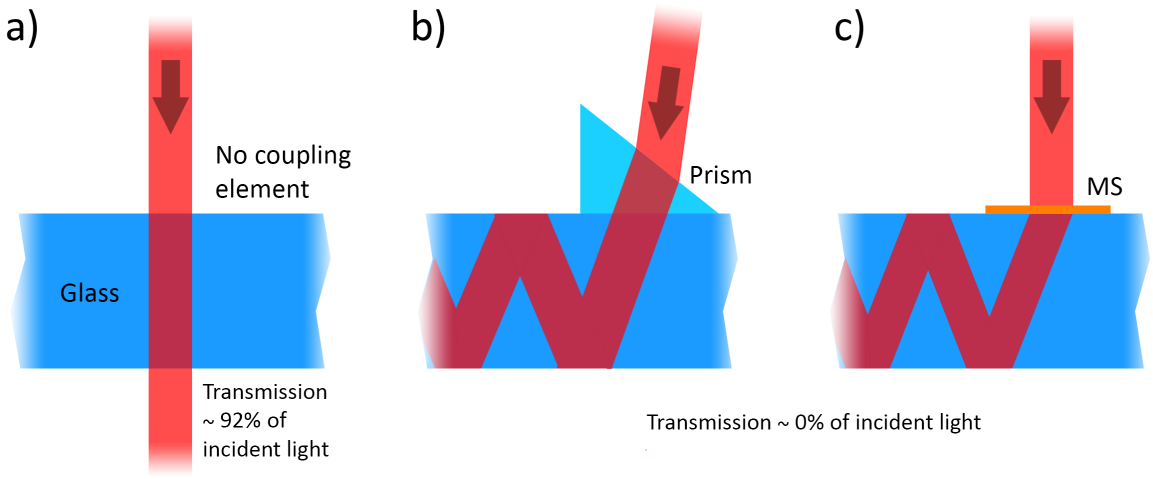

Figure 2.1 – (a)Without a couple the incident light will largely traverse the microscopy substrate and no light will couple into it. (b) Although not the preferred option nowadays, prisms have been used to couple light into the substrate for TIRF microscopy. The usual configuration employed a trapezoidal prism situated on top of the biological sample, different to this conceptual image focused on the substrate coupling mechanism. (c) Proposed concept in which a subwavelength-thin metasurface couples the normally incident light into the substrate.

subwavelength sizes will result in an adjustable effective index that ultimately translates into the desired phase applied on the incoming beam. This 'effective medium' approach and its range of validity has been previously discussed and tested by several authors[63, 64, 58, 51].

The intrinsic asymmetric characteristic that we seek on this metasurface as a coupling device forces us to move away from a regular diffraction grating, not only to maximize the amount of light coupled into the substrate but also to reduce as much as possible the transmitted light that can lead to scattering in close proximity to the fluorescent sample, reducing the overall performance of the device as a TIRF microscopy tool. Figure 2.2 offers a visual example of one of our current metasurface designs and its measured diffraction order efficiencies in comparison to a regular grating of similar characteristics.

2.2 Double groove metasurfaces

In 2014 it was experimentally demonstrated[65] that an asymmetric titanium dioxide double-groove grating (shown in Figure 2.3) had the ability to couple up to 70% of the normal incident TE-polarized light into the 1st order transmission diffraction. This order's output angle was $\alpha_1 = 50°$, higher than $\theta_{TIR} = 41°$ for a air-glass interface and as such, it satisfied total internal reflection for 640nm light.

Although the authors of this work rightfully point out the potential use of these structures as coupling elements for devices such as displays or solar cells, no discussion or analysis was done in the field of optical microscopy, more specifically TIRF microscopy. On the other hand, coming from an optical microscopy perspective, this development could be easily seen like an immediate candidate to be the starting point of a newer

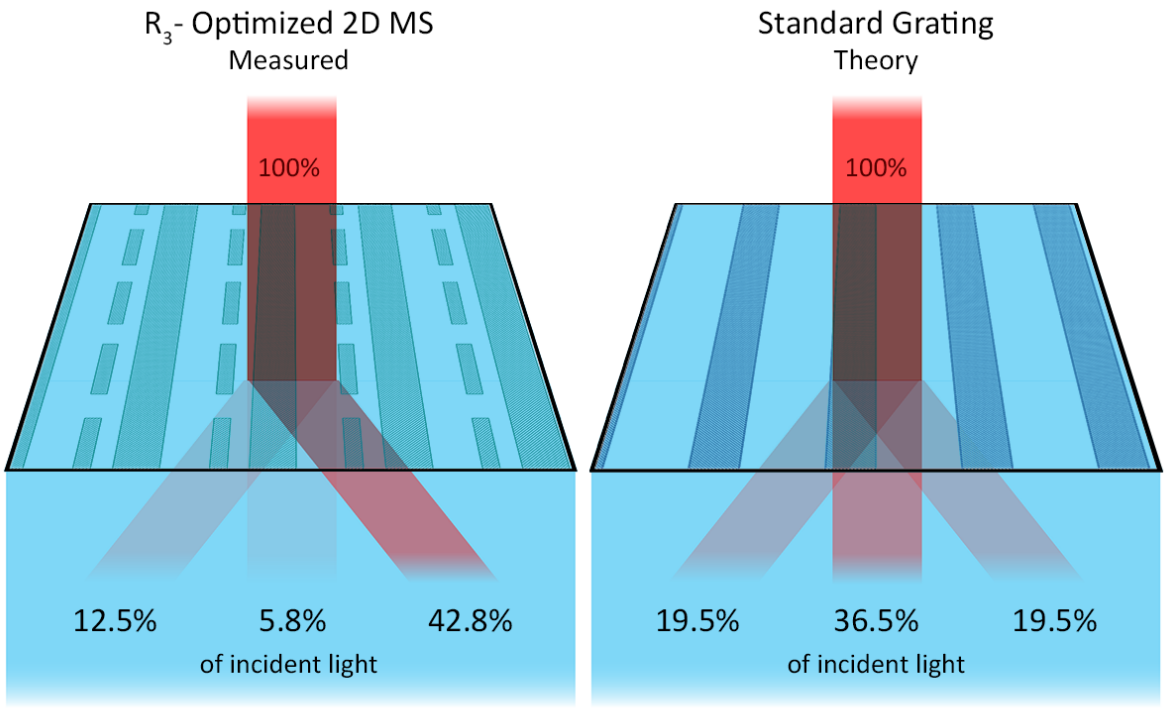

Figure 2.2 – Measured diffraction order efficiencies of one of our fabricated 2D MS samples, which manages to couple more than twice as much light than its standard-grating counterpart (simulated by removing the segmented structures on this 2D MS design), while having a direct transmission 6 times dimmer. The laser beam on this drawing is not to scale.

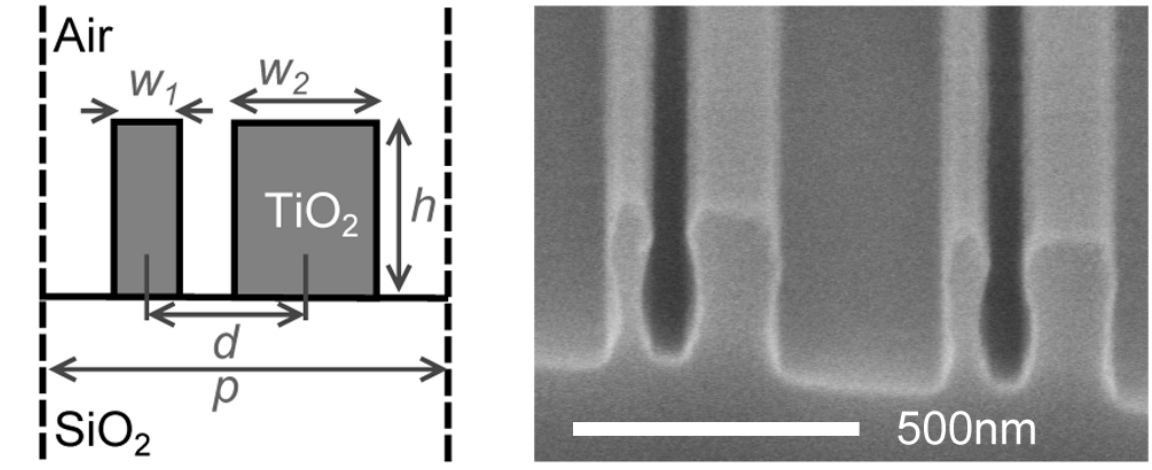

Source: Experimental investigation of double-groove grating satisfying total internal reflection condition. DOI:10.1364/OE.22.025362

Figure 2.3 – Geometry of the double-groove coupler envisioned in 2004 both theoretical (left) and experimental (right). Input and output diffractive channels labeled #1 to #4 respectively. (dimensions; $W_2 = 140$ nm, $W_1 = 60$ nm, $d = 180$ nm, $h = 230$ nm, $p = 580$ nm, refractive indices; $n_{TiO2} = 2.435$, $n_{SiO2} = 1.457$)

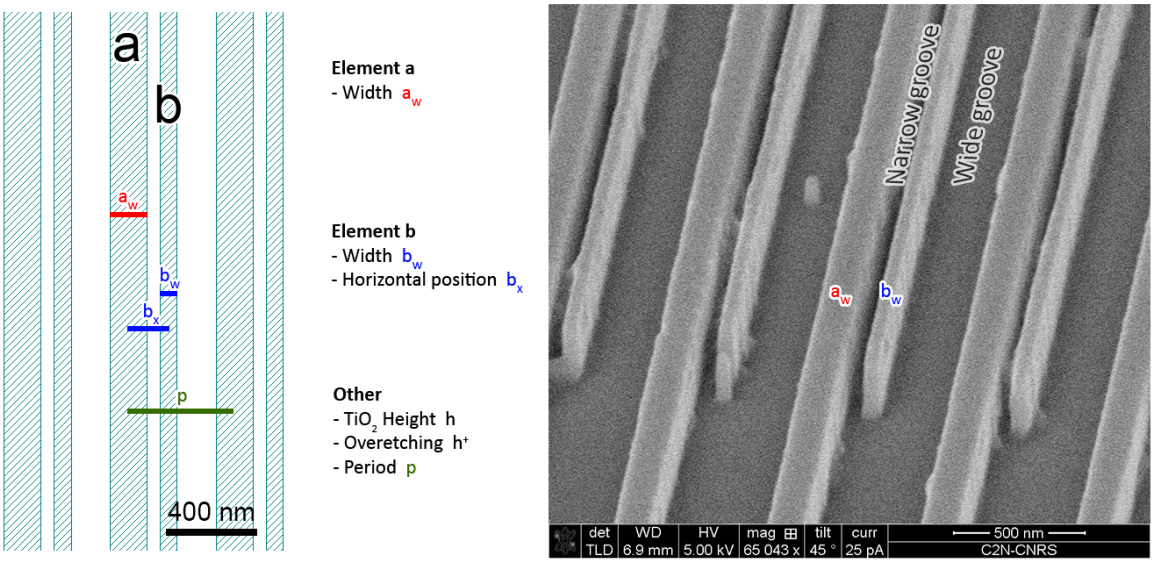

Figure 2.4 – Design-defining set of parameters for one generic metasurface used to optimize its performance as a light coupler device. The wider line, labelled 'Element a' is only defined by its width a_W, while the thinnest line, 'Element b' has a width b_W and a relative position b_X

generation of TIRFM tools. Unfortunately, this does not mean that a straightforward implementation is possible since a few key points should be addressed and one above all: in the ample majority of cases, a biological sample being observed is embedded in an aqueous medium with a refractive index typically close to that of water. In turn, a water-SiO_2 interface will have a much higher total internal reflection angle $\theta_{TIR} = 61°$ requirement and as detailed on the following sections (2.4 and 2.5) this will introduce some major fabrication challenges.

Figure 2.4 shows a basic scheme of the design and the appearance (SEM image) of the first metasurfaces we fabricated. Before submerging into the numerical simulations and optimization of the MS, some general geometric characteristics can be described:

- Period **p**: Our metasurfaces are periodic structures and as such, one could consider the period as the single most important parameter. We can calculate their first diffraction order's angle α_1 given by:

$$\alpha_m = \arcsin\left(\frac{m\lambda}{np}\right) \tag{2.2}$$

  With m corresponding to the diffraction order number, λ the wavelength of illumination used, n the refractive index of the substrate and p the period of the MS. Normal incidence is assumed. It is important to stress the independence of this angle from all others design parameters, which will in turn affect the diffraction efficiencies.

- The width of each line and its separation, labelled a_W, b_W and b_x in Figure 2.4 are the parameters best suited to work with in order to tailor the efficiency of the different orders. This is partly due to the fact that although other parameters also

affect these efficiencies, they are significantly more sensitive to minor environmental variations during the fabrication process. The asymmetric characteristic (i.e. blazed grating behaviour) of the metasurface depends on the ratio between the different widths as they define an effective index profile.

- Thickness **h**: The thickness of the deposited thin layer of TiO_2 will turn into the parameter 'height' or h once the TiO_2 is fully etched. This structure height determines the maximum phase jump that an incoming wavefront may acquire when traversing the MS, and as we can see in the upcoming sections it greatly affects the maximum ratio attainable between the efficiency of the positive and negative first order. Up to a certain point its beneficial to increase this value as much as the fabrication process allows, considering the aspect-ratio of the structures also scale up with it. Contrary to other parameters that could be changed on a sample-to-sample basis, the TiO_2 thickness had to remain constant for all the samples that came from the same deposition batch.

- Overetching $\mathbf{h^+}$: Finally, we quickly realized the important role taken by the sometimes-unavoidable overetching h^+ due to the Aspect Ratio Dependent Etching (ARDE) effect. Unlike all the previous parameters, its value is not under our control in a direct way, but only through our choice of a mask type and etching process. The inclusion of this parameter seeks to improve the accuracy of the simulations of MS designs with very different aspect ratios on their unit cell (within this project, almost exclusively 1D MS designs). This effect is further detailed in subsection 2.4.2.

Once all the parameters have been chosen, a GDS (Graphic Database System) layout file will be generated using a custom Python script built on the IPKISS parametric design framework. This code will also include an automatic labeling for an easier identification of the different samples.

2.2.1 Metasurface size and substrate arrangement

As can be observed in Figure 2.5 there is a maximum size D_{Max} that the metasurface can take before it overlaps with the point where the coupled beam has its second internal reflection. If this happened part of the beam would be decoupled out of the substrate through same metasurface it was coupled in before, reducing the performance of the device. Assuming the excitation beam has the width of metasurface, which is expected by design, the size D_{Max} is given by the first order's angle and the substrate thickness, following the equation in Figure 2.5. It is worth noting that this limitation is only valid on the plane defined by the 3 diffracted beams, and the MS can be arbitrarily large on its other direction (perpendicular to this page).

With D_{Max} being the maximum suitable metasurface width, h_s the thickness of the glass substrate and α_1 the first order diffraction angle given by Equation 2.2. In our case this meant each MS had to be smaller than 660µm for the typical 170µm-thick coverslip (λ =640nm) and in turn, between 10 and 40 individual metasurfaces could easily be arranged on a single 25x50mm coverslip substrate. Figure 2.6 shows one of such MS sample layouts and its corresponding finalized fabrication.

$$D_{Max} = 2h_s \tan \alpha_1$$

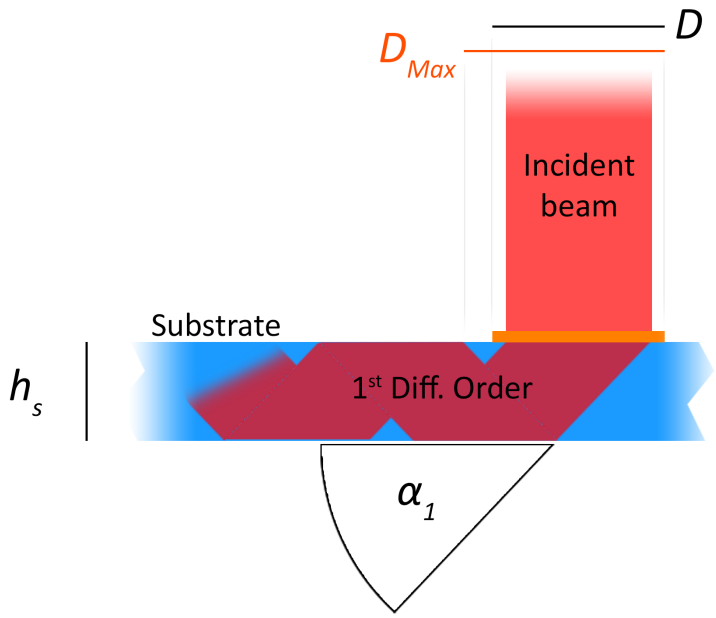

Figure 2.5 – The metasurface size D cannot exceed a maximum value D_{Max} along the direction of the diffraction orders is limited by the position of the second internal reflection of the coupled beam, affected by both the first diffraction order angle α_1 and the substrate thickness h_s. If this condition was not met, part of the beam would diffract out of the substrate, decreasing the performance of the device.

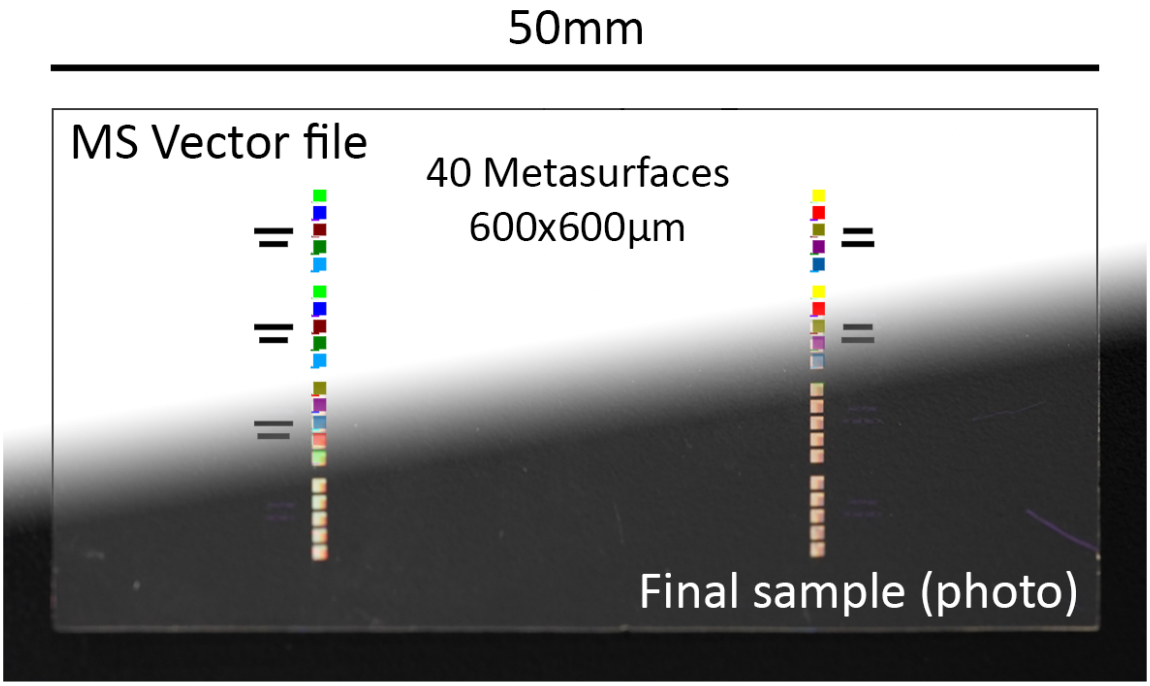

Figure 2.6 – Physical arrangement of 40 individual square 660µm wide metasurfaces in a single 25x50mm coverslip substrate, covering 2 different e-beam exposures, both . All the MS are oriented in such way that the maximized first diffraction order is coupled towards the center of the substrate, where the biological sample is expected to be placed.

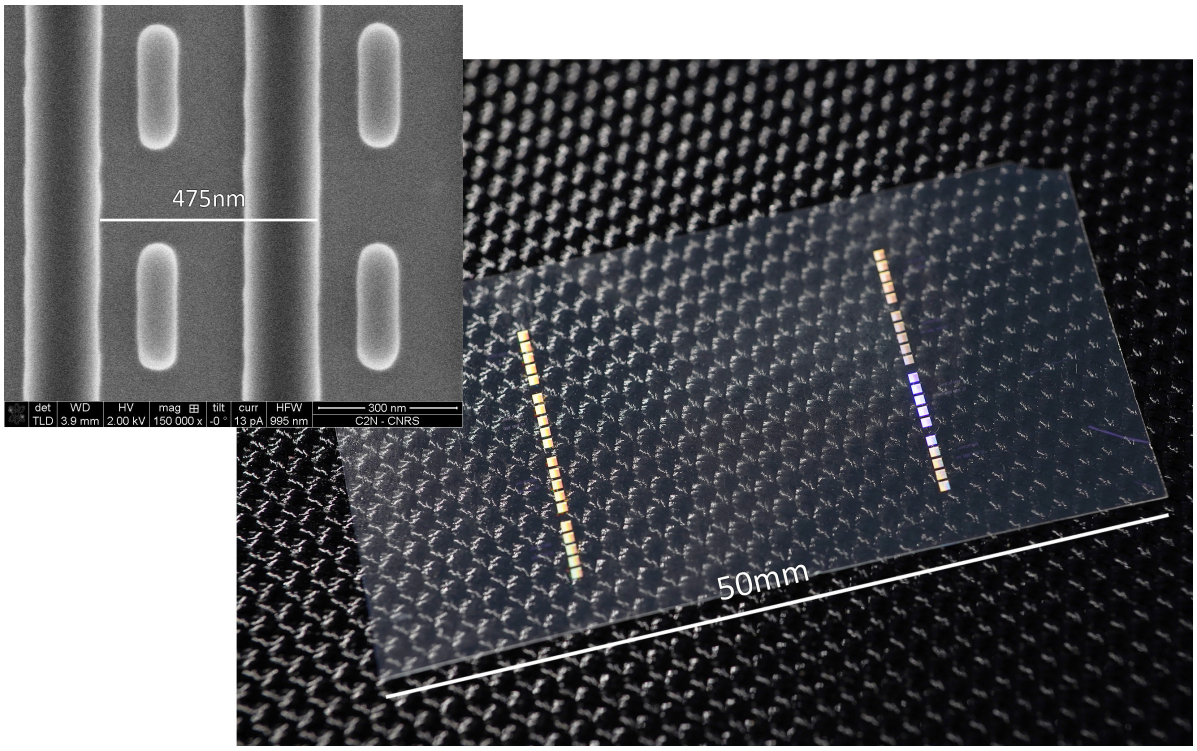

Figure 2.7 – Left: SEM Image of the smallest features (b_W=80nm, p=475nm) that need to be patterned into the MS material. Right: Sample closeup with 40 individual 0.6mm squared metasurfaces as seen with the naked eye.

2.3 Nanofabrication compatibility

There are several aspects of importance that have to be taken into account to design the metasurface pattern, which are mostly related with the ensuing nanofabrication phase. In order to favor a successful and timely fabrication, it is absolutely necessary to consider:

- **Metasurface patterning time**: When using nanofabrication processes based on electron beam lithography, similarly to other scanning derived techniques, we find a strong correlation between the resolution chosen (i.e. the size of the electron beam waist) and the time employed for a given writing area. When it comes to metasurfaces which are usually manufactured in sizes ranging from tens of microns to rarely a few millimeters[31, 42, 30, 51, 58, 66], we are forced to constantly consider the ratio between the resolution needed to 'draw' the smallest features of the design, and the overall area of the completed metasurface. In reality, these two parameters are also linked and constrained by other aspects of the design such as the size of the beam that will be hitting the MS or the TIR angle needed for a given substrate material, so an inevitable trade-off is found. In this project we chose to work with borosilicate glass as the substrate, the most commonly available material for microscopy slides and coverslips, and we designed the metasurfaces to be used with an incident laser beam waist size of 250-300µm, roughly half the size of each 600µm MS visible on Figure 2.7.

  Lastly, there is also a relationship between the maximum MS size and the substrate thickness, as it is important that the reflected beam does not hit the metasurface's

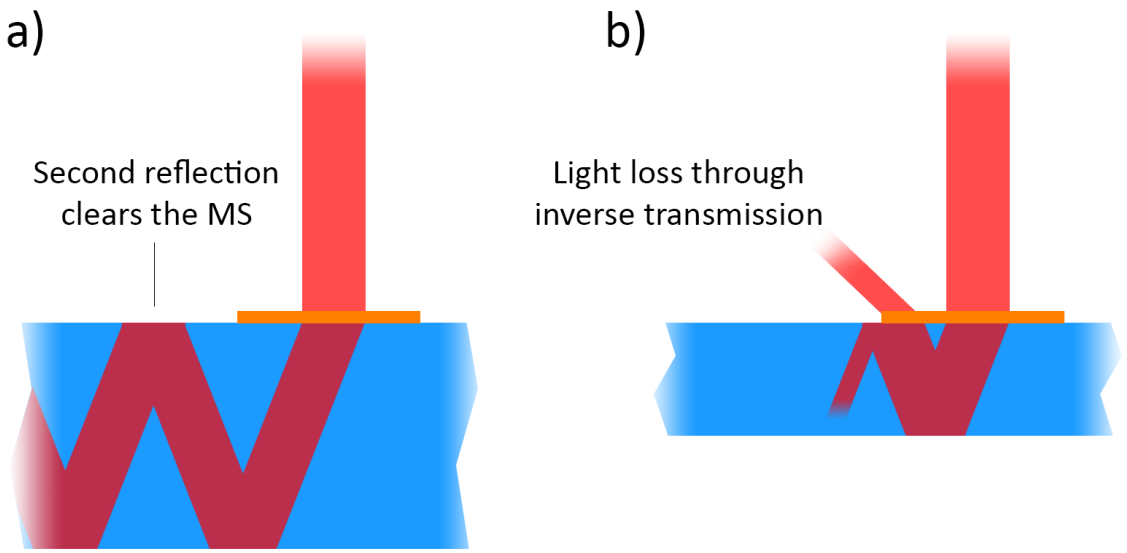

Figure 2.8 – Left: The beam's second reflection takes place on a substrate-medium interface. Right: If the substrate is too thin or the MS too large, the beam's second reflection will hit the MS a second time and the beam will be coupled out of the substrate.

bottom side. Figure 2.8 shows how the same MS size can result in less coupled light if the glass substrate is too thin in relation with that size.

- **Structure aspect ratio**: Assuming the heights of the structures composing the metasurface remain constant, as is usually the case, the aspect ratio will only change with the horizontal size of the pattern. Regardless if these structures are fabricated by depositing or removing material, narrower and taller features will necessarily turn the process increasingly complex and challenging. The tallest a feature in the pattern becomes, the thicker the mask used to transfer its shape to the sample, which in turn directly affects the resolution achievable and thus the smallest horizontal size. On the other hand, there are performance benefits of a higher aspect ratio (further detailed in chapter 2.3) and similarly to what was discussed for Patterning time, this leads to another design trade-off.

- **Uniformity of openings**: All along this project we used several different dry etching techniques and recipes, and depending on the particularities of each one of these processes we could perform a highly "chemical" isotropic etching (through chemical reactions between the gases in the plasma and the etched material), a mostly "physical" unidirectional etching (by high-energy collisions that break the etched material apart) or a mixture of both. Although one could be lead to believe that a perfectly physical and unidirectional etching would have a rate independent of the dimensions of the section being etched, in reality that is never the case, and a wider, larger area will always be etched faster than a thin or small section, specially if there is also some chemical etching involved. As a direct consequence of this asymmetry, it is extremely challenging to have equal etching depths on sections of significantly different sizes. Figure 2.9 shows one example of this effect, clearly visible on a profile SEM image of one of our 2D metasurfaces . In turn, this allows for two possible alternatives: either to embrace and incorporate this

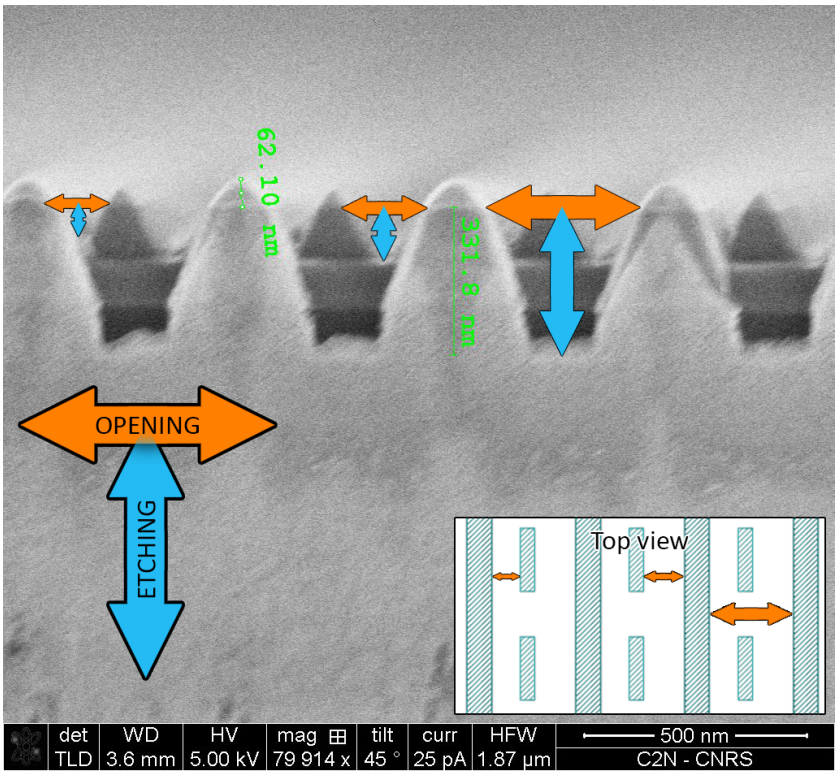

Figure 2.9 – Profile view of a 230nm-thick layer of TiO_2 with a 20nm nickel mask etched on an CCP RIE plasma. Although one would desire the entire surface to be etch to an equal depth, the 130nm-wide orange opening on the left was etched to a depth of 65nm, while the 170nm-wide opening shown in the center in orange was etched 110nm and the even larger 330nm section in the right was etched 332nm, all through the TiO_2 and deep into the glass substrate as well. The entirety of this surface was exposed to the same plasma in the reactor.

uneven etching into the design and simulations, knowing in advance that it is an inevitable characteristic of dry etching processes, or to design a pattern in which all the surfaces to be etched have roughly the same dimensions.

Although it could be conceivable other alternatives to partially mitigate this issue, such as the addition of a 'stop-layer', this would only be a partial solution and one that would carry other secondary undesired effects and as such, it won't be developed in this project.

- **Structure shapes**: The electron beam (e-beam) lithography system used for all the nanofabrication on the scope of this project was a EBPG-5000 manufactured by Raith. This particular model and its operating software utilizes a family of writing strategies seemingly optimized to write (or 'scan') rectilinear shapes and thus more complex shapes like circles or ellipses (Figure 2.10) will take notably longer times to be written. Additionally, the design-file processing time required in advance, which includes calculations like proximity correction factors, are also affected by the complexity of the structure's shape, with file sizes quickly becoming a limiting factor for centimeter-large structures[67].

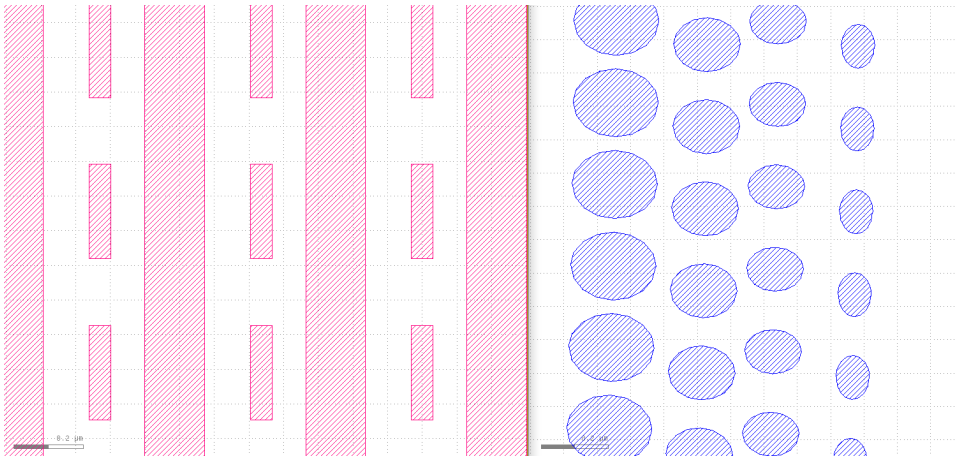

Figure 2.10 – On red and blue two different patterns fabricated with our e-beam system, consisting on similarly sized elements but with the rectangles in red taking just a fraction of the time required to write the ellipses in blue even though their total exposed surface and dose was comparable.

2.4 1D Asymmetric double-groove metasurface

2.4.1 Structure and Numerical simulations

We utilized J.P. Hugonin and P. Lalanne's RETICOLO software for grating analysis, a package of MATLAB routines capable of calculate the diffraction efficiencies and amplitudes of 2D stacked gratings as well as calculate and visualize the electromagnetic fields on them, using a frequency-domain modal method known as Rigorous Coupled wave Analysis (RCWA) [68, 69, 70, 71, 72, 73, 74]. RCWA is a relatively straightforward technique to obtain the exact solution of Maxwell's equations for electromagnetic diffraction in grating structures. It consists on dividing the grating structure in uniform vertical sections or 'layers', which allows for a separate exact calculation of the electromagnetic Bloch modes in each one of them, and to finally merge all those solutions using the boundary conditions between the layers. The accuracy of the method will depend on the number of Bloch modes considered for the expansion, with a more accurate calculation demanding more computing resources. While fabricated metasurfaces are of course finite in all dimensions, this type of calculations are done assuming infinity in both the in-plane dimensions.

Using this software as a platform for a series of custom scripts better adapted for the type of analysis we performed allowed us to better understand the type of optical behavior that we could obtain with each of the degrees of freedom that we had available, i.e. each of the design's parameters. Our simulations use a TE-polarized normal incident beam and the efficiency of the order m is defined as $\eta_m = |E|^2$ of the diffracted transmitted wave. It is important to note that for the wavelength and periods used along this project, and normal incident light, only 3 diffraction orders are transmitted. The general appearance and parameters used for the 1D metasurfaces discussed in this section are visible in Figure 2.4.

2.4.2 1D Optimization methodology

The optimization process can be split and tackled in 3 main parts:

- **Defining the target MS behaviour**, in this case the output angle requirements for a metasurface-based TIRF substrate to be functional. Considering a typical microscopy coverslip (borosilicate glass) and water as the two materials at the interface, with refractive index of 1.52 and 1,33 respectively, we need a beam's angle of at least 62 degrees (Equation 2.2). Lower than that means that the beam will not be coupled into the substrate, and higher will only translate into a thinner evanescent field outside the substrate. Ideally we want to stay slightly above this value. To generate such beam, we chose a metasurface design based on an asymmetrical grating pattern engineered in such a way that one of its first diffraction orders channels most of the incoming light, while having an output angle α_1 satisfying TIR. As with a regular grating, the required α_1 angle is fixed with the metasurface's period.

- **Choosing a figure of merit**, that acts as a direct mean of performance comparison between multiple designs. It has to be easy and fast to calculate for each set of parameters that unequivocally define a metasurface design. With it, an algorithm can navigate the multidimensional space of parameters and find the best performer design by maximizing such figure of merit. Taking into consideration the different positions the metasurfaces could take on the substrate, closer or further away from the observed biological sample, led to the selection of two different figures of merit:

  - Our first and most and most evident choice is a direct ratio between the efficiencies of the desired order (1st negative) and the sum of the other two (1^{st} positive and 0^{th}). Picking the negative first order against its positive counterpart is completely arbitrary as they both are diffracted with the same angle.

    $$R_3 = \frac{\eta_{-1}}{\eta_0 + \eta_1}$$

    With η_m being the transmission efficiency of the order m. Notably, when the first orders have an angle superior to 30 deg, the second diffraction orders become evanescent, as their angle would be over 90 deg.

  - Due to the specific purpose of out metasurfaces, and depending on the final device configuration, it could be the case that further increasing the efficiency of the order of interest (1^{st} negative) is advantageous even if that also increases the opposite order (1^{st} positive) as long as the transmission (0^{th}) remains minimal. This is attributable to the fact that on our MS-TIRF setup, the unused order being diffracted in the opposite direction to where the biological sample is situated, remains also coupled to the substrate and as such cannot reach the volume of the observed sample. Any possible scattering on the edge of the substrate is sufficiently far to have no visible negative effect and any light being reflected on the edge will effectively increase the evanescent field intensity, although arguably a negligibly amount. With that

in mind, we also used is a figure of merit to maximize that ratio regardless of the 1st positive order.

$$R_2 = \frac{\eta_{-1}}{\eta_0}$$

- **Establishing a search algorithm**, that allow us to rapidly find the best parameters possibles. In our case, the calculations needed for each unique set of parameters required about 150 milliseconds of computing time, which means that although a "check all combinations" approach is doable for 2 or 3 different parameters and a small number of points, it is not feasible for a wider and more refined search (see section 2.5).

After using the results described in section 2.2 to cross-check our RCWA simulations, we redefined an equivalent free-sized structure with only 2 fixed parameters: The metasurface's period p was selected to be one such that the transmission angle was above 61 degrees, corresponding to the total internal reflection angle θ_{TIR} for a borosilicate glass to water interface. Using the equation 2.2 and 2.1 for $\alpha_1 = \theta_{TIR}$ and $n = n_2$ this results in:

$$p_{TIR} = \frac{m\lambda}{n\sin(\alpha_m)} = \frac{\lambda}{n\sin(\arcsin\frac{n_1}{n_2})} = \frac{\lambda}{n_1} = \frac{640nm}{1.33} = 481nm \tag{2.3}$$

and thus the first period p fabricated was chosen to be 450nm in order to stay comfortably above 61 degrees for both 640nm ($\alpha_1 = 69deg$) and 675nm ($\alpha_1 = 81deg$) red lasers, the illumination wavelengths available in our experimental setup. The second fixed parameter was the metasurface's thickness h, which can also be seen as the structure's height and was chosen to be 230nm, in order to match those samples fabricated on our reference work (2.2). This number also comes from the typical structure sizes on the design and their resulting aspect ratio. The approach followed was to choose a design that we could probably fabricate before trying more challenging structures that take more effort and time to produce. From a microscopy perspective, there is little use for a design that we cannot fabricate.

The rest of the parameters, i.e. the width a_W and b_W of each line shown in Figure 2.4, and the distance between their center position b_X, were free to take any integer value, as long they were not overlapping, since this would turn them into a single line and thus the design would become a regular diffraction grating. We also considered the minimum size step variation to be around the resolution of the nanofabrication technology in use (electron beam lithography, see Chapter 3) which is on the 1-2 nm range.

With all these conditions the number of possible 1D metasurface designs is relatively small, and it is entirely possible to obtain the diffraction order efficiencies for all the cases and simply select the design that better fits our requirements, which in our case corresponded to $a_W = 158nm$, $b_W = 72nm$ and $b_X = 170nm$ (Using R_3 as figure of merit).

Overetching on the design

Given that all our nanofabrication efforts were going to be put into a handful of different designs, it was of great importance to simulate the structures as realistically as possible

and one aspect that we were aware we would find a discrepancy was on the depth of the grooves. It is relatively hard to etch narrow grooves of different widths to an identical depth. The technical reasons behind this are further detailed on chapter 3 but it become evident that incorporating an asymmetric depth on the design's grooves would improve the accuracy.

Figure 2.11 shows how the simulated diffraction order efficiencies are affected by the overetching of the glass substrate on the wide groove, as well as the resulting ratio R_3. Although it could give the impression that the difference is minor, it just takes a small deviation from normal incidence (5 degrees) for the overetching value to increase or reduce the figure of merit R_3 by a factor of 4.

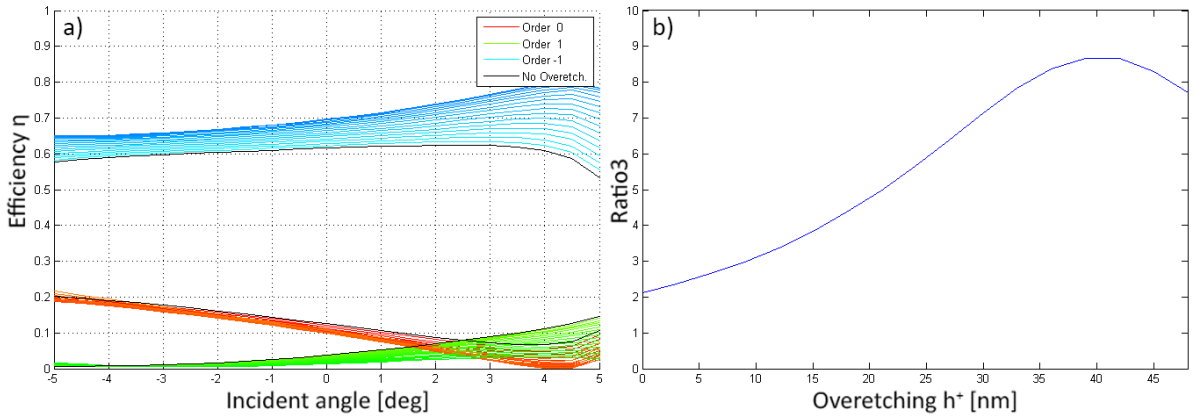

Figure 2.11 – Left: Simulated efficiencies of the orders for a test sample for different overetching values on the wider groove, from no overetching to 50 nm deeper than the narrower groove. Right:Figure of merit Ratio3 for a slightly angled incidence (5deg) and different simulated overetching values.

2.4.3 Selected 1D Metasurfaces

Starting from the 1D asymmetric grating design, our RCWA simulations allowed us to better understand and gain some predictability power in order to better focus on certain aspects of the design. For the first design we took into consideration the range of commercially available fluorophores, that cover the entire visible range but with more variety in the 480-580nm range and the tight relationship between the excitation wavelength used, the metasurface period and the size of its structures. Figure 2.12 shows a series of individual optimizations for each wavelength λ in the 450-700nm range, starting each optimization on the best parameters found on the previous λ. For the intended use of the MS, we need to maintain the α_1 order angle constant. This requirement along with Equation 2.3 tell us that the period p will scale linearly with the wavelength λ, generally forcing those structures fitting within a single period to shrink as well, becoming increasingly harder to fabricate as we see on 2.12(a). In this optimization series the height of the TiO_2 layer h is kept constant, and all other variables were free to take any value regardless if we could fabricate it or not. We observe a high $R_3 = 12.9$ for $\lambda = 566nm$, although not without a challenging 50nm gap in between the **a** and **b** lines (see Fig. 2.4) and a thin $b_W = 46nm$ **b** line. The maximum on both ratios seen around λ=566nm is correlated with the TiO_2 thickness h=230 in relationship to the wavelength,

and these curves shown in (a) can be interpreted as the same as those in Figure 2.17 that were simulated for a fixed λ but a variable h.

Similar reasons apply to the height h of the structures and all this led us to focus on only 3 parameters: The width of both lines a_W and b_W and the relative position b_W. On the other hand, discretizing these magnitudes beyond the nanometer resolution of the electron beam lithography would not provide any real advantage, which means that this 1D metasurface optimization consisted on finding the best performer design out of a pool mathematically defined by:

1. A fixed period $p = 450nm$ to satisfy Equation 2.3 at λ = 640nm, with a 8 degree margin over TIR angle.
2. A fixed height $h = 230nm$ defined as a good compromise between metasurface performance and our current nanofabrication capability.
3. A three-dimensional matrix with all the possible values for the parameters a_W, b_W and b_X. Their extreme values are 0 and p, although in practice we do not need to calculate those designs deemed invalid because they are symmetric or they are beyond our fabrication capability. We can also skip those designs that are a mirrored copy of a previously calculated design. Figure 2.13 shows some possible random designs, including some of those invalid cases.

With these conditions we chose the design with the highest ratio R_3 at λ=640nm shown in Figure 2.14. It is defined by h=230nm, p=450nm, a_W=158nm, b_W=72nm and b_X=170nm.

2.4.4 Characteristics of the selected 1D MS design

Figures 2.15 and 2.16 contain the calculated efficiencies for the main three diffraction orders and their response to these variations, which generally tend to reduce the optimized ratio by reducing the desired η_{-1} efficiency while increasing the other 2 transmitted efficiencies. Despite the fact this is to be expected considering how the parameters were optimized, it was important to also observe a smooth dependence of the calculated efficiencies on the structure's dimensions, to assure some level of robustness against manufacturing imperfections. This particular 1D metasurface, designed to have its first diffraction orders transmitted at 69°, has a relatively high ratio $R_3 = 3.7$. This particular metric chosen to evaluate the MS performance by definition treats equally the efficiencies η_0 and η_1 but in following samples we prioritized reducing the intensity of the order 0, even if that meant slightly reducing the overall R_3. This is due to the fact the direct transmission (0^{th} order) could potentially be more detrimental to the imaging process than the light being coupled into the substrate in the opposite direction (1^{st} order), that will not be able to ever reach the observed biological sample placed on top of the substrate. Figure 2.15 also let us clearly see the maximum wavelength (684nm for this sample) that still produces a pair of transmitted first orders, with only direct transmission being visible for longer wavelengths.

On Figure 2.16 and Figure 2.17 we can also see a behavior we observed all across our simulations, slightly taller structures (h ∼13% taller) would theoretically lead to even

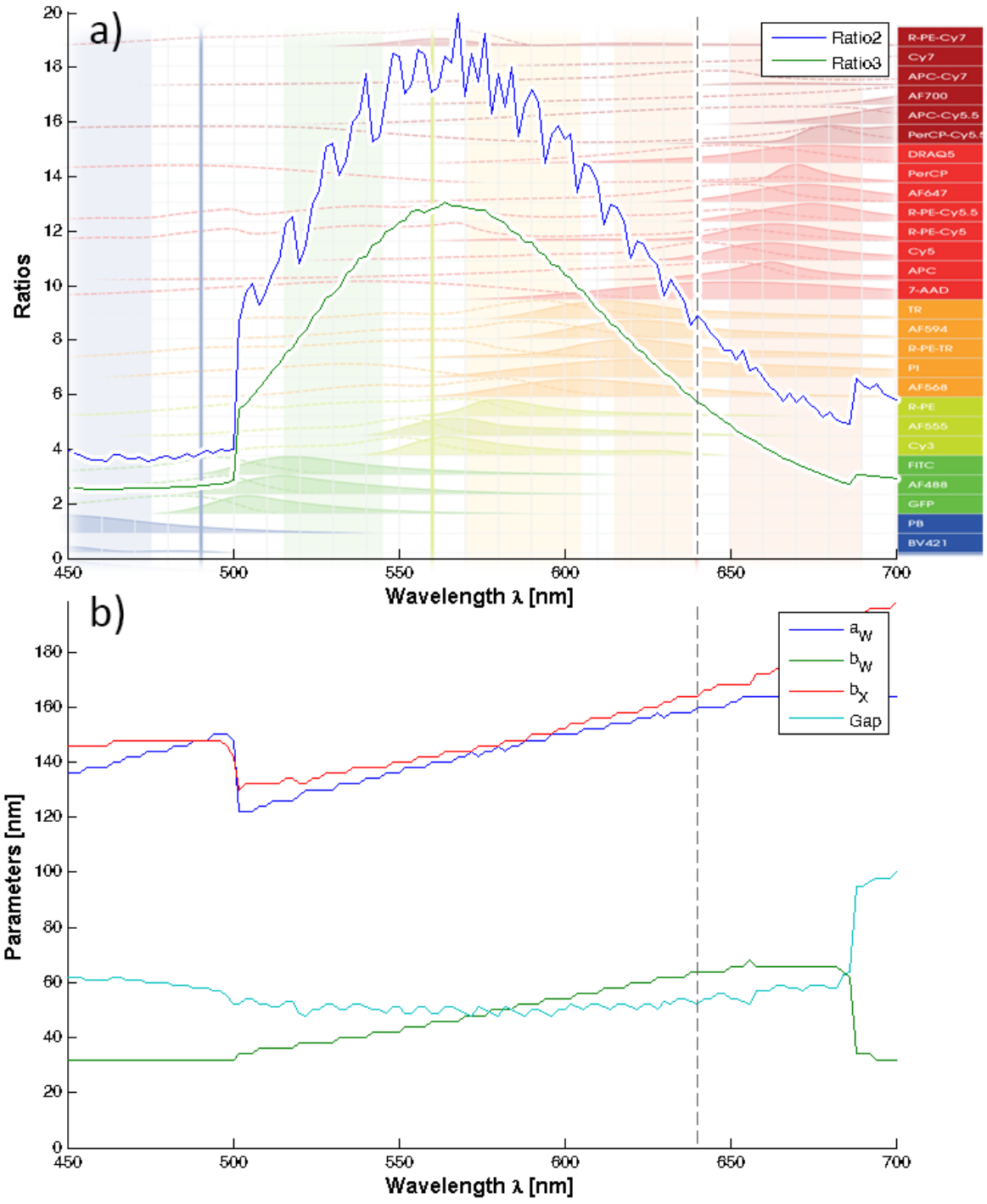

Figure 2.12 – (a) A single optimization series starting with a random set of variables at λ=450nm and re-optimized in 2nm steps until the excitation wavelength is 700nm, with the available fluorophores in the background. Moving from our chosen λ=640nm marked in a dotted gray line, the ratios R_2 and R_3 increase towards λ=566nm (at this fixed layer thickness h=230nm), but simultaneously the dimensions of the MS elements and the distances between them tend to shrink(b), making the fabrication more challenging. With this in mind we saw λ=640nm as good compromise between compatibility with a wide range of dyes, and a more accessible TiO_2 patterning process. This also stress the importance of keep refining the TiO_2 fabrication process to reach increasingly higher aspect ratios. Background on (a): go.myabcam.com/fluorochrome-chart

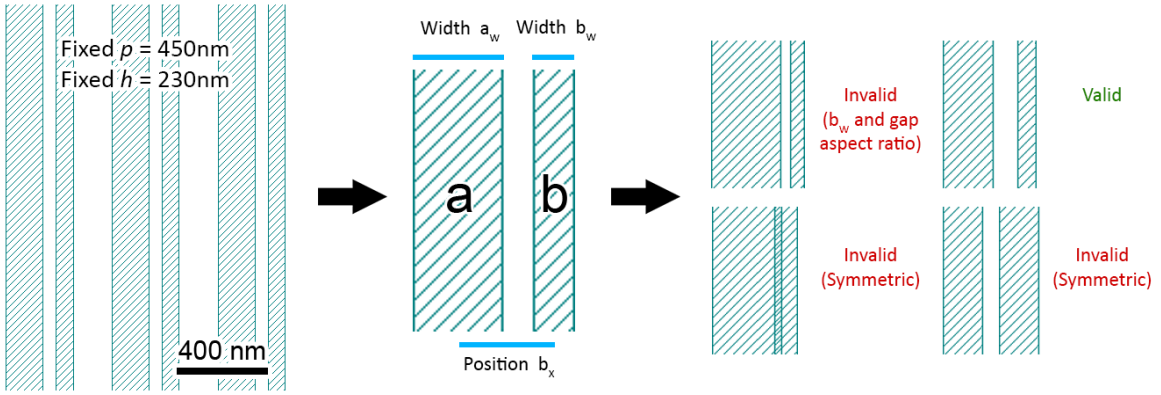

Figure 2.13 – Although the variables a_W, b_W and b_X defining the 1D MS design can theoretically take any value between zero and one period p, in practice the majority of the resulting designs are excluded because either they are not asymmetric or the resulting aspect ratios are too high for our current technology.

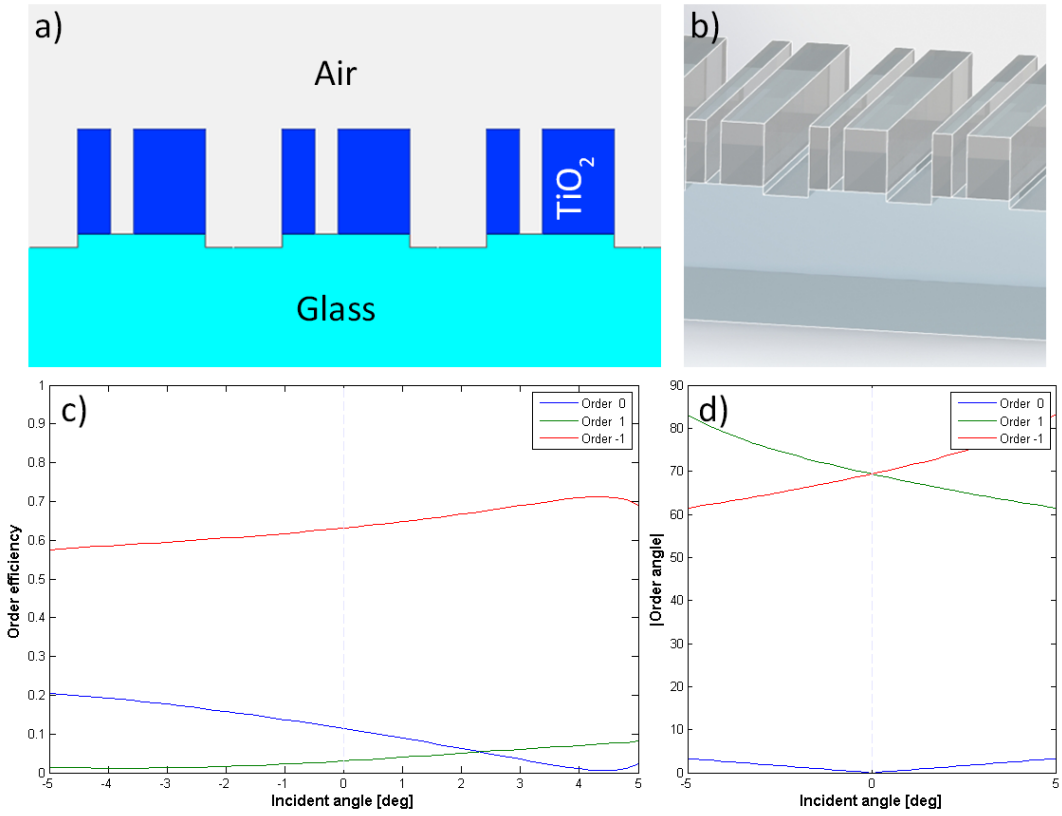

Figure 2.14 – Profile (**a**) and 3D render (**b**) of the chosen 1D metasurface structure optimized for λ=640nm, with a theoretical ratio R_3 of 3.8 at an angle of 69 degrees. Bottom: Efficiencies for normal incidence are 0.62, 0.13 and 0.04 for the orders -1, 0 and 1 respectively. This MS is defined by the parameters h=230nm, p=450nm, a_W=158nm, b_W=72nm and b_X=170nm.A h^+=30nm overetching is considered in the simulations, based on our first measurements using the first fabrication process (Section 3.2).

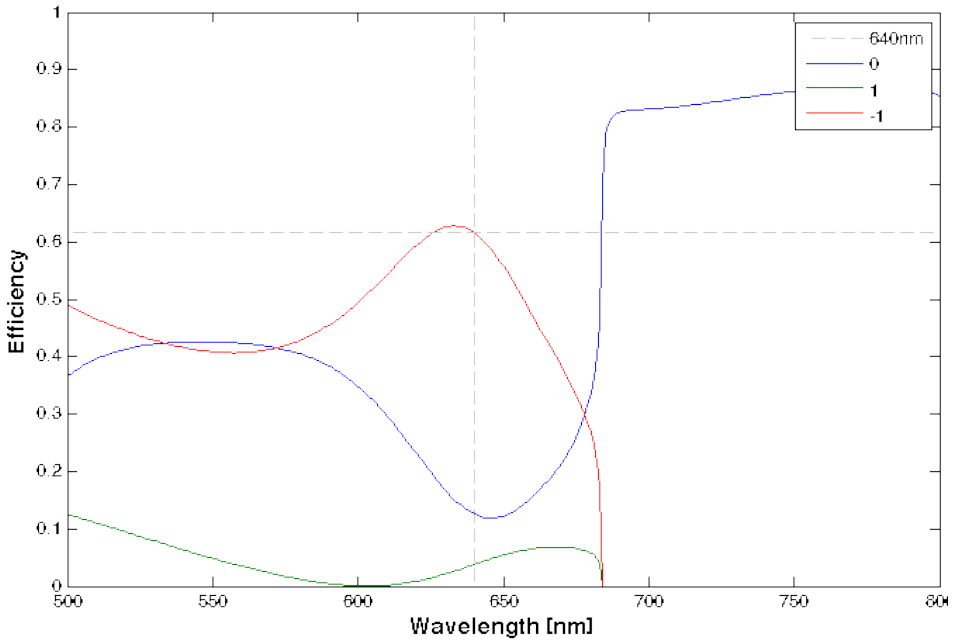

Figure 2.15 – Diffraction order efficiencies as function of the excitation wavelength. At 684nm we observe the first order transmission cut-off, where its angle reaches 90 degrees and it becomes evanescent.

better performance of the MS, since it would provide us with a wider effective index profile range, and thus a further-reaching phase profile up to the full 2-π. Unfortunately, this also leads to higher aspect ratios that are harder to fabricate. For similar reasons we also needed to filter out designs where both lines were closer than about 50 nm from each other ($b_X - (a_W + b_W)/2 < 50nm$), as this would generate an extremely narrow groove difficult to cleanly etch away to its full depth (also a high aspect-ratio but in depth instead of height). An first hand example of this limitation was rapidly found, shown in Figure 2.18, where a tested TiO_2 CCP RIE etching process was relatively successful for a low aspect ratio of 2, but insufficient for the same patterns etched 50% deeper with an aspect ratio slightly above 3. Ultimately this means that up to this point the performance of the metasurfaces is not inherently limited by their design but by the nanofabrication process in use, and the former will be almost automatically enhanced by any improvement achieved with the latter.

In this design generation, the smallest features are 48 nm wide, and the TiO_2 layer is 230 nm thick, resulting in a maximum aspect ratio of 4 or slightly higher if considering the possible overetching. This topic is further discussed in chapter 3.

2.5 2D Asymmetric metasurface

2.5.1 Structure and Numerical simulations

After the first nanofabrication series of the 1D metasurface design, it became apparent that a new structure was necessary, mostly motivated by a potential gain in performance thanks to the wider range of effective index that can be reached by a more flexible design,

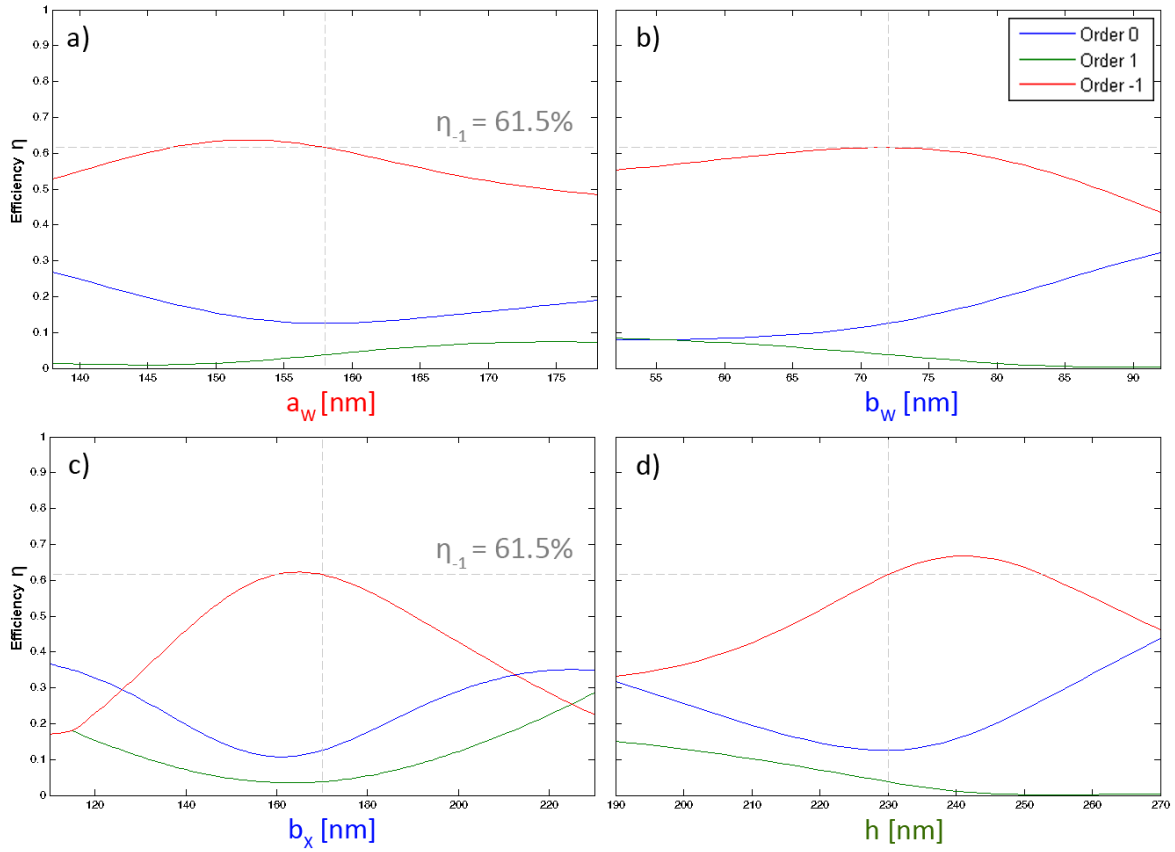

Figure 2.16 – Numerically calculated efficiencies for the three main diffraction orders as function of the design parameters shown in Figure 2.4. The smooth variation of each of the curves assures some level of robustness to imperfections that could arise during the nanofabrication. Later 2D metasurfaces were chosen prioritizing the reduction of the 0^{th} order efficiency η_0 before η_1, since light coupled into the substrate (orders 1 and -1) produces less potential scattering near the imaging system than direct transmission traversing the glass coverslip close to the biological sample.

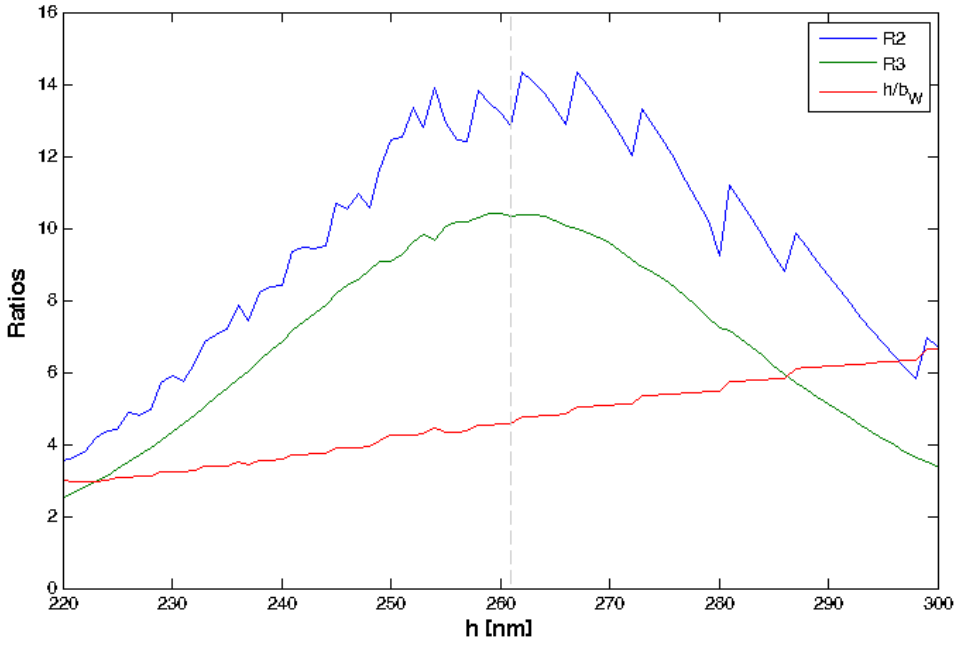

Figure 2.17 – Optimized R_3 figure of merit for different MS thicknesses h with no restriction over the parameters that define the structure, visible on figure 2.4 with the exception of the period p that is fixed by the first diffraction order angle α_1 required. The optimization done at each point disregards if the resulting aspect ratios for lines and grooves are within our current nanofabrication capability. We observe that more performant MS designs could be fabricated on thicker TiO_2 layers, responding to being able to apply a full 2-π phase on the incident beam when the MS is approximately 260nm tall.

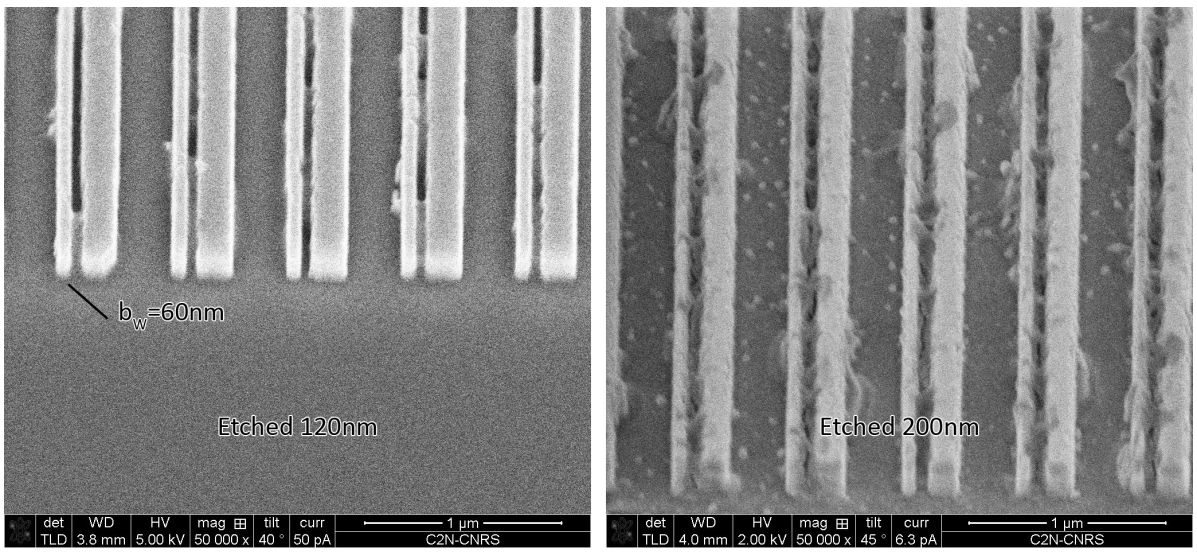

Figure 2.18 – Although much improved in later processes, this early SF_6/CHF_3 CCP RIE recipe test showed the clear difference between a process capable of fabricating low aspect ratio structures, against a more demanding design with higher aspect ratios. In this sample, the critical dimension is 60nm (b_W), which was within the scope of the process being test if an aspect ratio of 2 was sufficient, but was not for an aspect ratio slightly over 3. Higher aspect ratios are almost without exception harder to fabricate.

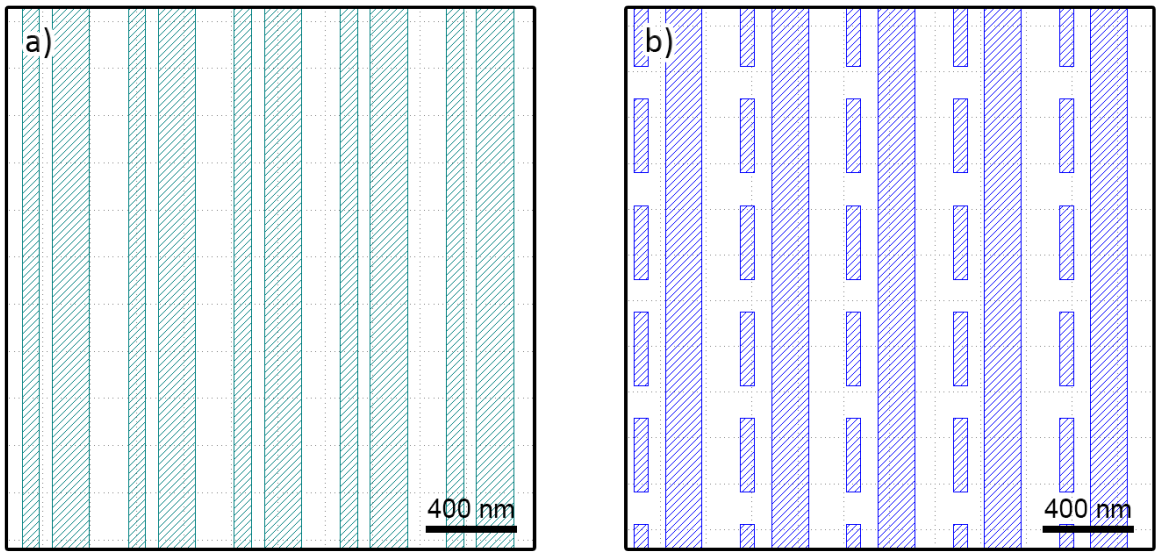

Figure 2.19 – Example layouts of the initial 1D Asymmetric double-groove (**a**) and one of our second generation 2D asymmetric metasurfaces (**b**). These are just one of many similar designs of each type optimized for different or figures or merit.

and no less important by improving the reliability and output of the manufacturing process. This section describes the process that led the evolution from designs of the type shown in Figure 2.19 (**a**) to 2.19 (**b**)

From the nanofabrication perspective, the 1D double-groove design presented three main difficulties:

1. Resist development: Regardless what the used fabrication process was, there is always a design transfer to a resist layer that will act as first, and sometimes only mask to be written with the electron beam. For both positive and negative resists, the old MS design required a thin ($\sim$ 50 nm) a long strip of polymerized resist that could occasionally collapse to the sides during its development. By segmenting this line, we can avoid one collapsing sector to pull and collapse the rest of the line, affecting a much larger area of the sample.

2. In all processes involving a liftoff step, (First generation process, Section 3.2), it has been almost impossible to have a good metal deposition in the bottom of a deep, narrow groove. The metal build up in the edges of the top level of the mask will either close the groove or severely affect the desired flat and homogeneous metal deposition in the lower level in direct contact with the titanium dioxide. Figure 2.21 exemplifies this undesired effect that will completely halt the fabrication process.

3. In the cases where the development and lift-off of a sample of the first-gen MS design were satisfactory, there was one last difficulty related with the way the etching rate of the MS material is affected by the shape and "openness" of the surface to the plasma. This is detailed in Section 2.3 where we see how it is easier to achieve an homogeneous etching result when the different sections to be etched are of comparable size and shape.

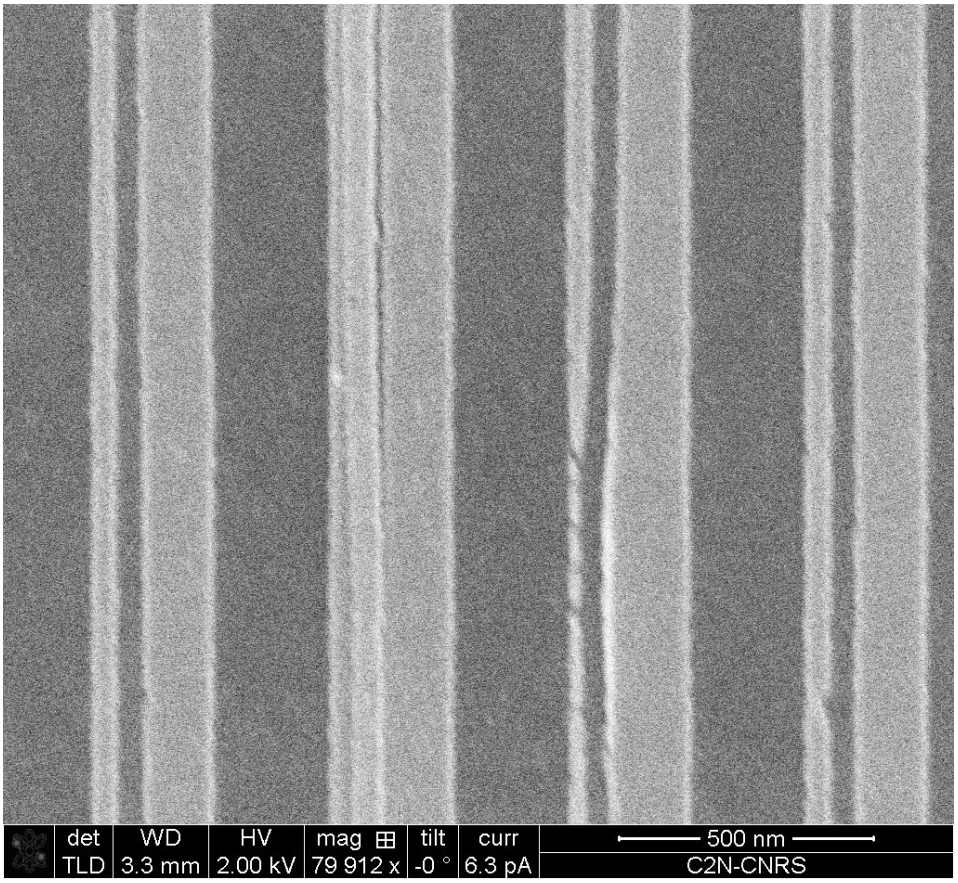

Figure 2.20 – Collapsed resist lines results in undulating lines on the following fabrication step.

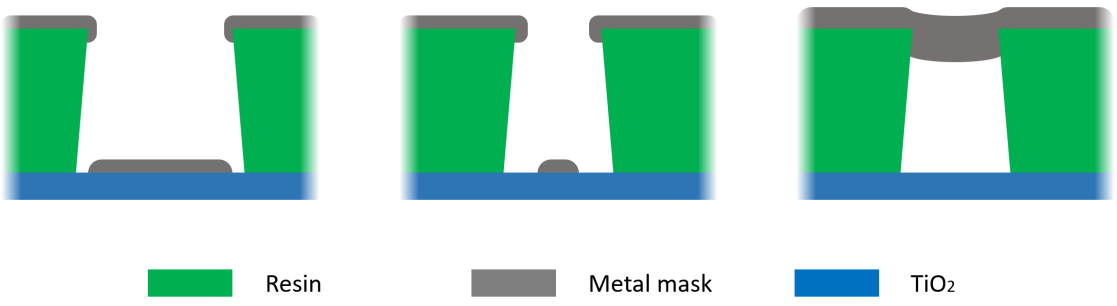

Figure 2.21 – Left: An optimal metal deposition over a resist mask with the right profile will generate an accurate metal mask reproduction in size and shape of the inverse of the resist mask. Center: As the openings in the resist mask become smaller, a point will be reached in which the size difference on the transferred metal patter will be significant, deteriorating the quality of the final sample. Right: On extreme cases with soft mask openings similar in size to the metal layer thickness, the gaps on the resist are closed up by the metal accumulation on the mask's edges and there is downright no pattern transferring.

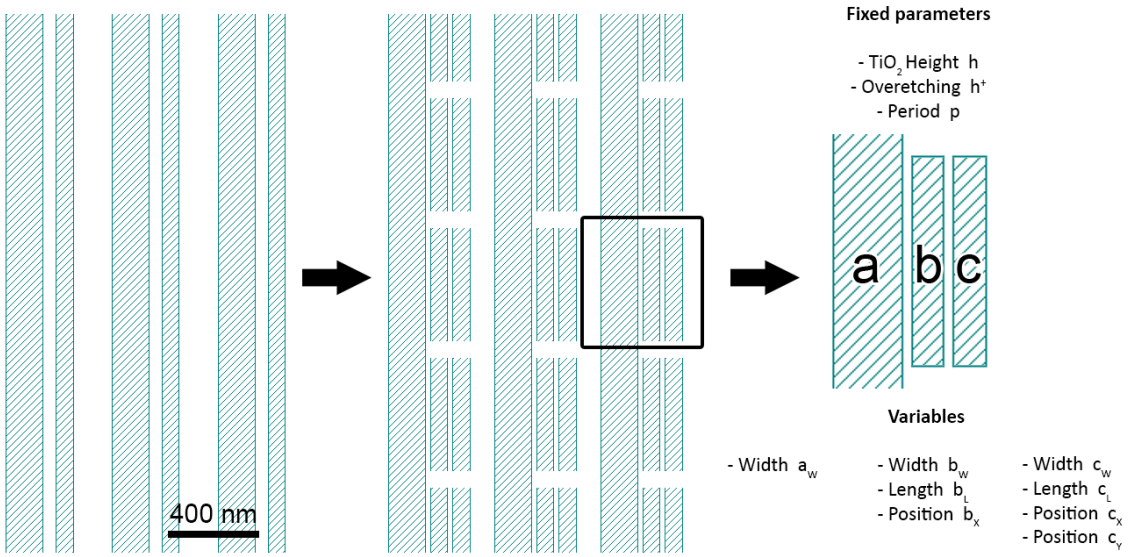

Figure 2.22 – Evolution of the original 1D MS design towards a 2D structure with 3 possible elements instead of 2. This new 2D design with its 11 defining parameters (of which 8 are variables used in the optimization) became our template to search for the optimal MS-TIRF metasurfaces.

To tackle these difficulties we sought a different kind of TiO_2 structure design, more resilient to localized defects, easier to etch and if needed, easier to transfer by lift-off.

2.5.2 2D Optimization methodology

The starting point was the previous 1D asymmetric design comprised of two continuous lines with grooves in between, but now with a third TiO_2 line added and 2 out of those 3 lines divided in segments along their direction, while the last one is continuous as before. While previously we had a surface with a 1D structure, now it also has a periodicity along the other horizontal axis. This 'template' design, shown in Figure 2.22, represents just a starting point for an optimization algorithm, and each of the parameters that unequivocally define one design is free to change with each optimization iteration. This 2D template consists of 1 continuous line or variable width a_W and two smaller elements free to take any size and position within the unit cell (black square in Figure 2.22). These degrees of freedom result in a total of 8 variables to work with, plus the period p (defined by the required TIR angle) and TiO_2 thickness h. The thickness h will continue to be 230 nm which offers a good compromise between performance and simplicity during fabrication, although it could probably be increased with relative ease using the latest nanofabrication processes that we developed.

While the 1D MS design optimization required the calculation of the figure of merit 50-100 thousand times, entirely possible using a portable computer, this brute-force approach was not an option with the 8+ dimensions of the 2D metasurface template. To tackle these designs, a much more efficient MATLAB script implementing a simplified version of a gradient ascent was developed. This iterative optimization method allows us to navigate the multi-dimensional matrix of parameters only in the direction that maximizes the value of the figure of merit chosen, using one random variable at the

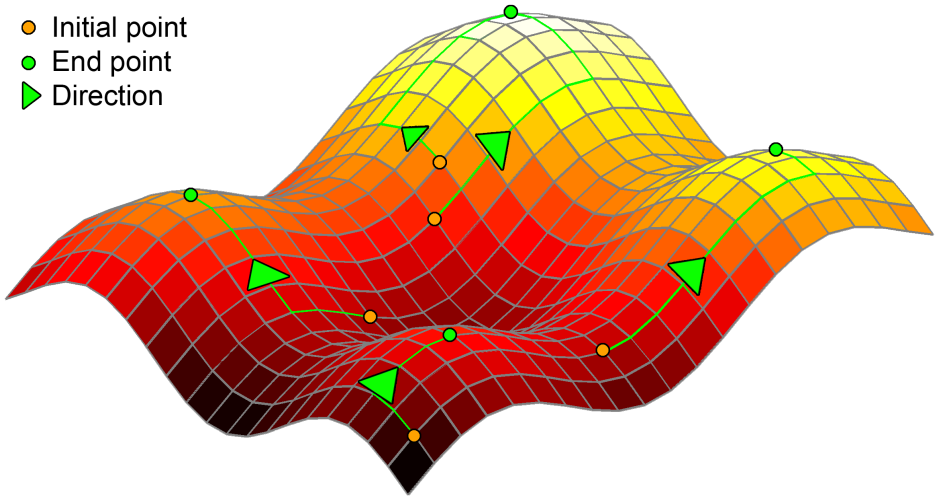

Figure 2.23 – Bidimensional analogy of the search algorithm used to find the local maximums of the 8-dimensional matrix of 2D MS variables. Starting from the initial random point (orange) one variable is adjusted in discrete steps as long as they increase the figure of merit calculated at each intersection. When this condition is no longer valid, another variable will be used to continue to increase it further, until no further increment can be achieved with any of the parameters in any direction. This whole process is repeated starting on another intersection, possibly resulting in another local maximum.

time. Using this strategy we can consider sets of $\sim 50^8 \sim 4\text{x}10^{13}$ different metasurfaces and find the very few with the highest figure of merit and then manually choose among those the best suited for our specific nanofabrication process.

Despite this method providing convergence only to a local maximum, the radical increase in speed allows us to run the algorithm multiple times starting from random initial values and check if we always converge to the same values. While this heuristic approach does not assure us we will necessarily obtain the global maximum nor all the local maximums for a given range of sizes, having previously observed the smooth behavior of the figure of merit function for a single parameter variation, we did not expect a large number of maximums. Additionally, if we assume an approximately uniform distribution of the local maximums and if we run the optimization algorithm n (e.g. 20) times on a range that includes m (e.g. 4) local maximums, the probability of never arriving to one of them is $P = (m - 1/m)^n$ (0.3% on the example). Alternately, if under these assumptions we only obtain 3 different maximums, then we can be 99.7% sure that we have found all the optimized configurations that we could have found. By the contrary, if there was a very sharp local maximum that we did not find with our algorithm, we know it would be challenging to fabricate and use, so our interested in it is limited.

Figure 2.24 shows an histogram with the figure of merit R_3 for a series of 300 optimization runs. The majority of the runs arrived to only 5 distinct design (with a local maximum for R_3) with at least 10 results. With the assumptions described above, the probability of having a 6th never-found maximum is just extremely small.

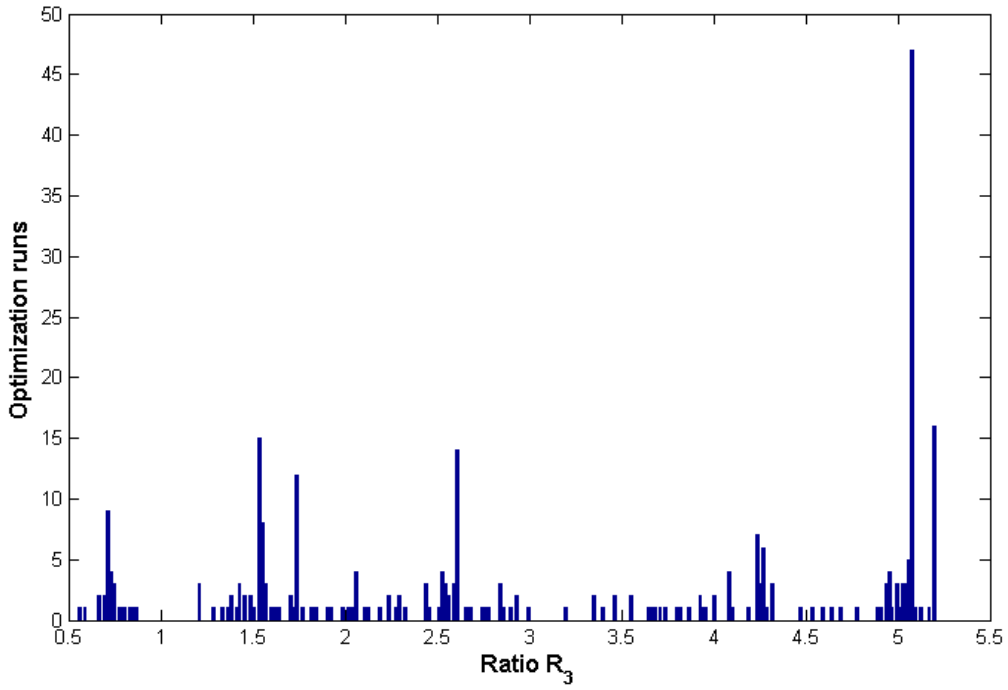

Figure 2.24 – Performing a gradient ascent optimization from hundreds of random initial points leads to a small number of designs with almost the same figure of merit R_3 ($\pm 10\%$). Being a periodic structure means that all results equivalent to a rigid displacement in the direction of the lines will outcome the same performance ratios. The R_3 values that came up just once are explained by the minimum gradient demanded to keep the optimization running, a mean to filter out extremely long and inefficient runs.

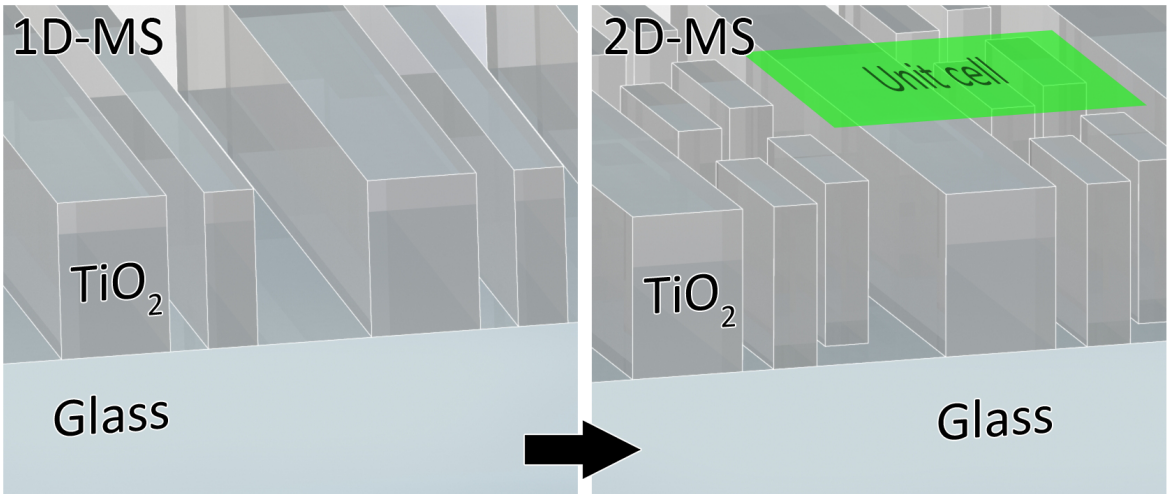

Figure 2.25 – Left: Render of the fabricated 1D metasurface grating Right: Render of the template for a 2D metasurface optimization. All the dimensions of the 3 objects visible in one period are free to take any value. The unit cell is marked in green.

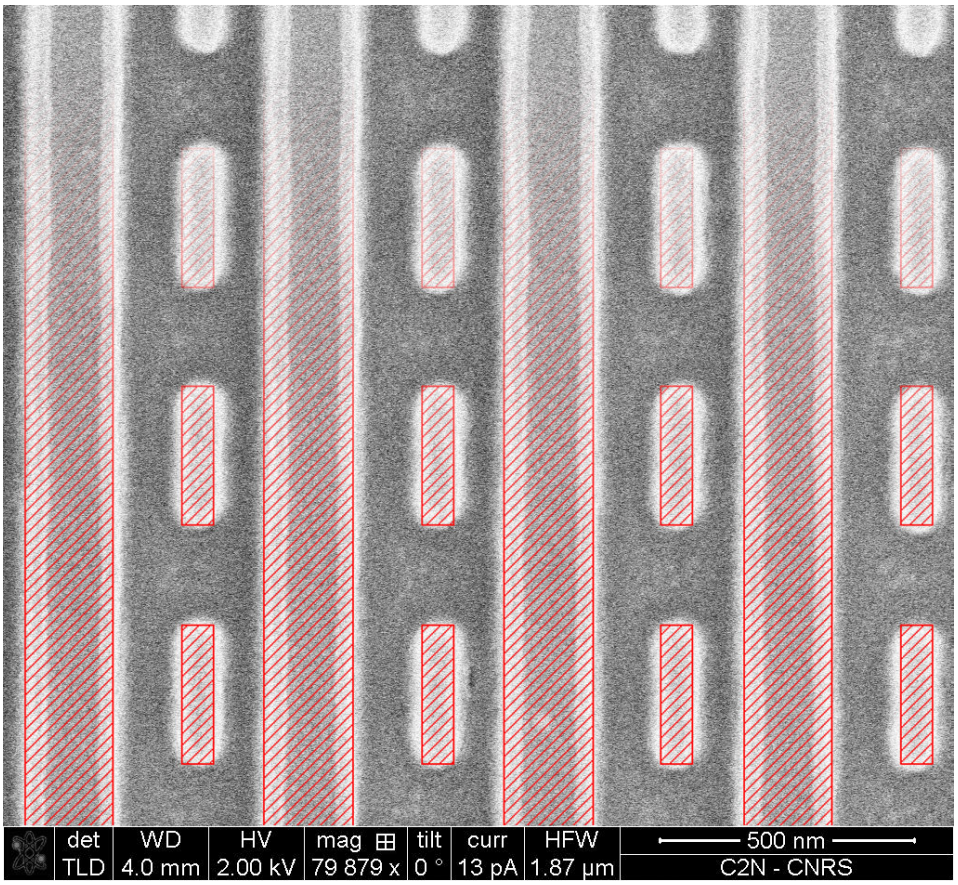

Figure 2.26 – While our initial simulations considered perfectly rectangular corners on the metasurface's elements, at this scale and with our processes it was an unrealistic condition. For this reason, this effect was taken into account in our most recent simulation code to improve the accuracy of the optimizations, with variations as large as 20% in some cases.

Edge shape on the simulated structures

After the first few fabricated samples of these 2D MS designs, it became evident that obtaining the sharp rectangular corners used in the simulations was not a realistic scenario, at least using our current nanofabrication process. To offset this discrepancy, we also incorporated the rounded edges seen on SEM images of the MS samples (Figure 2.26) back in our simulations, which modified our calculated figure of merit as low as 2% and as much as a 20% depending on the overetching of the sample, and its specific design and fabrication process.

2.5.3 Selected 2D Metasurfaces

Fixing $\lambda = 640nm$ and $h = 230nm$ and optimizing the figure of merit R_3 gave us 300 different structures, most of them clustered around 7 defined R_3 values as we see on the histogram on Figure 2.24. By grouping these designs by their performance and studying their common characteristics, as those 4 design results visible on Figure 2.27,

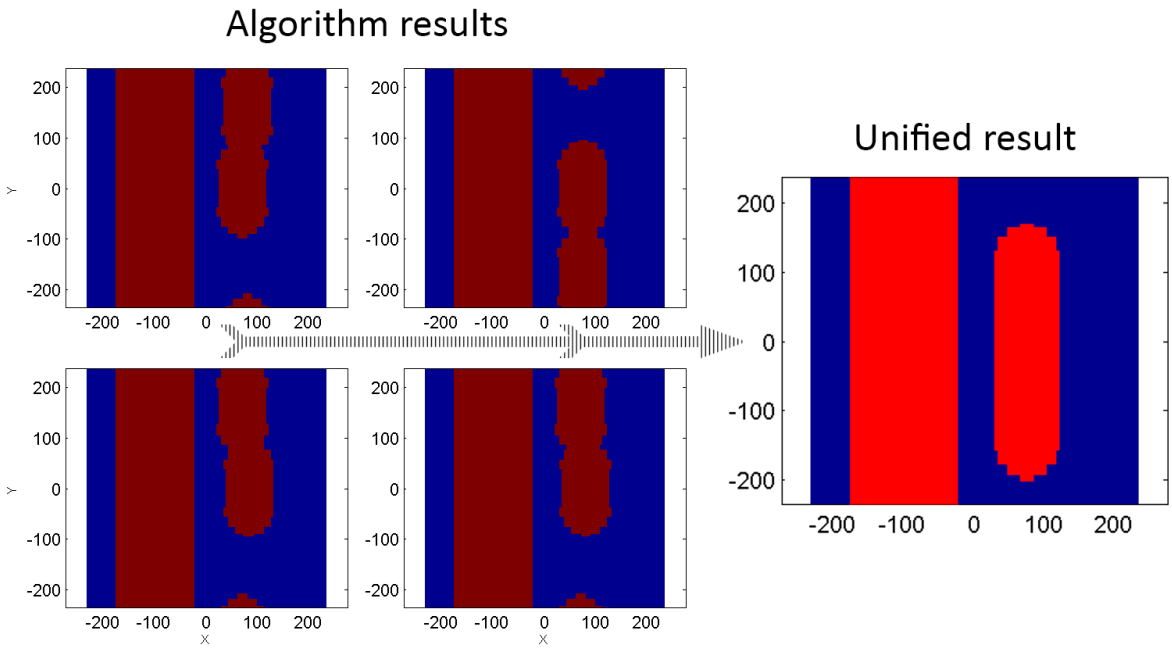

Figure 2.27 – From the set of designs with the highest figure of merit shown in Figure 2.24, a unified design is defined. These optimizations were performed by simulating rounded shaped structures as detailed in 2.26.

and removing any invalid or incompatible results[1], we selected one optimal metasurface to be used with $\lambda = 640nm$, described by $p = 465nm$, $a_W = 160nm$, $b_W = 61nm$, $b_X = 186nm$ and $b_L = 322nm$. Figure 2.28 **b** shows the vector files for this MS.

This process was repeated four more times for wavelengths between 630nm and 650nm, to obtain slightly different sizes that could accommodate an imperfect fabrication. As explained in section 2.4, we also repeated this algorithm to optimize the ratio R_2, which leads to a different distribution of light between the diffraction orders. For $\lambda = 640nm$ and $h = 230nm$ the selected design optimizing R_2 is defined by $p = 465nm$, $a_W = 172nm$, $b_W = 61nm$, $b_X = 215nm$ and $b_L = 271nm$ and is shown in Figure 2.28 **a**.

[1]For a given design characteristic, we can sometimes foresee its approximate fabrication outcome based on previous experience, and assess if it is worth a fabrication attempt.

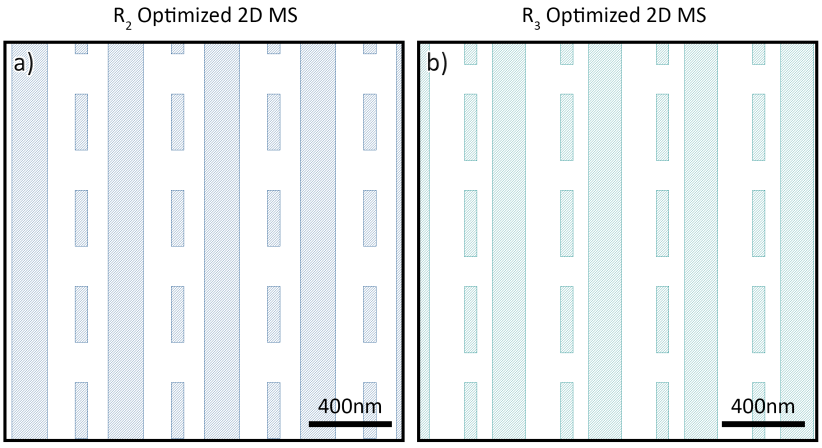

Figure 2.28 – Design files of the chosen 2D metasurface designs optimized maximizing the R_2 ratio (**a**) and R_3 ratio (**b**).

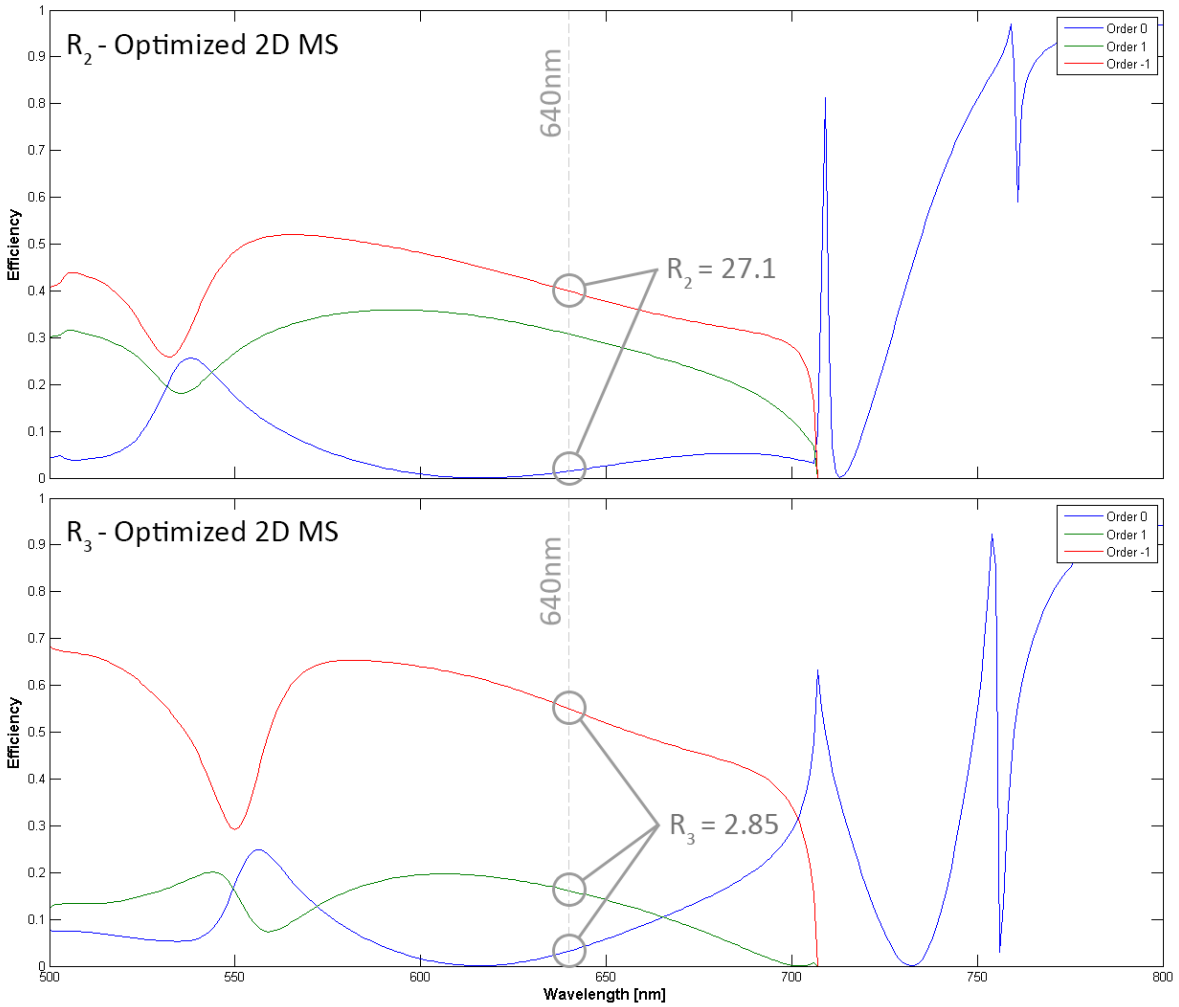

Figure 2.29 – Simulated response of the chosen 2D metasurface designs obtained by optimizing the efficiency of the diffraction order -1 against the order 0 (i.e. Ratio R_2) and against the sum of the orders 0 and 1 (i.e. Ratio R_3). At ∼680nm the first diffraction order angle reaches 90 degrees and they become evanescent, with their transmission efficiency rapidly dropping to zero.

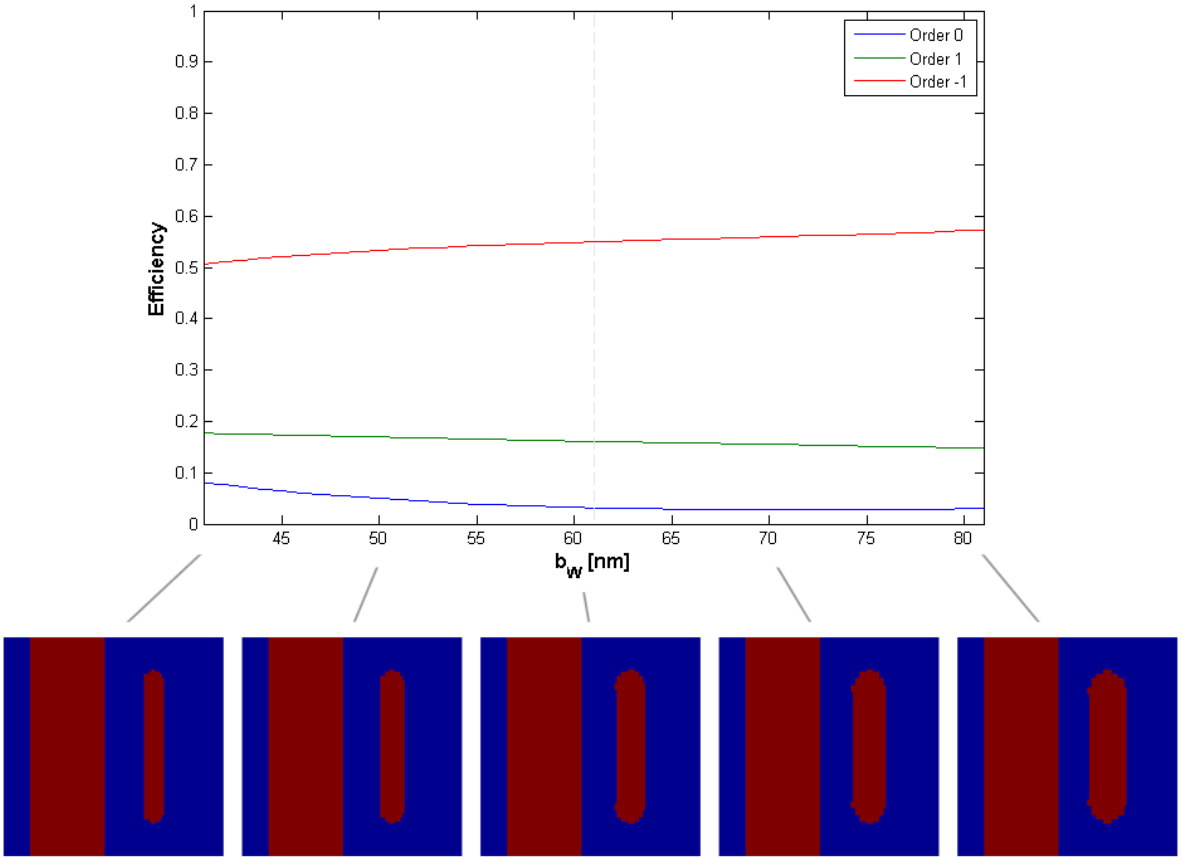

Figure 2.30 – Simulated response of the order efficiencies for the chosen 2D metasurface design (best R_3 version) for slight variations of the b_W width parameter.

For these two selected MS designs we simulated their wavelength response, visible in Figure 2.29. The smooth, non-resonant evolution around the light source design-value of 640nm is key to assure us that we are dealing with a MS that can be employed with several types of lasers around 640nm (632nm, 637nm and 640nm being popular options) without suffering a major performance penalty. On these two designs, we also simulated their robustness to variations on those parameters that are more prone to suffer deviations on fabrications, mainly during the development of the fabrication process. One example of such analysis can be seen in Figure 2.30 for the design optimized with the ratio R_3 and its parameter b_W, corresponding to the width of the smaller element. Similarly Figure 2.31 has the order's efficiency response for variations on a_W and b_X. In summary, we see that these variations are within a 5% from the nominal value when we simulate a 10nm size change on any of those 3 parameters, with an accumulated reduction in R_3 under a 18% in the worse case scenario (the order efficiency η_{-1} going down while η_0 and η_1 go up). While 18% drop in R_3 would be significant, the 10nm variation in size hypothesized is between 2 and 4 times above the resolution that can be obtained with a finalized and fine-tuned fabrication process, as well as above the resolution already achievable with our current process, making it an extreme case used to point out the robustness of these designs.

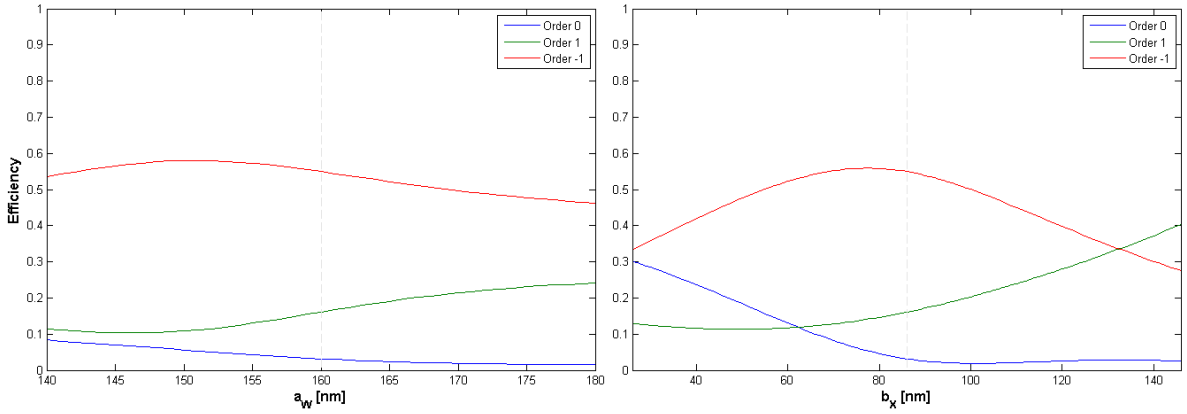

Figure 2.31 – Simulated response of the order efficiencies for the chosen 2D metasurface design (best R_3 version) for slight variations of a_W and b_X parameters.

2.5.4 Future designs

In parallel with the development of the nano-fabrication process for TiO_2 metasurfaces, the pursuit of increasingly better designs continued, leading to several designs that even though could not be fabricated during this work, are in several cases already compatible with our latest technological processes. Even those metasurfaces that are today beyond our fabrication capabilities remain of interest as we expect TiO_2 fabrication technologies to improve over time.

In particular, 2 designs stood out, with one of them already compatible with the latest process we developed (Section 3.5):

- Using the ratio R_3 as the figure of merit we obtained the pattern shown in Figure 2.32 using the same TiO_2 thickness $h = 230nm$ as before, for $\lambda = 640nm$ resulting in a efficiency for the first order almost 6 times higher ($R_3 = 5.83$) than the other 2 orders combined. This would be a valuable increase from the $R_3 = 2.85$ theoretical on previous designs. More importantly, the aspect ratios for the structures and gaps between them are lower than before which should facilitate the etching of the sample as well the lift-off if required.

- By just maximizing R_2 instead of R_3 we were led to a completely different structure with the potential of being an excellent metasurface design to almost completely extinguish the 0th order ($\eta_0 = 0.006$) while still coupling 39% of the incoming light into the order -1. The resulting theoretical R_2 ratio is over 65. With elements as narrow as 31nm (c_W in Figure 2.33), this design would require some further improvements on the fabrication process to attain such demanding 7.42 aspect ratio.

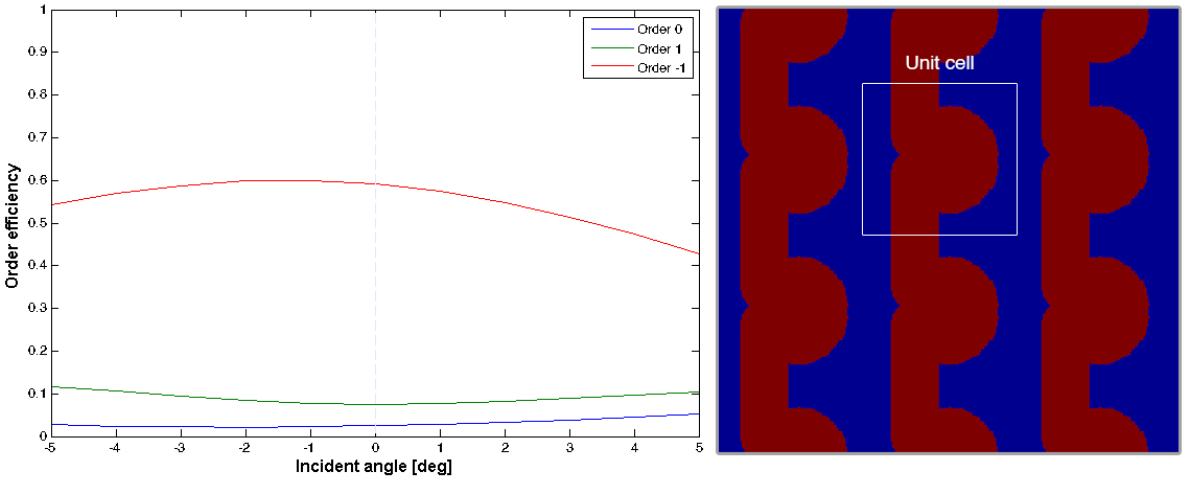

Figure 2.32 – Metasurface design with the highest ratio R_3 between the efficiency of one first order (-1) against the other two transmitted orders (-1 and 0) for $h = 230$, $p_X = 467nm$ and $p_Y = 467nm$, with a suitable aspect ratio for its fabrication. Its parameters are $a_W = 0nm$, $b_W = 149nm$, $b_X = 0nm$, $b_L = 498nm$, $c_W = 293nm$, $c_L = 255nm$, $c_X = 109nm$, and $c_Y = 218nm$.

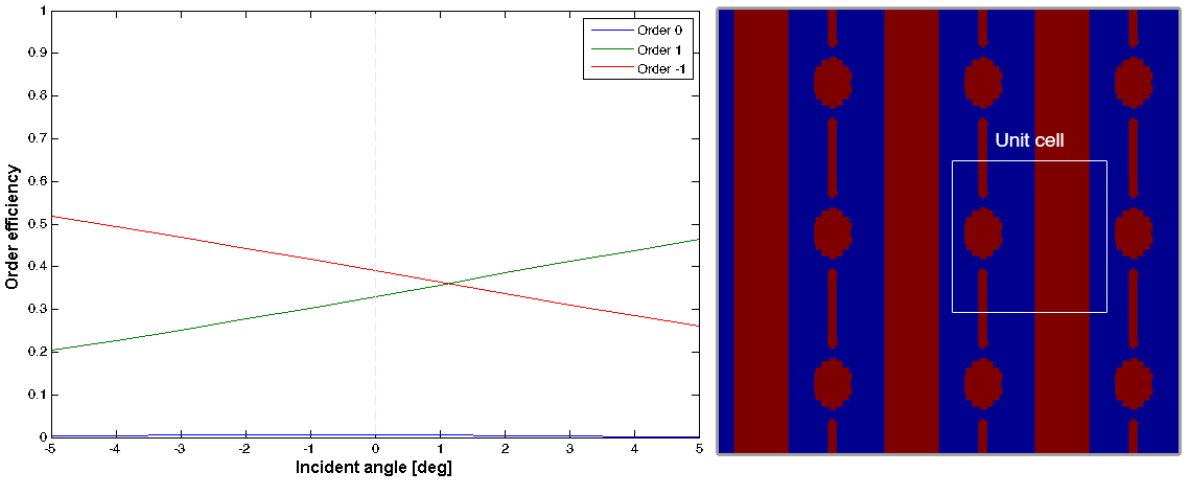

Figure 2.33 – Metasurface design with the highest ratio R_2 between the efficiency of one first order (-1) against the 0th order for $h = 230$, $p_X = 467nm$ and $p_Y = 467nm$. Its parameters are $a_W = 170nm$, $b_W = 112nm$, $b_X = 123nm$, $b_L = 153nm$, $c_W = 31nm$, $c_L = 246nm$, $c_X = 123nm$, and $c_Y = 234nm$.

Chapter 3

Nanofabrication

3.1 Introduction and generalities

As discussed in section 1.3.2 the fabrication process development of these nanostructured metasurfaces, referred as 'Nanofabrication' was one of the key aspects of this project. For the kind of devices we envisioned we knew we did not have a very large number of material options, offering very high refractive index in the visible wavelengths, being non-toxic and chemically inert. Titanium dioxide, a naturally occurring material, has got increasing attention over the last few decades for its use as a dielectric metamaterial thanks to its biocompatibility and high refractive index in the visible, 2.4@640nm for our amorphous TiO_2. This is well above materials like tantalum pentoxide (n$\sim$2.1 at λ=640nm [75]), hafnium dioxide (n$\sim$2.1 at λ=640nm[76]) or zirconium dioxide (n$\sim$2.2 at λ=640nm[77]) and similar to that of other biocompatible materials such as gallium nitride(n$\sim$2.38 at λ=640nm[78]), while being easier to work with. Metalenses [43, 31, 44, 30], solar cells [79], displays [80], and other optical components [53, 51] that benefit from a large refractive index and transparency in the visible added significant value to the technological processes required to shape and pattern TiO_2 structures and became evident that new fabrication processes had to be developed to keep up with those progressively more challenging structures. The processes described in this chapter were targeting the fabrication of patterns with critical dimensions as small as 48 nm on millimeter-large surfaces, with aspect ratios as high as 4.8 and as low as 1 in within the same structure. While higher aspect ratios in TiO_2 have been previously reported[51, 43], we sought to achieve similar results with simpler and faster processes, as well as compatible with more irregular shapes or uneven aspect ratios.

Generalities

When talking about pattern generation on a thin film, we can describe three large groups of techniques (and occasionally hybrid techniques as well), those that rely on material deposition, those that are based on mechanical deformation of the material and those that consist on material removal. In reality, while selectively depositing material may be a suitable option for some specific compounds (e.g. two-photon polymerizable resists for 3D printers), this is generally not the case for most substances. On the other side,

the list of materials for which there is a way to etch them is significantly longer, making this approach markedly more common. Thus:

- **Material deposition**: 3D-Printing and similar additive manufacturing techniques.
- **Mechanical deformation**: Techniques such as Nanoimprint lithography (NIL) are based on a mechanical deformation of a resist by a master template and could be seen both as adding material or removing material. These techniques are better suited for low cost, high throughput production once a well defined pattern has been chosen, as the template reusability provides no real advantage if the design is still changing between samples.
- **Material removal**: Standard etching techniques, which can also be divided into two main subcategories.
  - Wet etching, which consists on dipping a sample into a chemical solution that will dissolve the material on those places where is unprotected by the mask, transferring its shape and generating the desired pattern.
  - Dry etching, which consists on removing the masked material by exposing it to either a bombardment of ions (physical process) or ions and radicals (physical/chemical process) inside a plasma reactor.

Although a large number of advantages, disadvantages and differences between these two types of etching techniques could be mentioned, it could also be argued that the defining feature is the way they carve into the material: wet etching will isotropically[1] remove material by chemical interaction at any point where there is direct contact between it and the dissolving solution, whereas dry etching offers a whole range of plasma parameters that can modify the etching characteristics, from a very directional carving with high-energy ion bombardment to a very isotropic etching that may closely resemble that of a wet etching process. While wet etching can occasionally be a suitable option when the pattern's size range falls in the µm to mm scale, dry etching is the most popular option on the nanometer scale and when the etching profile desired does not match with the intrinsic isotropic characteristic of wet etching processes.

Among those ractive dry etching alternatives, fluorine-based and to a lesser degree chlorine chemistries have been used to etch TiO_2 thin films, with specific research done on these technologies as early as 2001[81]. Between those two options, fluorine has been generally the preferred option, producing the fastest etching rates[82, 83, 84, 81] and it is also the chemistry previously used in our laboratory[2] for the fabrication of blazed binary diffractive elements[51].

After the chemistry and etching technique has been defined, we need to evaluate and ultimately test different alternatives to generate the mask, which is closely dependent on the chosen chemistry. Three main aspects have to be considered and often compromised: the ease of fabrication, the quality of the pattern and the selectivity that it offers.

[1] With the exception of crystalline materials

[2] The label "our laboratory" refers to the team of people working continuously together under different institutional names since the realization of that work.

- **Ease of fabrication**: Although less quantifiable than the other items, a simpler process to fabricate a mask will often lead to fewer failures, better repeatability, and improved yield overall.
- **Mask quality**: With some specific exceptions[3] the final quality of the etched pattern on the thin film will not be higher than the mask that generated it. This is due to the unavoidable modifications to the pattern taking place with each transfer (from one mask to underlying material) incorporated in the complete nanofabrication process.
- **Selectivity**: Indicates the relative resistance against the etching process of the mask compared to the resistance of the material to be etched underneath (generally quantified as the planar etching rate ratio between of the thin layer material against the mask). It is strongly correlated with the plasma properties and it is the parameter that will ultimately define how long (or how deep) the etching process can be run until the mask has completely disappeared or it has been altered beyond an acceptable limit (dependent on the application or target accuracy).

Considering these 3 points and the fact that often e-beam resist masks are not etch-resistant enough to etch the underlying material directly, two main options are commonly employed for TiO_2: using that e-beam generated soft mask (i.e. the resist mask) to etch a more resistant hard mask (dielectric or metal); or use it to perform a lift-off with it, which generates such hard mask through a metallic deposition.

At the time of this work, we had both fluorine and chlorine-based dry etching chemistries available, with a Capacitively Coupled Plasma (CCP) Reactive-ion Etching (RIE) reactor (Nextral-Unaxis NE100) working on Sulfur Hexafluoride (SF_6), Fluoroform (CHF_3) and Oxygen, and an Inductively coupled plasma (ICP) RIE reactor (SENTECH ICP-RIE SI500S with a triple planar spiral antenna) equipped with various halogen gases including Cl-based gases (Cl_2, BCl_3, $SiCl_4$) and HBr. Based on the available literature[81, 85] and the in-house expertise mentioned above, our first TiO_2 etching tests were done in a fluorine plasma environment on a CCP RIE reactor, performing a lift-off to generate a metallic hard mask, as a direct adaptation of the process used previously in our laboratory[51]. That work served as our starting point for the development and refinement of 4 different fabrication technologies detailed in the following sections, with gradually increasing capability and reliability.

3.1.1 Aspect ratio dependent etching (ARDE)

One effect that we expected and observed common to all the processes described in the upcoming sections is the aspect ratio dependent etching. For a given pattern, such as that of Figure 3.1, the horizontal size of its etched sections shown as S_1-S_2 and the desired depth h (equal to the layer's thickness) will result in an aspect ratio. This effect refers to the difference in etching rates observed when the pattern contains features with very distinct aspect ratios, leading to narrower sections, like S_1 in the example, to be insufficiently etched by the time wider sections like S_2 have been fully etched. This undesired effect that has been studied extensively for other processes, in particular for

[3] In microelectronics sometimes the edge smoothness can be improved during the pattern transfer.

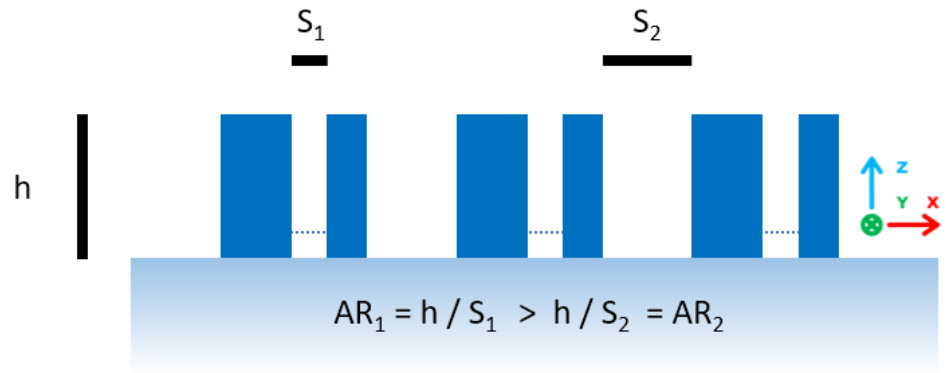

Figure 3.1 – Side view of an arbitrary pattern whose design require sections with different aspect ratios S_1 and S_2 to be etched to a depth of h. The ARDE effect will cause that by the time S_2 is fully etched, S_1 has not reach the nominal depth h. The stronger the aspect ratio dissimilarity, the stronger the depth difference (exemplified with a dotted line in S_1. The aspect ratio of the gaps is not to be confused with the aspect ratio of the structures (in blue).

silicon[86, 87, 88], has many undesirable consequences on the fabricated samples and can often be a limiting factor in terms of design freedom of the structures. Among other things, it has been one of the deciding factors when choosing between different metasurface designs of similar theoretical performance, as discussed in Chapter 2.

3.1.2 SEM Inspection

Certainly one of the most important tools used to evaluate the results and performance of a particular fabrication process, not only in this project but in almost any other nanofabrication task is the scanning electron microscope (SEM). This type of microscopy works by scanning the surface of the sample with a focused beam of electrons and as such it is particularly suitable for electrically conductive samples than can discharge that incoming current away. This is so important to the proper functioning of the device that until the advent of the very latest generation of commercial electron microscopes, imaging uncoated[4] nonconductive samples was almost impossible to do. Thankfully nowadays samples like our dielectric metasurfaces can be imaged directly in some cases, although we cannot expect the same level of detail and general ease of use than that can be achieved when imaging a conductive or metallized sample. In this work, we opted to image our samples both coated and uncoated depending on the specific metasurface and measurements needed, as a 4-5nm additional conductive layer (typically aluminum or amorphous carbon) could, in same cases, affect in noticeable ways the topography that we aimed to visualize. The SEM unit used in this project is a Magellan 400L (FEI, 2008).

[4]Without a conductive layer, often a thin metallic deposition.

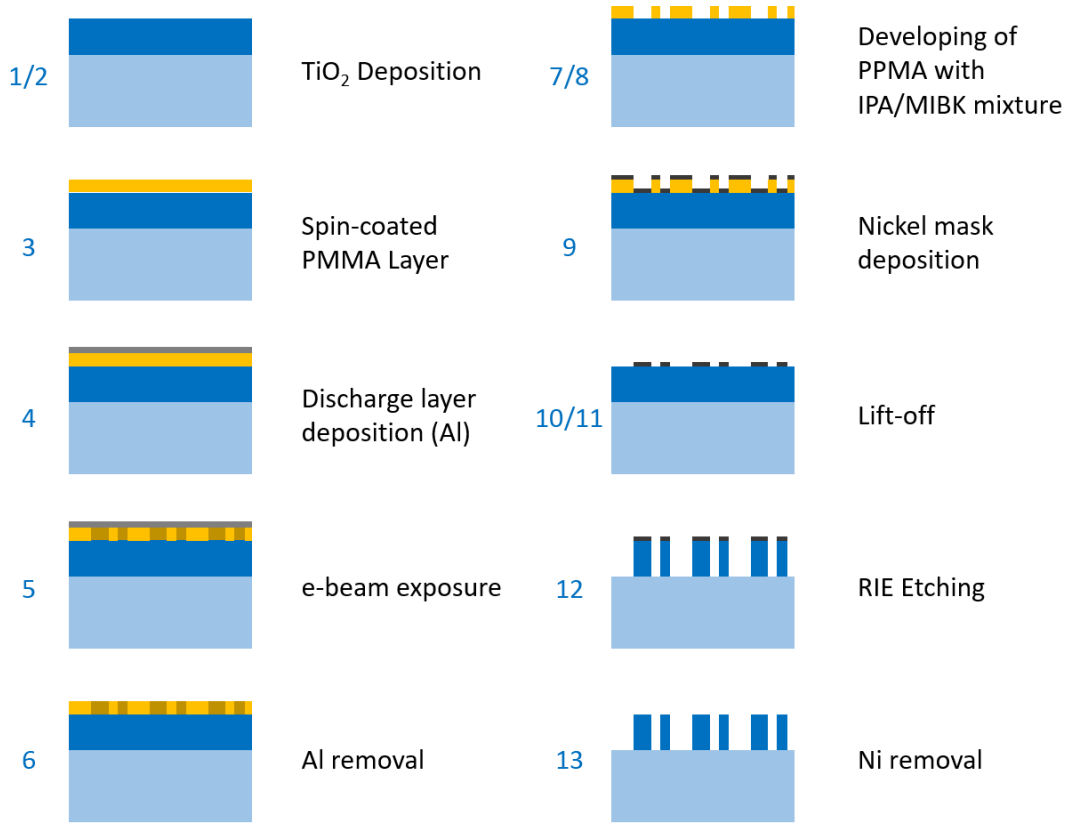

Figure 3.2 – First generation fabrication process for TiO_2 on glass metasurfaces. A detailed description of the process is found in Appendix .2

3.2 First-generation process: Single layer Lift-Off

This process, adapted from an older technology developed in our lab, can be summarized as a double pattern transfer (using a resist soft-mask and a metal hard-mask) followed by dry etching of a titanium dioxide layer, with a lift-off intermediate step to transfer the pattern between the soft and hard mask. A detailed description of the process, including the initial TiO_2 layer deposition method, is found in Appendix .2.

3.3 Second-generation process: Bilayer soft mask

The first major modification to our original nanofabrication process came in to tackle difficulties encountered during the lift-off of the secondary mask (Nickel). Despite the lift-off technique has proved itself as a relatively simple and reliable technique since its introduction at least 40 years ago[89], the evolution towards higher and higher resolution on electron beam lithography also pushed toward increasingly higher e-beam energies. This in turn makes the sidewalls of an exposed resist more vertical whereas a good lift-off requires and slight undercut profile that forces the metal deposited on top of the resist to be physically disconnected from the metal deposited on the substrate. This a key aspect of the technique and it is particularly important when the structures are as small as on our metasurface designs. Figure 3.3 exemplifies what the resist profile should resemble to ensure an accurate metallic mask (left) and what is the effect of a

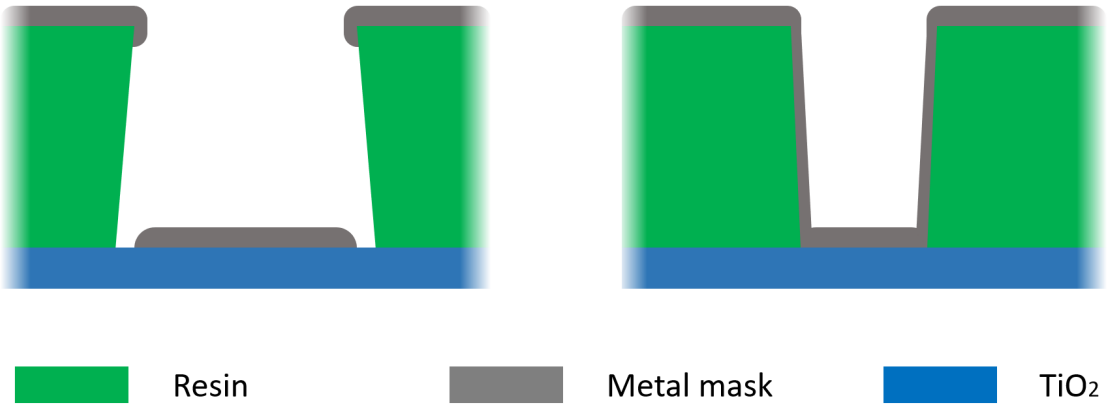

Figure 3.3 – An undercut profile (left) allows for a clean separation between the metal mask in the substrate and the metal excess that needs to peel away when the resist is dissolved. A vertical resist profile (right) often leads to a continuous metal layer that not only will not segment as necessary but occasionally will not even let the resist to be dissolved by the TCE.

positive slope resist profile, generating an undesired continuous metal layer (right). This last case was a recurrent issue with the first generation process, with uneven metallic mask edges like those visible in Figure 3.4.

When the electron beam characteristics in conjunction with the specific resist used does not result in a favorable profile to manufacture a given size by lift-off, a bilayer approach can be a feasible alternative to favor the undercut profile needed[90]. This technique consists on replacing the single-layer resist layer for 2 layers with slightly different sensitivities to the electron beam, using two separate resists. For a given dose, the more sensitive bottom layer will develop into a larger opening than the upper layer. By carefully adjusting the thickness and type of each layer we can reproduce a satisfactory undercut profile and greatly improve the quality of the lift-off. For our structures we chose a bilayer stack composed of a less viscous version of PMMA (A2) as top layer, and MMA (17.5EL10) as bottom layer. With each of them being approximately half the thickness of the older PMMA-only layer, the resulting final height of the new dual-resist mask remains similar. Even using the maximum speed that our spin coater could offer, a ∼50nm-thick layer of MMA required further dissolution of the MMA EL10 resist, with 1 part in 2 parts of anisole thinner to achieve a satisfactory 60 nm bottom layer (spin coated at 6000RPM). The development of this dual-resist mask after the e-beam exposure is a shorter version of that of the PMMA only layer, with only 30 seconds in MIBK/IPA (1:3) solution and the standard 10-second IPA rinse.

3.4 Third-generation process: Etched Aluminum hard mask

While up to this point all the fabricated samples required a lift-off to create the metallic mask, resulting in some satisfactory samples, we noticed that the lift-off was often

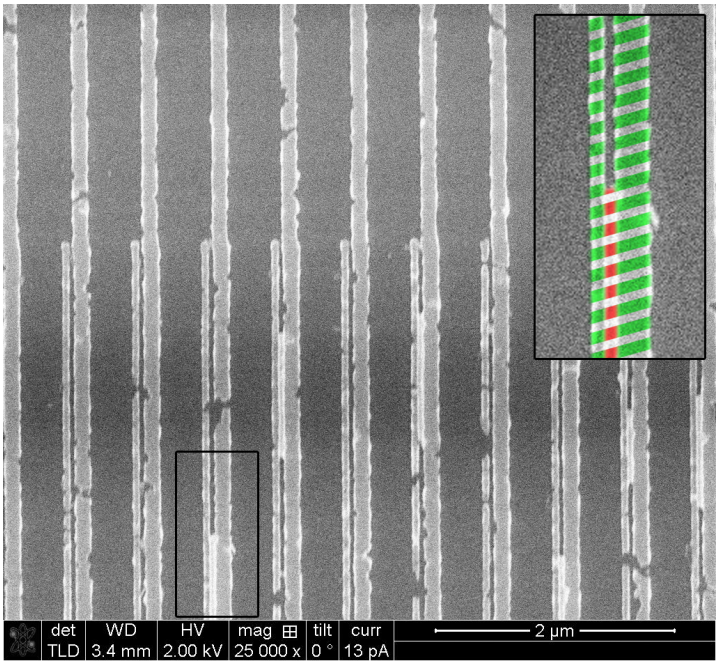

Figure 3.4 – Even a thin metallic layer connecting the two levels of the soft leads to fragmentation of the future metallic mask deteriorating the edges and creating small metallic fragments that spread and stick on the surface rendering the mask useless. Inset: Close up of the framed section, with the parts of the mask that should remain after lift-off(green) and should have been removed(red).

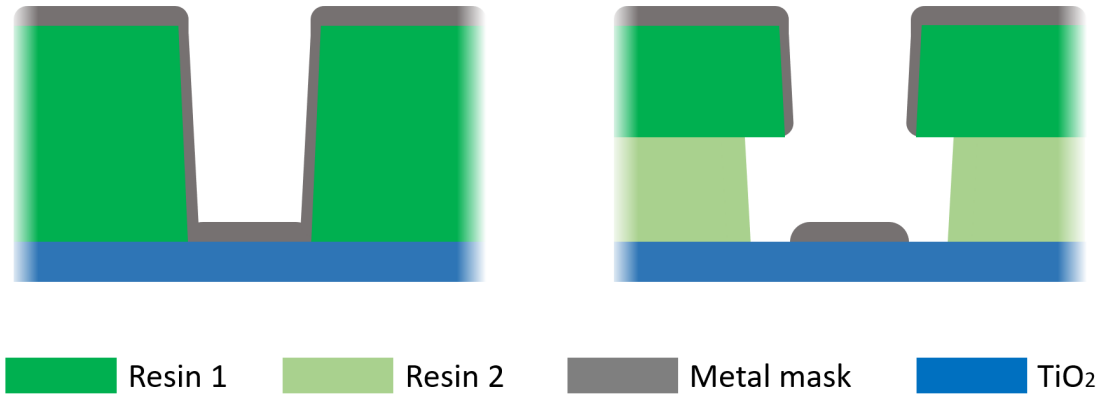

Figure 3.5 – When the undercut profile (left) cannot be achieved with a single resist layer due the particular characteristics of the electron beam exposure (beam energy, thickness of the resist, size of the pattern, etc.) a dual layer configuration (right) with a more sensitive bottom layer can generate an undercut even if the sidewall slope is positive for each individual resist. Our process used a top A2 PMMA layer and EL10 MMA underneath.

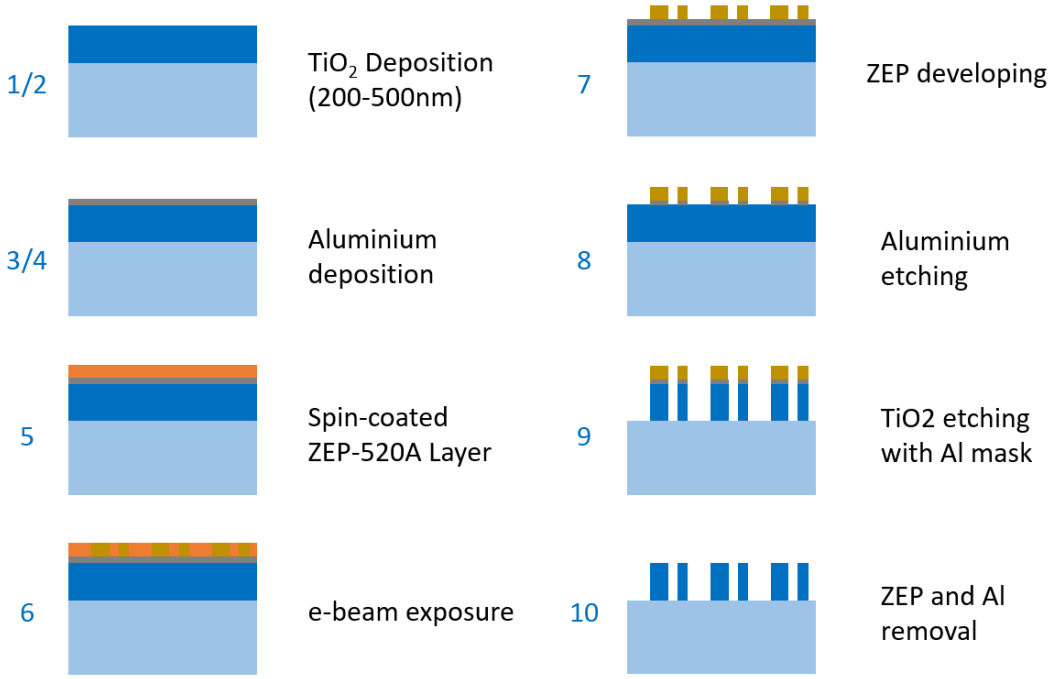

Figure 3.6 – Third generation fabrication process for TiO_2 on glass metasurfaces. A detailed description of the process is found in Appendix .3

the most problematic step of the process. This was due to the difficulty of lifting-off the relatively thick[5] Ni patterns necessary to compensate the limited selectivity of our TiO_2 CCP etching process, in an homogeneous way and defect-free over a challenging surface as large as 4mm x 4mm in some cases. This motivated us to develop a different technology that did not rely on a lift-off mask altogether, performing a metallic mask dry etching instead. This alternative technique is not only more repeatable but it also allowed us to attain a hard mask of the required thickness avoiding all the inherent thickness limitations of a lift-off.

This new approach consisted on depositing an aluminium layer, spin-coating it with ZEP-520A[6], and use this resist as a soft mask to etch the Al layer in a chlorine-based ICP plasma, turning it into an Al hard mask. Contrary to a lift-off that is a manual procedure and transfers the inverse layout of the soft mask into the hard mask, this new process is fully automated, more repeatable and replicates the soft mask into the hard mask, without inversion. In turn, this change requires inverting the MS design vector file and exposing the area surrounding the metasurface elements (instead of exposing over the MS elements as before). Despite Ni offering higher selectivity against TiO_2 than aluminium, the dry etching of nickel is a rather complicated process involving highly dangerous compounds[7] and it was thus not considered as a viable option. The resist change from PMMA to ZEP-520A is an adaptation to the change in the hard mask material, to have good selectivity on the chlorine-based ICP Al etching. The resulting process is detailed in Appendix .3

[5]In comparison to the soft mask's thickness of only 100nm.

[6]High resolution positive electron beam resist by ZEONREX Electronic Chemicals, compatible with chlorine-based dry etching processes.

[7]Nickel Carbonyl is the only known volatile compound of Ni[91, 92], a highly dangerous compound according to United State's Centers for Disease Control and Prevention.

3.5 Fourth-generation process: Direct soft mask etching

Most of the ∼50 fabricated MS samples were meant to test and solve one specific process obstacle. Some of these technical challenges could be tackled with minor modifications of the process currently in use at that moment and some others forced us into investigating entirely different alternatives, leading to a new process. Whereas the lift-off technique to generate a hard mask pushed us from the single-layer soft mask into a bilayer mask ("Gen2" in section 3.3) and later into a process with no lift-off at all ("Gen3" in section 3.4), the main motivation for this last process was the quality of the TiO_2 etching and simplicity of the process as a whole, improving its reliability.

This last process comes as a sub-product of the tests performed when developing a suitable ICP chlorine recipe for the aluminium hard mask etching on the "Gen3" process and relies on exploiting the typically already high resistance of the ZEP-520A resist in conjunction with an newly developed ICP etching recipe whose selectivity is high enough to etch at least 230nm of TiO_2 using just a single soft mask. In practical terms this means roughly a 25% reduction on the time employed for a single fabrication (around 6 hours in optimal conditions) and an increased resolution due to the lack of a intermediate pattern-transfer between the soft and hard mask as it was the case on all previous processes. Despite the only 8 samples fabricated with this latest method, insufficient for any type of statistical comparison, a higher yield and repeatability is observed thanks to the overall simpler technology. The process is detailed in Appendix .4.

It is worth noting that the new ICP etching recipe for TiO_2 is also compatible with a Ni mask generated by the bilayer soft mask process of Section 3.3 and even after a 10% overetching of the 230nm TiO_2 layer, the Ni mask was not fully etched. The vertical profile on the TiO_2 also indicated that there was no noticeable lateral etching, meaning that an bilayer soft mask with chlorine-based ICP etching could be a feasible option, not yet explored in the time frame of this work. Even if the selectivity obtained with ZEP is sufficient for our current TiO_2 layer thickness, Ni is likely to be offering an even higher selectivity, potentially interesting for the future designs discussed in Section 5.2.

3.6 Results

A significant fraction of this project's efforts were put into the nanofabrication task, starting with some limited experience from a project that took place almost twenty years ago in our lab[51], and with the final goal of a reliable and accurate fabrication process for TiO−2 metasurfaces. Closely related to those two factors was the simplicity of the process, which was not only aimed to improve both of those aspects but that also meant more samples fabricated using the finite resources of time and equipment, a hugely important factor for the microscopy side of the project. In this section we go over the different challenges found, how we faced them, our results and the experience acquired on this undertaking.

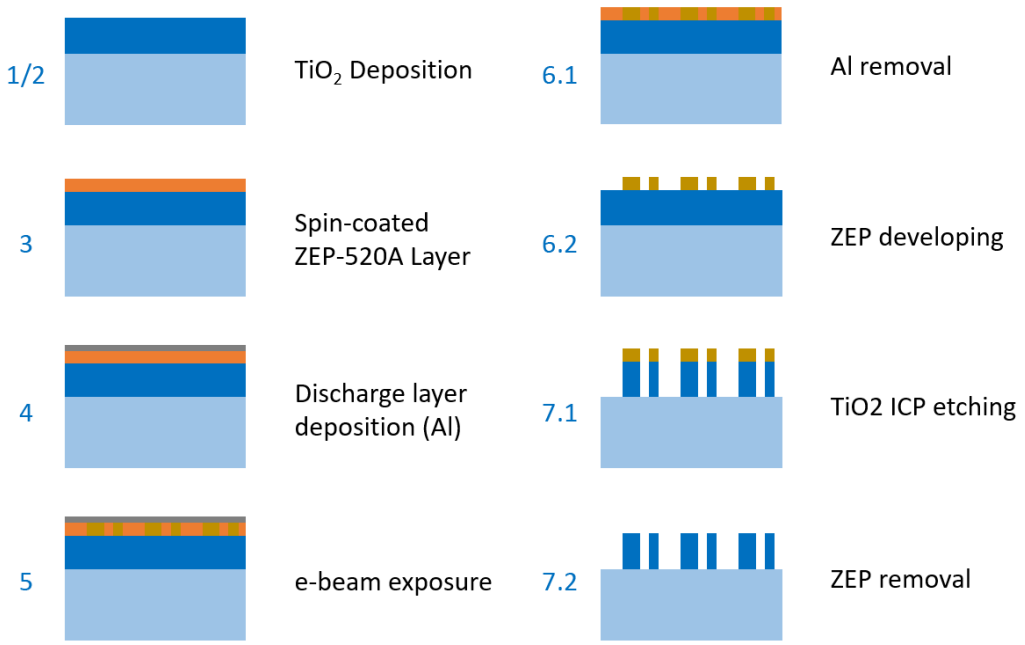

Figure 3.7 – Fourth generation fabrication process for TiO_2 metasurfaces on borosilicate glass substrates. A detailed description of the process is found in Appendix .4

3.6.1 Samples

Despite the different reasons that motivated the evolution from one fabrication process to the next, all process employed in this work provided at least some degree of success, even if not fully matching the metasurface requirements or expectations for that technology. Figure 3.8 shows a rundown of 3 metasurfaces fabricated with the PMMA single-resist process (SEM images a and b), the MMA-PMMA bilayer process (c-d) and the direct ZEP etching process (e-f), representing the 1^{st}, 2^{nd} and 4^{th} generation processes. The PMMA samples a-b were etched on a fluorine plasma (SF_6/CHF_3 CCP-RIE) and show a trapezoidal etching profile and an underetched narrow groove of 40nm, for a design that has a 55nm nominal value, due to the ARDE effect. Additionally, later tests also revealed a depth difference between the two grooves of over 30%. Both the profile and size distortions are improved in future 2D MS designs and fabrication processes, with the latest direct ZEP chlorine ICP etching process (4^{th} gen.) used for samples e-f being faster and more reliable than the bilayer lift-off based process (2^{nd} gen.) of the c-d metasurfaces. The 3^{rd} generation process, not shown in Fig. 3.8 was quickly replaced after several fabrication tests made on a silicon substrate revealed that although we could obtain a high quality aluminium hard mask, even thicknesses as high as 80nm were not sufficient for the CCP RIE fluorine TiO_2 etching (see Figure 3.13).

3.6.2 Electron beam lithography

Along this project we used three e-beam[8] lithography positive resists, Polymethyl methacrylate (PMMA by MicroChem Corp.), Methyl methacrylate (NANO™ MMA (8.5) by MicroChem Corp.) and ZEP520A (ZEONREX Electronic Chemicals). Al-

[8]PMMA is also compatible with x-ray and deep UV lithographic processes.

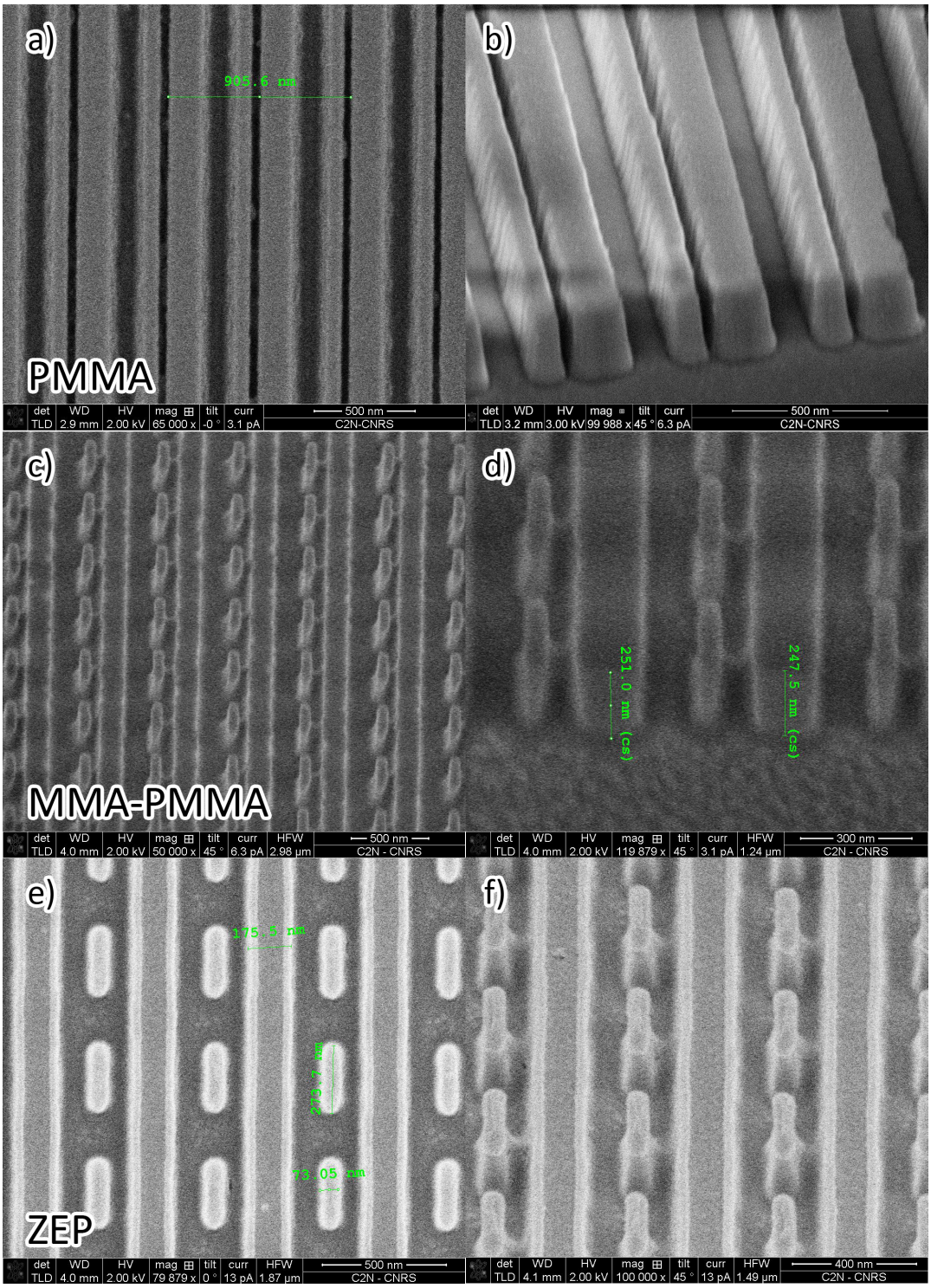

Figure 3.8 – (**a-b**) 1D MS fabricated with the 1^{st} generation process (PMMA + Lift-off). Showing relatively smooth edges but a strongly trapezoidal profile of the etching walls, its optical performance was not satisfactory. The large difference in the size of the grooves constantly led to a strong aspect ratio dependent etching effect, which is difficult to accurately predict and include on the simulations. (**c-d**) 2D MS sample fabricated using the 2^{nd} generation process (bilayer soft-mask + Lift-off). This technique allowed us to thicken the hard-mask while still obtaining a successful lift-off, giving us more flexibility on the TiO_2 etching recipe, ultimately improving the walls profile and optical performance.(**e-f**) The final process developed, a direct TiO_2 etching with a single ZEP resist soft-mask not only allowed for a faster fabrication overall but also offered a cleaner structure, with minimal defects and a highly vertical etching profile.

though the doses used are relatively standardized, the different sizes, thickness and dilutions have an impact on the optimal dose for a specific pattern and in consequence, a dose array fabrication is generally the first step. We realized several stepped-dose arrays with increasingly finer increments to finally find what we considered to be the optimal dose for these types of structures.

- **PMMA**: Doses between 300 and 900 µC/cm^2 were tested, with best results achieved for 450-550 µC/cm^2. Manual size compensations are required to reach the right size on the wide and narrow lines simultaneously (parameters a_W and b_W). This dose is matched with a 50-second development in MIBK/IPA and 10-second rinse in IPA and will need to be increased if the development is shortened. Only used for 1D MS designs.
- **PMMA-MMA**: From the first 400 to 800 µC/cm^2 tested on 25 µC/cm^2 steps, we narrowed it down to 600 to 650 µC/cm^2 paired with a shorter 30-second MIBK/IPA development and a 10-second IPA rinse. Used for 1D and 2D MS designs.
- **ZEP**: Our best results with ZEP resist were obtained using doses of 140-160 µC/cm^2, significantly lower than the doses used for the other resists in this project. This reduction on the dose by a factor of 4 allows for a 50-60% faster writing, only limited by the maximum frequency of the electron beam system. Used for 1D and 2D MS designs.

While many aspects of the metasurfaces were highly influenced by the process used for their fabrication, namely characteristics such as the profile, size, or surface quality of the structures, the period accuracy of the gratings only depends on the accuracy of the e-beam lithography system and was consistently well under 1% of the nominal values, with an absolute error Δp nearing 1nm.

3.6.3 TiO_2 deposition

The thickness of the amorphous TiO_2 layer, chosen to be h=230nm in all cases and kept constant until a nanofabrication process is fully refined, has been measured in several instances with an ellipsometer (HORIBA UVISEL) and its measured thickness ranged between 228nm and 232nm, roughly a 2% variability across the 22x40mm and 25x50mm microscopy coverslips. It's extinction coefficient is negligible at the visible range (undetectable by our ellipsometer, with some publications[93] giving an order of magnitude of 10^{-3}) and its measured refractive index is over 2.4. It has been deposited with a Plassys MEB 800 IAD e-beam gun system.

3.6.4 Bilayer soft mask

Figure 3.10 (**a**) shows an SEM image of a single resist soft mask process (1^{st} Gen Process, Section 3.2), with an unsatisfactory PMMA resist profile after development. This led to a metallic hard-mask (Nickel) that is not segmented between the bottom of the grooves and the top of the lines (see Figure 3.3) making the lift-off impossible. We observe Nickel fragments scattered on the surface and hard edges where it broke away. On the

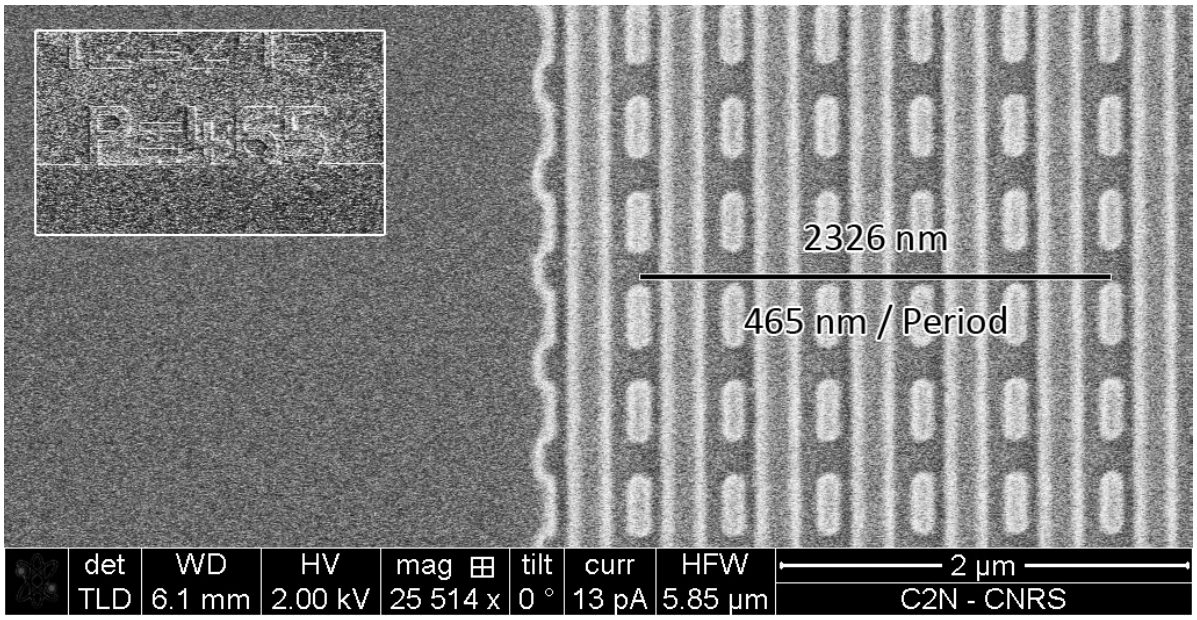

Figure 3.9 – Regardless the fabrication process utilized, the period of the fabricated MS gratings has been consistently within 1nm of their nominal values, resulting in an error under 0.5% on the measured diffracted angles (Subsection 4.1.1)

contrary, Figure 3.10 (**b**) shows the result of a successful lift-off achieved using a bilayer MMA/PMMA soft mask that forces the necessary undercut profile when said mask is developed (2^{nd} Gen Process, Section 3.3).

The **A** character visible on the MS label of the sample shown in Figure 3.11 let us verify the quality of the bilayer soft mask profile in an unexpected way. The SEM charge effect observed in the green region (specifically the dark area) indicate electrical insulation between the top and bottom levels of the Nickel hard mask. While electrical insulation is not a requirement for a clean lift-off, and small imperfections like those shown in the red circles pose no issues whatsoever, this is a favorable sign of having a proper undercut profile on the soft mask, an essential characteristic for a successful lift-off process.

While the bilayer soft mask helped us to greatly improve the lift-off success rate for a 20nm-thick Nickel hard mask, the following step (i.e. etching the TiO_2 layer) proved to be the next main challenge. With the hard mask thickness of 20nm being close to the upper-limit of what the 2^{nd} generation process could provide (for a ∼50nm critical dimension), and too close to the lower-limit necessary to withstand the TiO_2 CCP-RIE etching, it became evident that a new approach was necessary. This motivated the evolution towards our 3^{rd} generation process that skipped the lift-off step altogether and allowed us to test thicker metallic hard masks, and ultimately led to our Fourth generation process, Direct soft mask etching described on Section 3.5. In spite of these changes, the much improved results obtained with the bilayer-based lift-offs for 20nm nickel masks were later found to be compatible with the ICP RIE chemistry of our 4^{th} Gen. process.

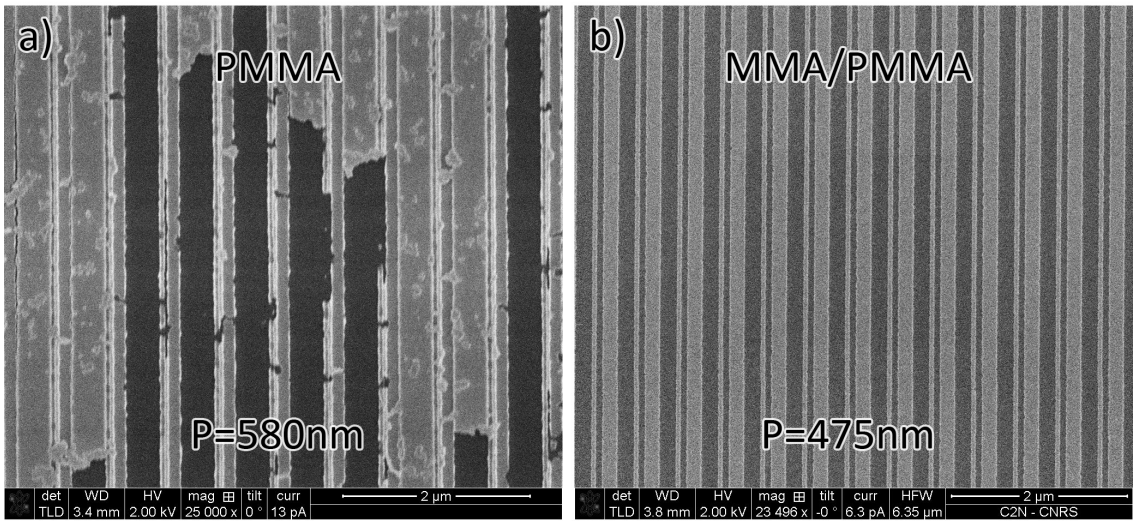

Figure 3.10 – SEM images of a pair of similar 1D metasurface nickel hard masks created through a lift-off process over a single resist PMMA soft mask (**a**) and a bilayer MMA/PMMA soft mask (**b**). The more sensitive underlying MMA layer helps to force an undercut profile as that of Figure 3.5 and drastically improves the nickel segmentation and subsequent lift-off.

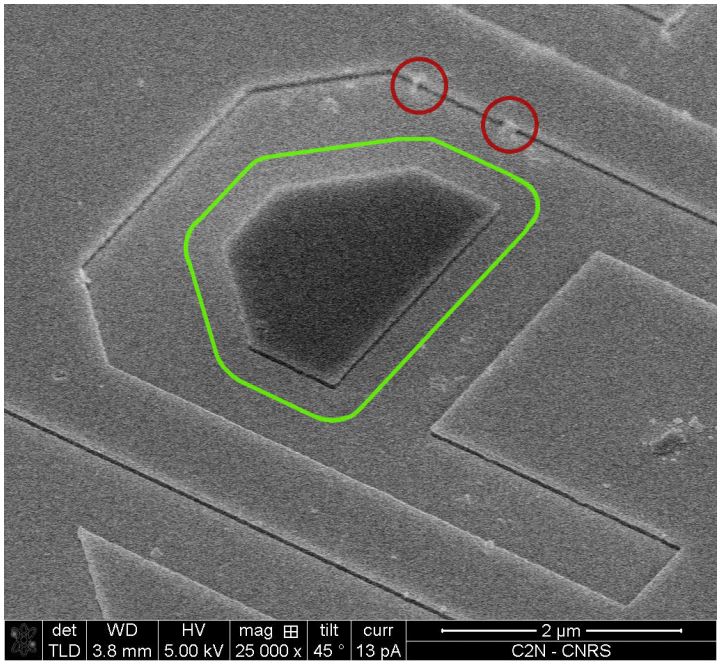

Figure 3.11 – Example of the appearance under the SEM microscope of a properly segmented metallic layer (Nickel) in preparation for lift-off. The Difference in tonality seen on the middle section of the **A** character marked in green comes from an electric charge effect, due to its electrical isolation between that section and its surroundings, evidence of mechanical separation of the two metallic levels, which ultimately translates into a successful lift-off. This example was achieved using a bilayer soft mask (2^{nm} Gen. Process in Section 3.3), developed precisely to tackle the lift-off issues found a single resist process at the scale of our metasurfaces.

3.6.5 Lift-Off technique

Patterning processes that include a lift-off step exists since at least 1980 and being such an old technique, we find a very large number of subtle variations of the technique, even with the same chemical elements involved. Every experienced user seems to have their own particular way to do it successfully and considering it is very often a completely manual procedure, there is plenty of room for voluntary and involuntary disparities that in some cases lead to radically different results, e.g. hand movements, sample transfer between containers, position of the sample in the solvent, sonication type and strength, etc. During this project, we went through different sources starting with our own in-house experience[51] on how to obtain the best possible results of this rather difficult step, particularly for the size of the patterns we were trying to transfer into the metallic hard mask. Ultimately, we converged to the lift-off technique described in Appendix .1, with one example of the result shown in Figure 3.10 (**b**). This technique was exclusively used with the Second generation process (Bilayer soft mask on Section 3.3) that despite being later replaced with the Third and Fourth generation processes (Etched Aluminum hard mask on Section 3.4 and Direct soft mask etching on Section 3.5) it was still of great value for hybrid processes (i.e. Bilayer Lift-off and ICP Chlorine etching).

3.6.6 TiO_2 Etching

In addition to gain more design flexibility, one of the main advantages of updating the MS design from continuous lines (1D MS) in favor of segmented lines and other bidimensional structures (2D MS's) was to minimize as much as possible the ARDE effect and thus gain more control over the fabrication results. By homogenizing the plasma exposure of the different etched areas we observed a significant reduction of this undesired effect, to a mere 5% instead of 30+%. Figure 3.12 shows this improvement on one of our samples (Third generation fabrication process) that included both 1D (**a**) and 2D (**b**) metasurfaces in it, all etched simultaneously with the same exact plasma conditions. On the 1D pattern, we observe a major depth difference between the narrow and wide sections of the design, not only detrimental to the performance of the metasurface but also with a highly irregular shape that we cannot accurately predict. By segmenting the 1D design into 2D structures we obtain a much more even depth profile along the cross section (shown in red on top of the layout **b**).

Figure 3.12 (**a**) and (**b**) also show the limitation of the Third generation fabrication process. Although aluminium was expected to offer the required etch resistance in a fluorine-based CCP RIE etching due to the formation of nonvolatile AlF_x species[94], we observed that its selectivity in combination with our structure's sizes resulted in the hard mask being etched from the sides, changing its nominal width, before the TiO_2 is fully etched. Even if the plasma recipe could result in a relatively vertical profile (green slope in Fig. 3.13) thanks to the TiO_2 sidewall passivation[9], half way into the etching the slope is greatly reduced as aluminium mask is eroded laterally by the plasma (red slope in the same figure).

The solution for both the ARDE effect and TiO_2 etching profile ultimately consisted on discarding aluminium (insufficient selectivity on CCP RIE etching) or nickel (prob-

[9]Likely due to the deposition of either CF_x or AlF_x species.

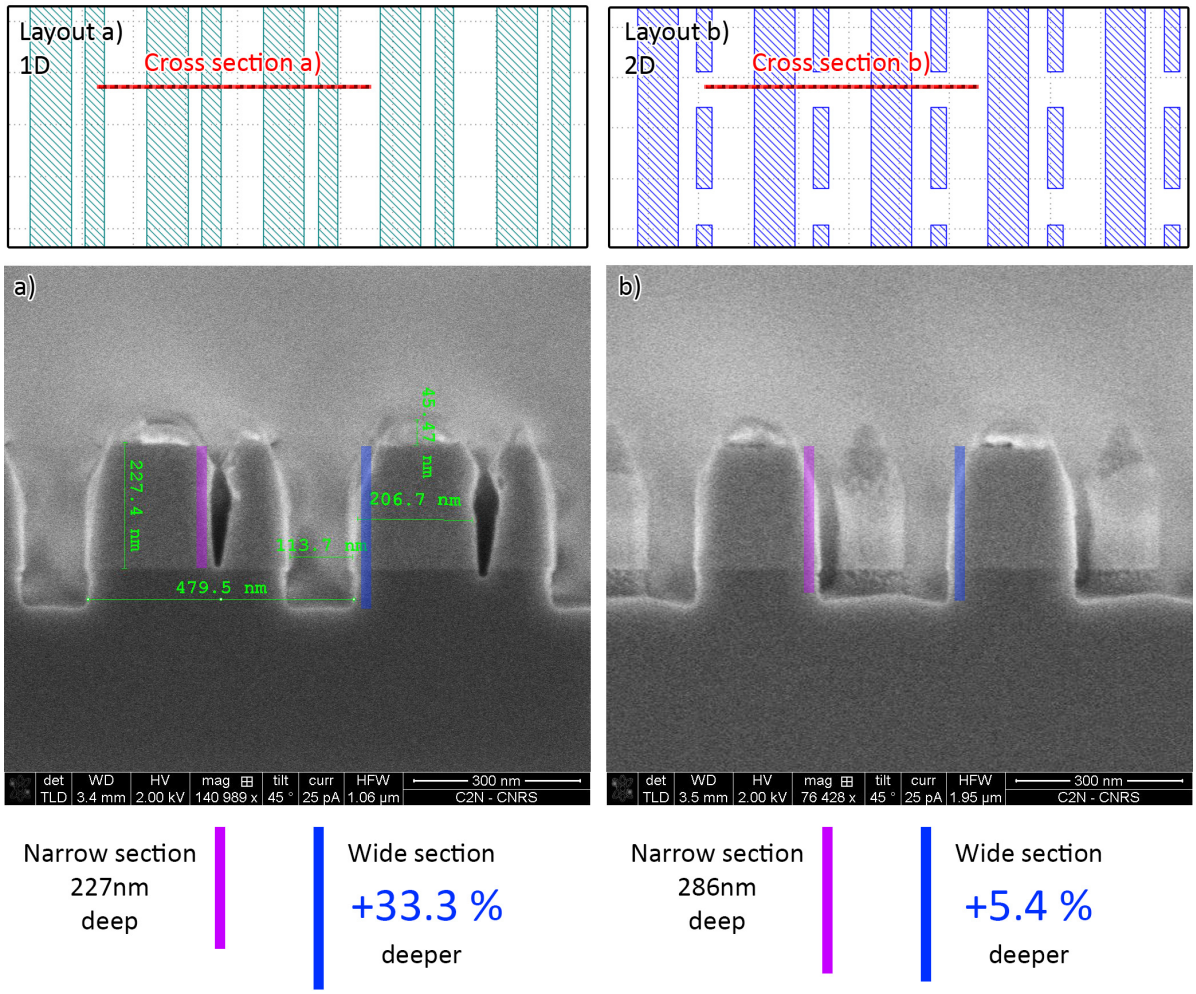

Figure 3.12 – The Aspect ratio dependent etching (ARDE) is an effect by which bigger features of the etched pattern are etched at faster rates than smaller features, creating deeper wide openings and shallower narrow one. We found this effect to be quite severe on our first 1D MS designs(a) tested on a Si substrate in comparison to our newer 2D MS designs (b) that were, among other things, addressing specifically this issue. The violet segments lengths match the observed depth at the narrow sections, with the wide sections matched by green segments.

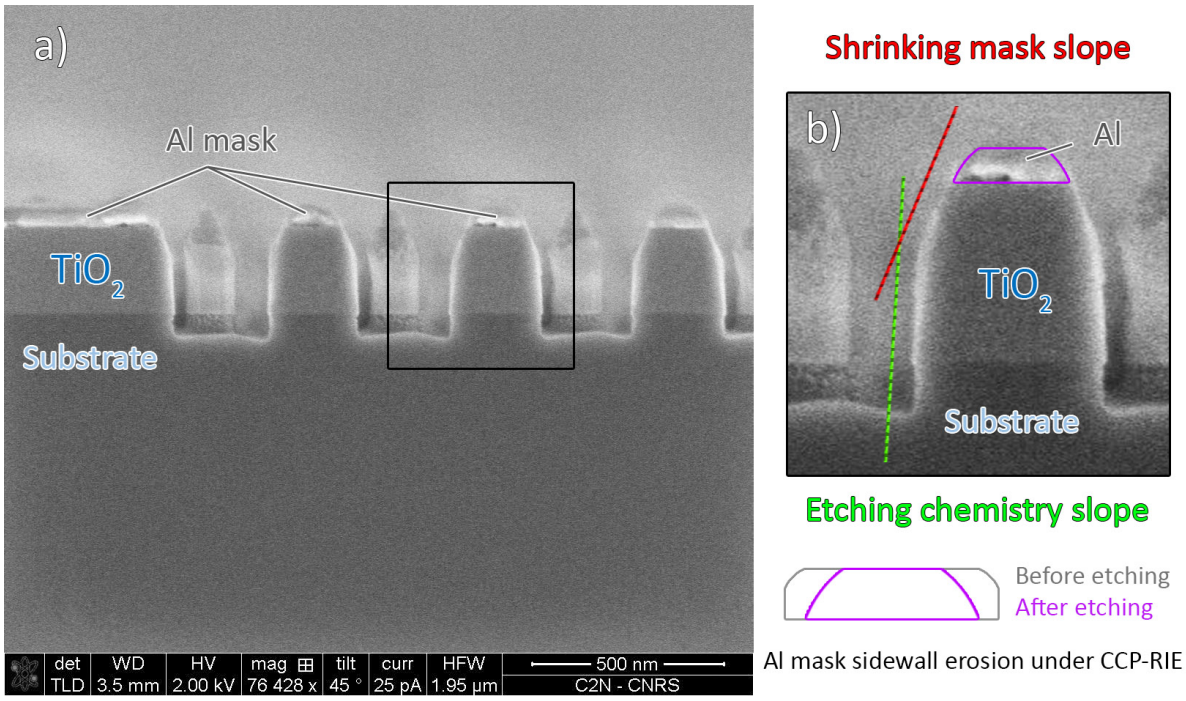

Figure 3.13 – SEM side view of a 2D MS test fabricated using the third generation process, based on ZEP resist and an aluminium hard-mask. Although ZEP was highly effective to create an accurate hard mask, the selectivity of the aluminium for Fluorine-based CCP RIE etching is not enough even with a relatively thick 80nm layer (4 times the thickness of the nickel layer in the 1^{st} and 2^{nd} Gen. process). This can be seen on the dual slope profile of the structures, with the dotted green slope due to the etching recipe and etched material, and the dotted red slope due to yielding aluminum mask. This incompatibility was solved developing a new fabrication process based on ZEP and more importantly, ICP Chlorine-based etching. The outcome of that 4^{th} Gen. process can be seen on Figure 3.14.

lematic lift-off and insufficient selectivity on CCP RIE) as hard mask materials and focus on a completely different TiO_2 process for 2D metasurfaces, replacing the SF6/CHF3 CCP etching for a HBr/BCl_3 chemistry on an TPSA-ICP RIE reactor (Section 3.5).

We found that this process (4^{th} Gen. Section 3.5) provides a high selectivity even using a soft mask (ZEP-520A resist), resulting in a more direct approach than using metallic hard masks (Ni and Al) as in previous processes. Its etching profile was also improved, with significantly more vertical walls than all previous processes, as is visible on the 2D MS on Figure 3.14 . In addition to this, on our test we also observe high selectivity with nickel, making a thin and easy-to-lift-off nickel hard mask also compatible and potentially advantageous for deeper etchings, although no further characterization was made due to clean-room time constrains.

In addition to the improvements in the MS quality, the advantages of a simpler process are hard to underestimate and they manifested not only in the final metasurfaces fabricated with it but during its development as well, with faster tests and fewer failed samples.

3.6.7 Future improvements

Short term

One unpredictable challenge was found with large-surface fabrications, with 'large' referring to samples that extend beyond the size of a single EBL main field size (500µm on our case with the Raith EBPG-5000) is that the physical displacement of the sample holder to a new field position, often caused variations on the field's result. Figure 3.15 is a good example of this, seen under an optical microscope with a large 4mm-wide metasurfaces fabricated for testing purposes. What should be an even surface of identical structures is clearly segmented on different sections with different exposures. Even if this type of anomalies is more rare on our typical 600µm MS fabricated with only 4 EBL fields (i.e. 4 mechanical movements), we have currently no control over these defects.

Another effect that we observed and had to take into account before measuring the size of the metasurface's elements is a reduction of the effective dose at any point closer to 15µm to the edge of the metasurface, most often squared and 600µm in size. We can relate this effect to the spatial distribution of energy density deposited in the resist by the electron beam due to the scattering of electrons on the resist and more precisely, the backscattering of electrons on the substrate[95], which makes this effect relatively independent of the resist employed[10]. In Figure 3.16, a SEM image near the edge of a 600µm metasurface shows, this inequality can be clearly seen. Each point in the MS design will receive an additional dose proportional to the amount of exposed surface on its surroundings, and hence all the points near the edge could receive as little as 50% of the secondary electrons received by the points 'inside' the MS (i.e. further than 15µm from the edge), reducing their effective dose on those places and altering the size of the structures. This effect can be taken into account when processing the vector files if need, and BEAMER (lithography software by GenISys GmbH) includes algorithms to

[10]If for a given resist, if its polymerization was highly nonlinear with the beam's intensity this effect could be reduced.

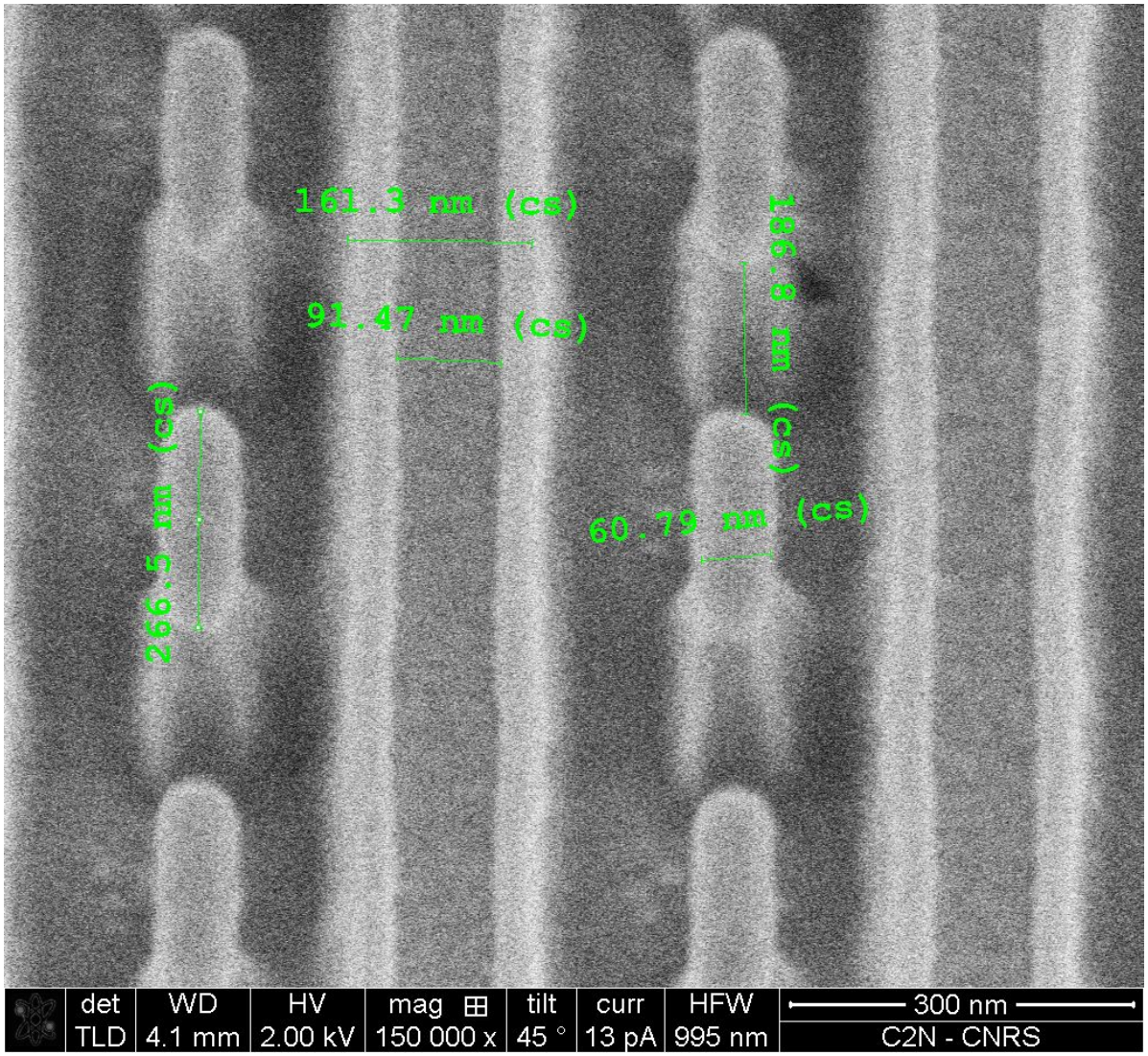

Figure 3.14 – TiO_2 etching profile and edge quality of a 2D MS fabricated with our latest 4^{th} generation process, based on a HBr/BCl_3 ICP RIE etching directly after the ZEP-520A resist soft mask is developed, avoiding the creating of a hard mask altogether. This process not only provided the best fabrication results compared to all the previous techniques tested but it is also a shorter fabrication with fewer potential failure points.

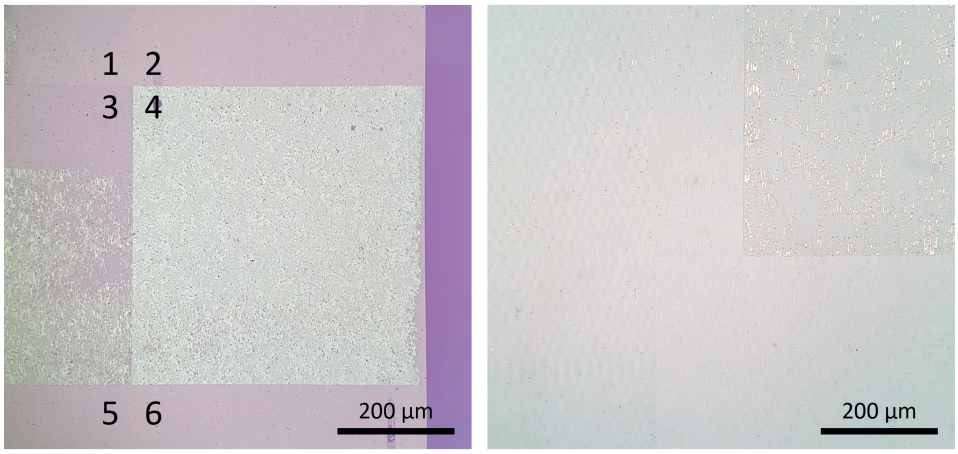

Figure 3.15 – Left: On this unusually large 4mm wide MS composed of 64 500µm EBL fields we distinguish 6 fields on what should be an even continuous surface. Right: Similarly to the left case, we observe individual fields indicating an different exposure or focusing of the electron beam.

compensate for these effects. Although this kind of software-based corrections were not used during the project, We expect future versions of the metasurfaces to include such corrections, even if under normal use the amount of light reaching the very edge of the MS is minimal.

More related to the pattern itself, when fabricating 1D metasurfaces, we observed a tendency to have an uneven response of the width of each line to the dose, with wider lines coming out with the correct size for larger doses than those needed for thinner lines, typically around 1/3 of the width of the former as shown in the example in Figure 3.17. This can be attributed to an underestimation of the e-beam's PSF size that is subtracted from the pattern's edge to accommodate for its own size when scanning such pattern. An underestimation of this PSF size could result on a few extra nanometers on every edge of the design, effect that becomes increasingly more significant the smaller the structure is. If the exposure is slightly underdosed, the combined result is smaller features being larger than nominal and larger feature being smaller than nominal. To correct for this effect, we need to adjust the e-beam effective PSF's size estimation for this particular type of sample and substrate, although in the context of this project this corresponds to a second order correction.

Long term

While our 4^{th} generation process allowed us to fabricate more than 10 successful samples, homogeneous across more than $10mm^2$ and with smooth vertical walls, the TiO_2 ICP RIE etching employed has not been fully optimized for our samples. As long term improvements we see necessary a systematic characterization and optimization of the HBr/BCl_3 ICP chemistry for TiO_2, specifically adjusted to the type of structures we have designed so far. There is also the need to properly characterize and improve the selectivity for the two mask materials used, namely a ZEP-520A soft mask and a nickel hard mask (generated by the bilayer soft mask process of Section 3.3).

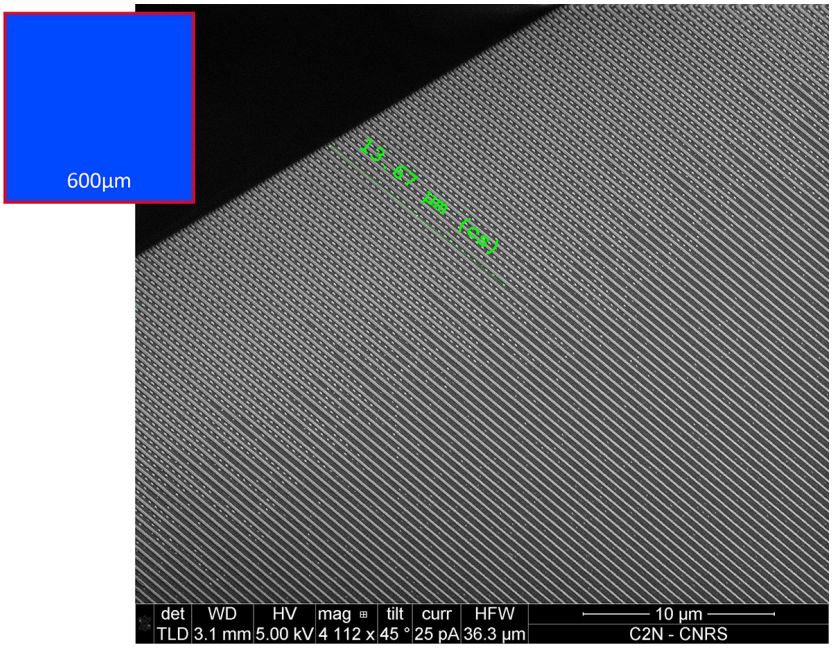

Figure 3.16 – The effect of EBL secondary electrons can be clearly seen on the surrounding 15µm of this 600µm square 2D MS. Inset shows at scale the region with an homogeneous effective dose in blue, and the affected section in red around the edges. Being the 9% of the MS surface that receives the less amount of incident light, no corrections were put in place up to this point, but it can be easily adjusted with available software tools.

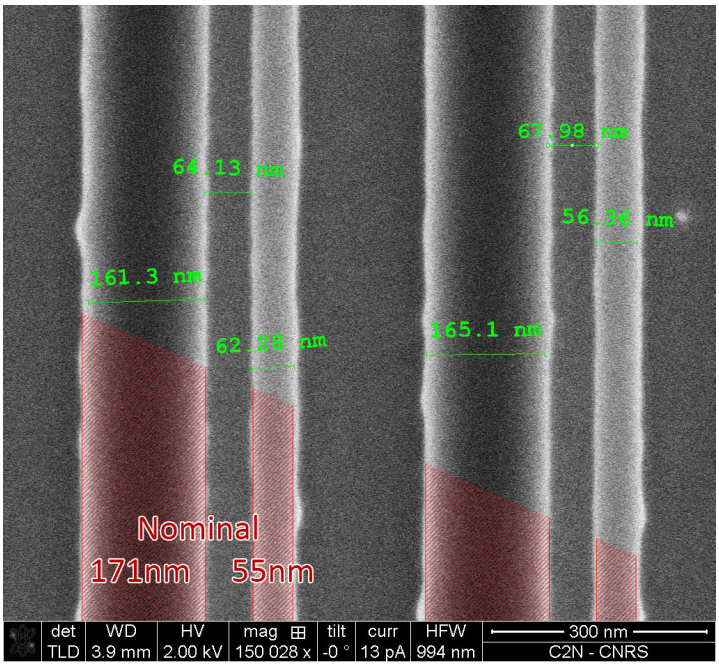

Figure 3.17 – Overlap between a SEM image of a 1D metasurface aluminium hard-mask and its vector file design. Fabricated with a ZEP soft-mask and a 165µC/cm^2 dose, we observe the narrow lines are too large (62nm instead of 55nm) and the wide lines are too thin (163nm instead of 171nm). We suspect this corresponds to an underestimation of the e-beam PSF size when processing the files.

In a secondary instance, studying fluorine-based chemistries but on our ICP-RIE system, such as a pseudo-Bosch C_4F_8/SF_6 process, could potentially lead to an even higher selectivity, due to the lower ion energy and stronger passivation effects (CF_X). Lastly, we think there is a possible revalorization of the 3^{rd} generation 'lift-off-less' process if we find a more etching resistant metal, with chromium being the suggested first candidate.

Chapter 4

Characterization

The characterization of the optical response of the metasurfaces was fundamental to validate the fabrication process. The optical test carried out consisted in the following main tasks:

1. Obtaining the angle of the transmission diffraction orders for the wavelength at which the MS design was optimized.
2. Measuring the direct transmission (0^{th} order) of the metasurface at that wavelength.
3. Obtaining the efficiency of each transmission diffraction and the resulting figure of merit for which the MS design was optimized.
4. A validation of the metasurfaces as a light coupling device using a standard microscopy slide.
5. A proof of concept of the technique as a whole, resulting in a TIRF image of a biological sample.

The next two sections are aimed to present the preparation and execution of these individual measurements and experiments, divided into two main groups.

4.1 Passive experiments

We describe as "Passive" a series of experiments that do not include any fluorescent substance nor rely on the observation of an external element beyond our own metasurfaces. They are designed to give us a better understanding of the performance achieved with our designs and fabrication processes. These experiments are going to be followed by those in Section 4.2 that are aimed specifically to perform MS-TIRF microscopy on an external fluorescent sample.

Our first task was to measure the light intensity on each of the diffraction orders being transmitted by the metasurface. For small angles such task would be almost trivial, as any order being diffracted less than ∼42 degrees would be able to escape the

glass substrate and be measured with a simple optical power meter. In our case, we are precisely designing these metasurfaces not to do that, working with high diffraction angles that cannot escape the substrate. For that purpose, three experiments were employed, described in the following subsections and summarized as:

1. **Diffraction angle**. First and foremost the diffraction angle for the +1 and -1 diffraction orders, on which the entire device relies on, had to match the angle expected by the design. This was done in a direct way by coupling the MS to a large glass block and visually measuring the angle and also later verified by imaging the diffraction orders on the back focal plane of a TIRF objective and correlating their positions to their angles.

2. **Direct transmission**. The efficiency of 0th order, which is the transmitted light whose direction is unaffected by the metasurface, is a quick way to identify our best samples since its measurement is significantly simpler than that of the high-angled first orders.

3. **Order efficiencies and figures of merit**. Using a high-NA TIRF objective as described on section 4.1.3 we capture all 3 diffraction orders, measure their efficiencies η and calculate the relevant figures of merit.

Due to the large number of samples and metasurfaces on each sample as well as the chronological evolution of the experimental tests performed and MS fabrication, not every validation was performed on every single MS, but instead they served as a tool and guide for the continuous improvement of individual aspects of the MS design and fabrication, by testing those specific samples that could better help us to understand their overall performance as a TIRF microscopy device.

4.1.1 Diffraction angle

Seeking an initial validation for the fabricated metasurfaces, the first experiment devised to measure the diffraction angle was performed with the simple method of bridging the glass coverslip and a glass semicircular prism with index-matching oil. This configuration allows the diffracted beams to propagate beyond the thickness of the coverslip, more than 45mm, enough to visualize and measure in a direct way the angle between the incident input point, and the two exit points of the 0^{th} and 1^{st} orders, as shown in Figure 4.1. This confirmed us the diffraction angles obtained were systematically under one percent point of the design values (typically close to 0.5%), and well within the range that suffices the intended purpose of obtaining total internal reflection in a glass-water interface. This minimal error correlates with the high metasurface period accuracy achieved on the fabrication, making the diffraction angles the characteristic most resilient to process imperfections. Considering the periods were measured to be within 0.2nm of their nominal values (measured multiple times over multiple periods), the absolute error on the first diffraction order angle (Equation 2.2) can be estimated as:

$$\Delta\alpha_1 = \frac{\partial(\arcsin(\frac{c}{p}))}{\partial p}\Delta p = -\frac{c}{p^2\sqrt{1-\frac{c^2}{p^2}}}\Delta p\Big|_{p=465nm,\Delta p=\pm 0.2nm} \sim \pm 0.05^\circ \tag{4.1}$$

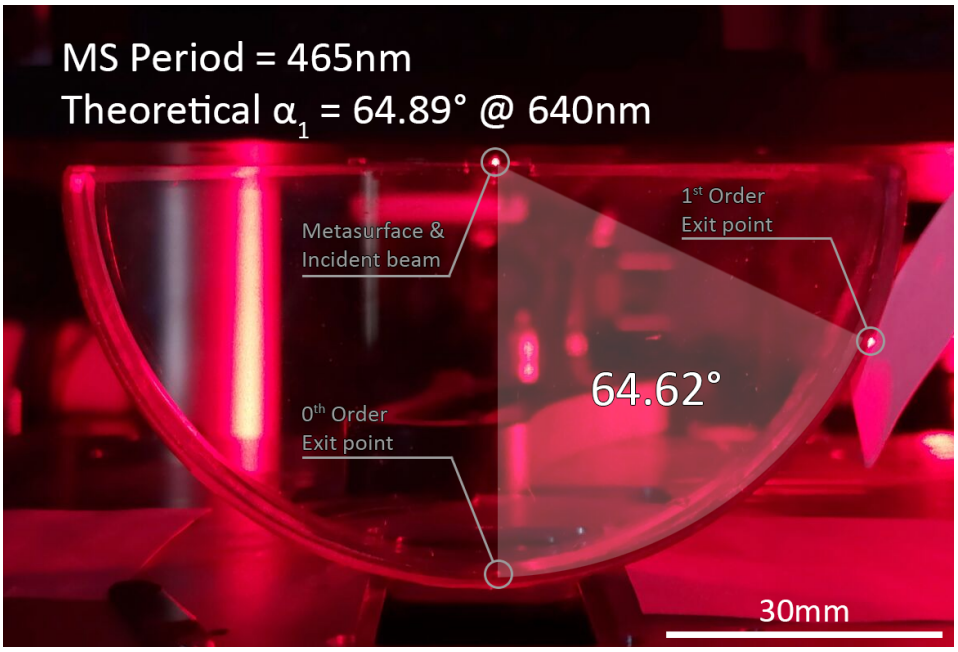

Figure 4.1 – Photograph of a metasurface on a glass coverslip stuck to a semicircular prism with index-matching microscopy oil. The point where the incoming beam hits the MS, and the exit points for the 0th and 1st order can be clearly distinguish, as well as the angle between them. This sample was fabricated with the Fourth generation process (Direct ZEP, Section 3.5).

for $c = 640nm/1.52$. This is below the error obtained on 4.1 which is likely to respond to the inherent errors introduced by a photographic measurement (e.g. due to optical distortions, pixel sampling, etc.). Even with these considerations, we repeatedly[1] obtained negligible relative errors on the diffracted angles. It is important to remark that the horizontal shape and vertical profile of the structures have no effect on the diffraction angles, as it is expected.

4.1.2 Direct transmission

The direct transmission or zero order refers to the light that is not diffracted by the metasurface and traverses the device without being diffracted by it. Depending on the device configuration (i.e. the position of the metasurface with respect to the biological sample on the substrate, see Section 5.4) this order may potentially have a detrimental effect on the image contrast and as such it was designed to be greatly minimized on all the designed metasurfaces. How effectively this order was minimized depended in great measure on the overall quality of the fabrication, and by illuminating the entire sample with a TE-polarized 675nm beam and measuring the light attenuation on each metasurface we could obtain a quick reference of which metasurfaces were performing their best, or more precisely which ones were certainly under-performing. For some early fabrication tests we made arrays of metasurfaces scaling up and down its feature sizes and general scale to adjust for possible size-shifts due to the e-beam exposure or resist developing time.

[1] Using photographs obtained with different cameras.

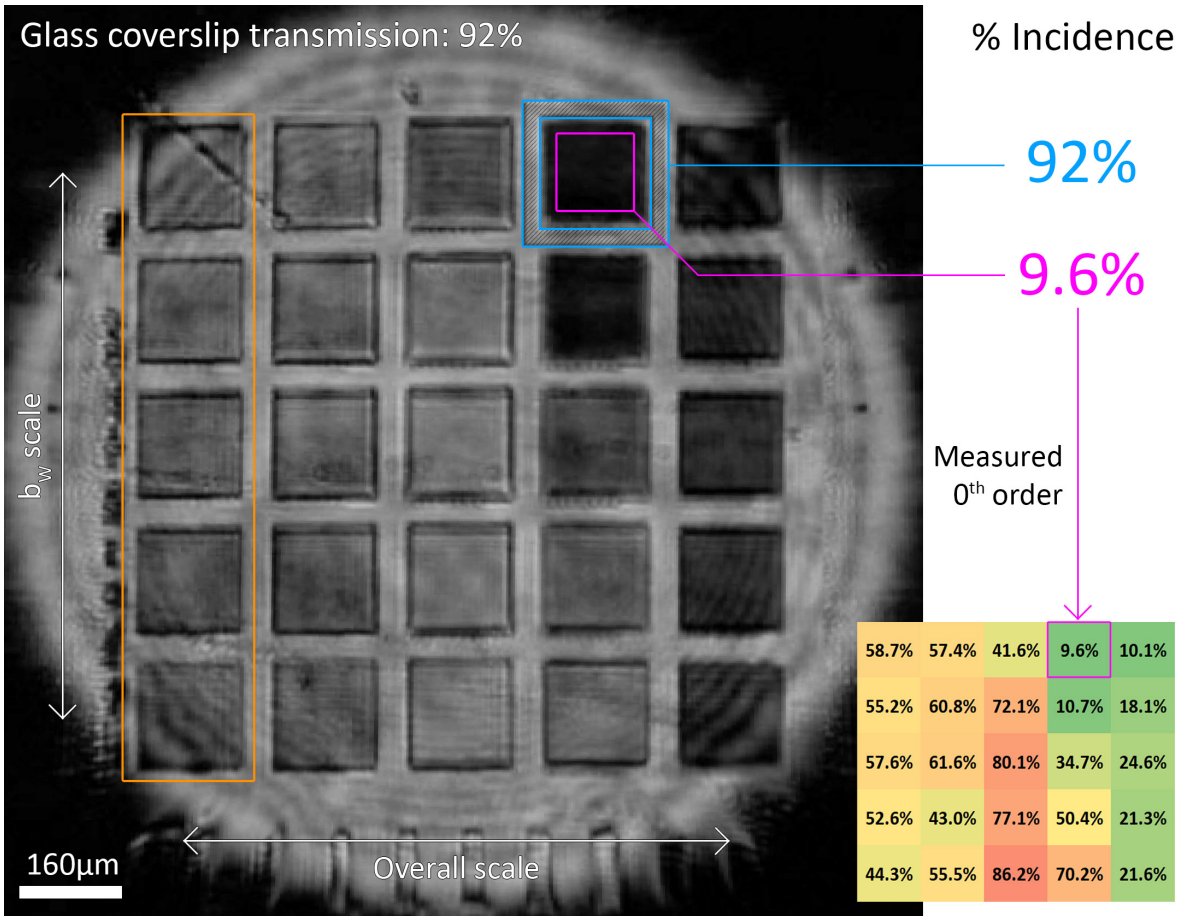

Figure 4.2 – Optical image of an array of 5x5 160µm-large one-dimensional metasurfaces being back-illuminated with a TE-polarized 675nm beam. This configuration allows for a very simple and fast reference of the direct transmission suppression, a desired characteristic of the device. The transmission efficiency of each individual MS is shown in the color diagram, from 0% in green to 100% in red. The inhomogeneity of the illumination plays no significant role since the transmission of each MS (marked in pink) is compared to its neighbours pixels (marked in blue), averaging ∼20K pixels both in and around the MS. Each column changes ±10% the scale of all the parameters (a_W, b_W, b_X and p) from the center column, and each row changes an additional ±10% on a_W, the widest line of the two. In the first column of metasurfaces (in orange) the thinnest line should have been 48nm wide, but it was not successfully fabricated, becoming effectively a regular diffraction grating (see MS1 and MS20 images on Figure 4.3).

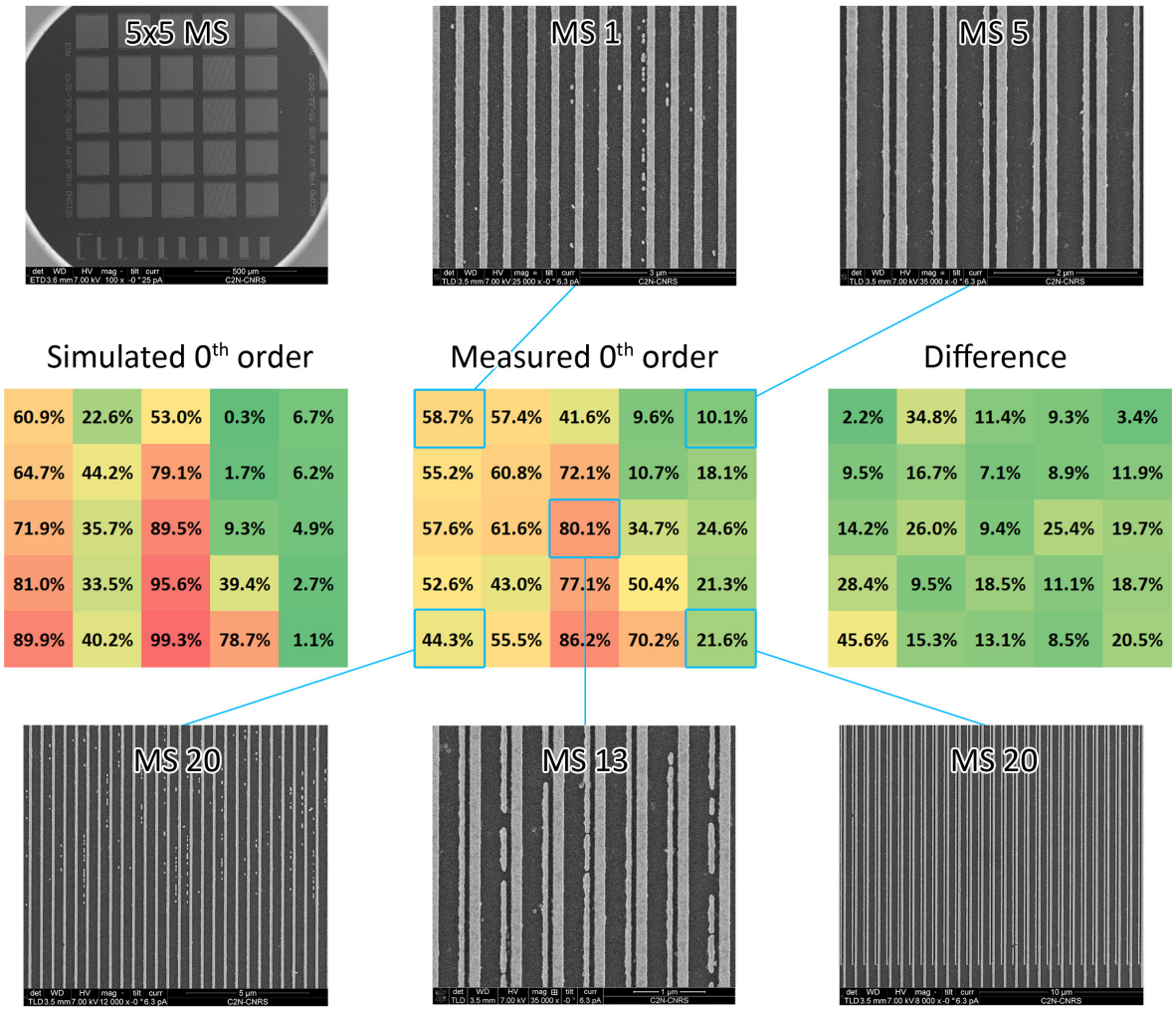

Figure 4.3 – Measured 0^{th} order transmission relative efficiency for the 5x5 array of 160µm-large metasurfaces shown in (a) in contrast to the simulated values for the same MS array and their difference (relative to maximum possible transmission of 92% of incident light). As expected, the MS overall performance deteriorates when the fabrication technology cannot keep up with the increasingly smaller sizes on the bottom-left of the MS array.

Figure 4.2 shows one of such arrays with 25 one-dimensional 160µm-large metasurfaces. This particular sample has each column scaling all parameters (a_W, b_W, b_X and p) on steps of 10% and each row additionally scaling only a_W on 10% steps resulting in 25 slightly different metasurfaces, an early-stage strategy to compensate for systematic fabrication inaccuracies. Under SEM inspection, we observed that the smallest features on those bottom-left metasurfaces were not successfully fabricated, while much better results were obtained for the top-right cases. Accordingly, the measured 0^{th} order transmission visible on Figure 4.3 is lower and better matches the simulated values on the latter (top-right corner), followed by a weaker correspondence towards the bottom left of the array. On the left column of the array, the thinnest line of the grating is so narrow ($b_W = 48nm$) that it is completely lost during the fabrication, effectively creating a regular diffraction grating.

To better analyze the response of the first column, in Figure 4.4 we compared our transmission measurements against a simulation better matching the result of the fab-

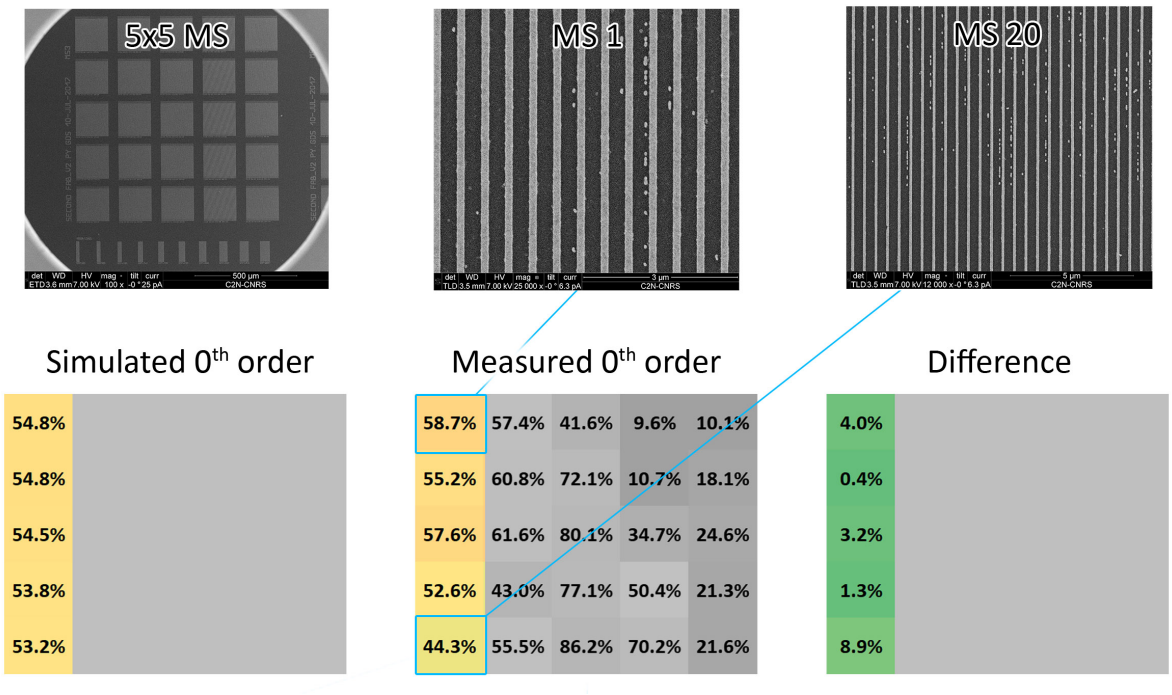

Figure 4.4 – An analysis equivalent to that of Figure 4.3 for the first column requires simulating a standard diffraction grating, due the missing 48nm line of the metasurfaces of that column. This reduces the mismatch between the simulations and the measurements visible for that column on Figure 4.3.

rication for that column, i.e. a standard diffraction grating. This adjustment improved the accuracy of the simulation for that section and closed significantly the gap between the simulations and measurements, to single digit numbers.

From this particular sample (Figure 4.2, 4.3 and 4.4) we can also observe that while both simulated and fabricated standard gratings transmit over 50% of the incoming light, using asymmetric metasurfaces the direct transmission is being reduced a factor of 6 to only 9.6% on this particular sample. With our latest design and fabrication process, this is further reduced to a transmission of only 6%, as we see on the following subsection (4.1.3 Fig. 4.8). We conclude that our asymmetric metasurfaces vastly outperform a standard grating in terms of 0^{th} order suppression.

4.1.3 Order efficiencies and figure of merit (FoM)

Due to the high diffraction angles transmitted by the metasurfaces, and with the sole purpose of studying our fabricated samples, we used a high-NA TIRF objective and oil to 'bridge' the air gap between the MS-TIRF substrate and the objective, and hence be able to capture the diffracted first orders even with angles as high as 78°, that would be totally reflected inside the glass substrate under normal use without oil (i.e. when imaging with an air or water objective).

The complete setup was based on a X-Y motorized stage with a metasurface holder, an Olympus UApo N 100X 1.49 oil objective mounted on both a motorized Z stage and a piezo Z-stage (PIFOC, Physik Instrumente GmbH) allowing for fine and course

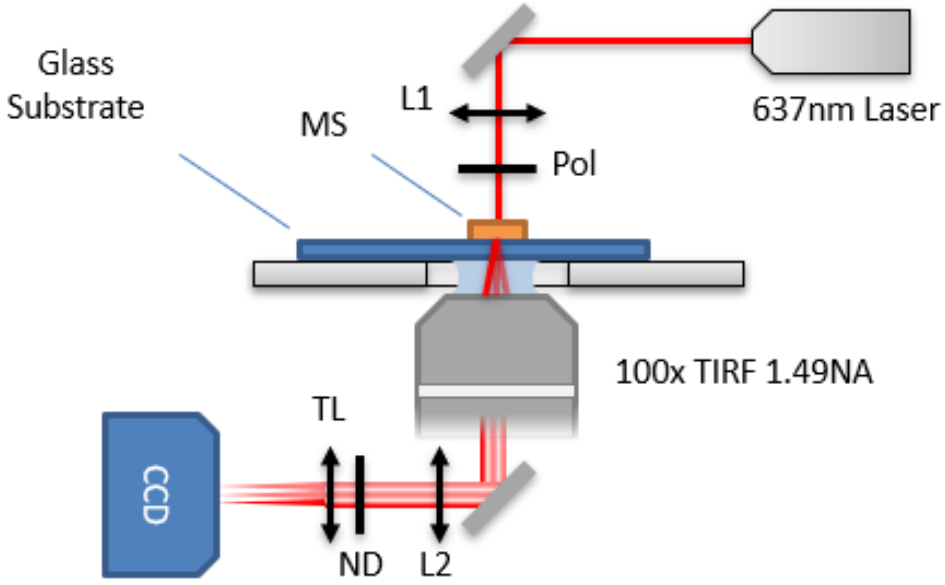

Figure 4.5 – Experimental setup for the measurement of the metasurface's diffraction order efficiencies for a monochromatic 637nm source. The beam is weakly focused with L1=300mm, linearly polarized for a TE only incidence and reaches the MS on the glass substrate with an approximated waist size of 250µm. All transmitted diffracted orders are captured thanks to a 1.49 NA Oil Objective and refocused in the objective's BFP near its exit pupil. A pair of lenses labeled TL and L2 image this plan on the camera's sensor plane. A neutral density filter is placed to avoid pixel saturation.

movements, a Coherent OBIS 637nm continuous wave diode laser system (140 mW) and a camera ANDOR iXon Ultra DU-897U-CS0-#BV with a 512x512 pixel sensor (16µm pixel size). The laser was filtered with a ZET 640/10 Laser Clean-up Filter, TE polarized with a Thorlabs CM1-PBS251 Polarizing Beamsplitter Cube and finally slightly focused with a Thorlabs AC254-300-A-ML 300mm achromatic doublet. This experiment was mounted in the Third Institute of Physics - Biophysics laboratory of the Georg-August-Universität Göttin-gen in Göttingen, Germany, with a similar configuration mounted a second time at C2N CNRS in France.

The TIRF oil objective, in close proximity to the slide but opposite side to the MS captures the 3 beams coming from the MS's glass side with a low divergence (∼5mrad) and focuses them on its back focal plane (BFP) close to its exit pupil. The rest of the experimental setup consists on a pair of lenses (TL and L1 in Figure 4.5 and 4.6) to image this BFP on the camera's CCD, plus an additional variable ND filter to regulate the intensity and avoid saturating or damaging the sensor. The lenses L2=300mm and TL=180mm employed gave a magnification of 0.6.

Under the assumption that we are dealing with a Gaussian beam and small divergence angles, we can estimate the radius ω_0 at which the amplitude is $1/e$ of its value on the axis (at the metasurface) for an incident $D = 1mm$ wide beam through a $F = 300mm$ lens as

$$2\omega_0 = \left(\frac{4\lambda}{\pi}\right)\left(\frac{F}{D}\right) = \left(\frac{4 * 0.640\mu m}{\pi}\right)\left(\frac{300mm}{1mm}\right) \approx 240\mu m$$

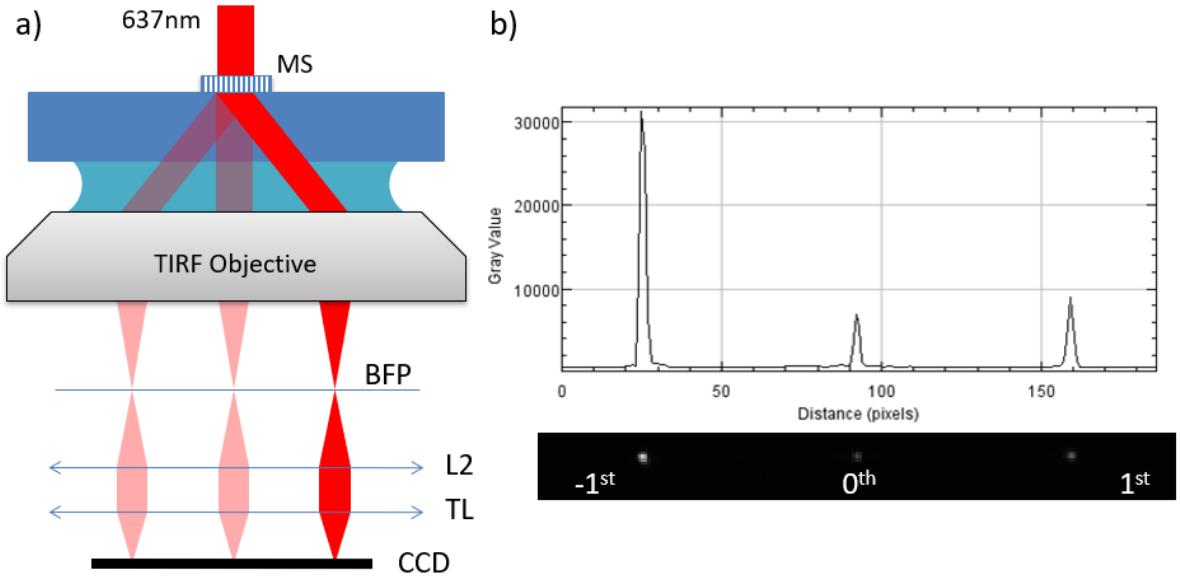

Figure 4.6 – a) Simplified schematic of the setup of Experiment 3 shown in Figure 4.5. b): Example of the BFP images obtained for one of our 2D MS designs optimized with the figure of merit R_3, with the highest intensity point on the image corresponding to the negative 1^{st} order.

which fits comfortably on the metasurface's size, typically a 600µm square. This condition is important because any light missing the metasurface and passing right around it, will also be collected by the objective and will contribute to the intensity of the 0th order focused on the BFP, altering the ratios between the orders that we intend to measure. On the opposite, if the beam waist at the MS is too small we would illuminate only a few individual periods, affecting the efficiency of the diffraction orders. When the beam on the MS is sufficiently large without exceeding the metasurface's size, we capture images like that of Figure 4.6 (example for the 2D MS shown in Figure 2.28**b**)

First order efficiencies and Figures of merit

Our measurements using the experimental setup described in Subsection 4.1.3 resulted in series of images showing the diffracted orders generated by the metasurfaces as well as others with direct transmission through a plain section of the glass substrate for normalization purposes. All of the fabricated MS samples had arrays of different e-beam doses resulting in many satisfactory MS along with overdoses or underdosed metasurfaces with degraded performance or even non-existant in some extreme cases.

Despite only a small fraction of the 40-50 fabricated samples are of the 1D double-groove type, and that those samples were fabricated with the very first process we have used in this project, we did measure some 1D metasurfaces with a high R_2 ratio up to 14.1, visible on Figure 4.7. This ratio is even higher than the expected value of 11.3, which most likely responds to the strong overetching observed on these early samples, the earliest strategy employed to try to fully etch the narrow grooves of the 1D design. While this may be desirable for this specific sample unit, it is very challenging to design metasurfaces and predict their performance taking into account a strong aspect ratio dependent etching, i.e. the effect that forces us to overetch the wide groove on 1D MS

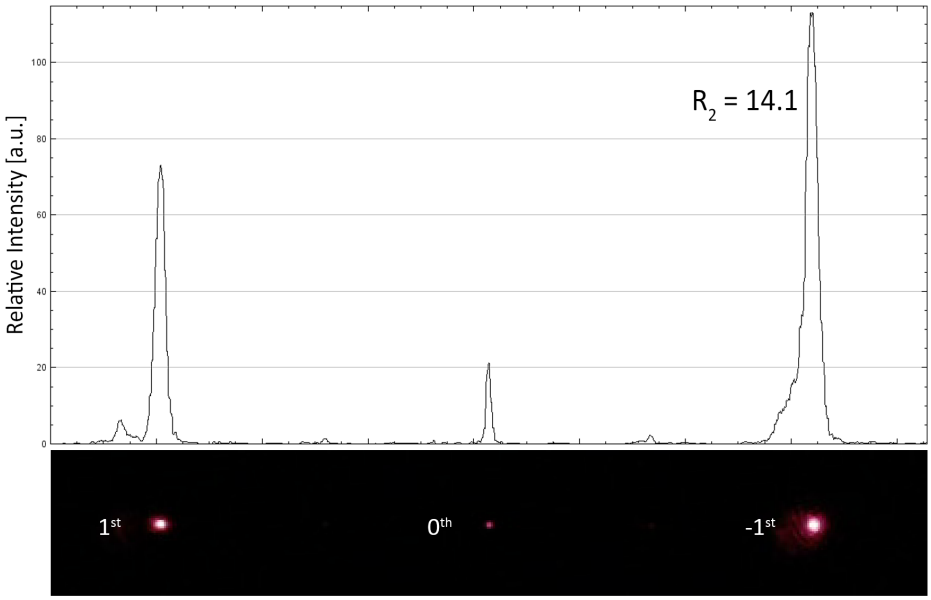

Figure 4.7 – The image of the diffraction orders of a 1D MS design show a relatively strong R_2 ratio of 14.1. The ratio is calculated with each point's integrated pixels value instead of their maximum value to be able to disregard the difference in size generated by the spherical aberration of optical system used.

designs.

Our 2D metasurfaces fabricated using the most recently developed ICP etching process (Chapter 3), with the designs visible in Figure 2.28 have successfully channeled up to 70% of the transmitted light into one of its first transmission orders. The back focal images obtained of both the light transmitted by the metasurfaces and a reference beam going through an empty section of the glass substrate allowed us to obtain all the relevant information. All the images captured had their mean background noise subtracted and the integrated pixel value of three sections around each point in the image (i.e. corresponding to the three transmitted diffraction orders shown in Figure 4.8) were normalized by the same type of measurement done with the reference beam, that was considered to be 95.7% of the incoming TE-polarized beam and was used to normalize the diffracted orders measurements. This percentage comes from the theoretical transmission of the air-glass interface considering a glass refractive index of 1.52 (borosilicate glass). Any other light loss occurring on the system will affect both the MS and reference measurements and as such have no impact on the order measurements. On those measurements where no spherical aberration is observed on the optical system, the pair of first order points on the image, and the center point corresponding to the direct transmission are of similar size, and then the ratio between their maximums closely resembles the ratio between their integrated value, which is not the case on some of the earliest measurements. In any case, by integrating the value of all the pixels around each point on the image, their precise size plays no role on the measured efficiency.

Figure 4.8 let us see an experimental ratio R_3 of 2.3 for this particular 2D MS design, with measured diffraction order efficiencies $\eta_{-1} = 0.43$, $\eta_1 = 0.13$ and $\eta_0 = 0.06$, not too distant to the simulated values for this 2D design of $\eta_{-1} = 0.55$, $\eta_1 = 0.16$ and $\eta_0 = 0.04$ and R_3=2.85. More importantly, we are obtaining a direct transmission 6

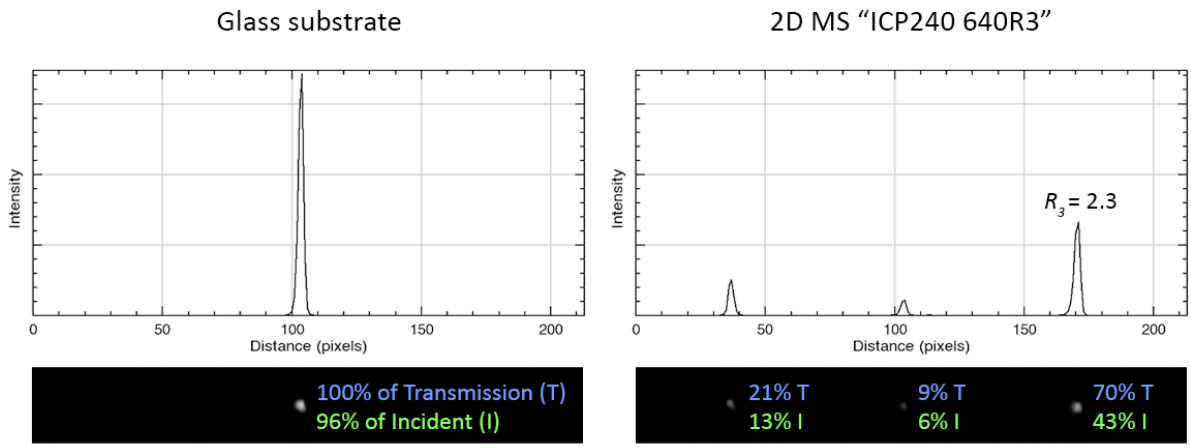

Figure 4.8 – Transmission order efficiencies measured for a 2D MS sample. With a resulting ratio R_3 of 2.34, it does not reach the theoretical value of 2.85 expected using a 640nm normal incident laser. The total transmission of 61.9% the incident light is also under the theoretical value of 74.9%. We think could be attributed to scattering looses due to the MS shape itself as well as possible surface contamination after the samples exit the clean room environment, or even small fragments of the metallic hard mask still adhered to the titanium dioxide.

times more suppressed than an equivalent 'standard' diffraction grating (simulated by removing the segmented structures breaking the grating's asymmetry), and 10 times more suppressed than our experimental measurements of similar gratings (see Figure 4.4). It is also worth noting that the fabrication process used for this 2D MS sample was barely optimized[2], and we expect these figures of merit, and overall performance, to increase as such process is further refined.

Incident polarization

By design these metasurfaces require TE-polarized incident light to effectively channel most of the light into one first order. We measured the effect on the order efficiencies of a linearly polarized incident beam that gradually rotated away from TE polarization (99.9%) by an angle γ, reaching a maximum of 90°, which corresponds to TM polarization.

The measured response visible on Figure 4.9 shows the relative efficiency of each of the 3 diffraction orders. Although we observe a higher than expected increase on the 0th order intensity as γ reaches 90°, the behavior of the two first orders and their crossover when switching from TE to TM-polarized light closely resembles the simulated curves, with both curves equalizing at γ=50 degrees both on the simulated and measured data. The central order increase well above the ±1 orders could be attributed to the sample fabrication itself, not being identical to that of the simulation, or to a possibly misalignment of the beam on the metasurface as the polarizing beamsplitter cube was rotated. For a TM incident beam the theoretical efficiency of the 0th order η_0 is just 0.26, whereas any light missing the MS area and passing through the glass coverslip substrate

[2]The lab's clean room facility was shut down in August 2018, shortly after the fabrication of this sample, and not yet fully operational in August 2019.

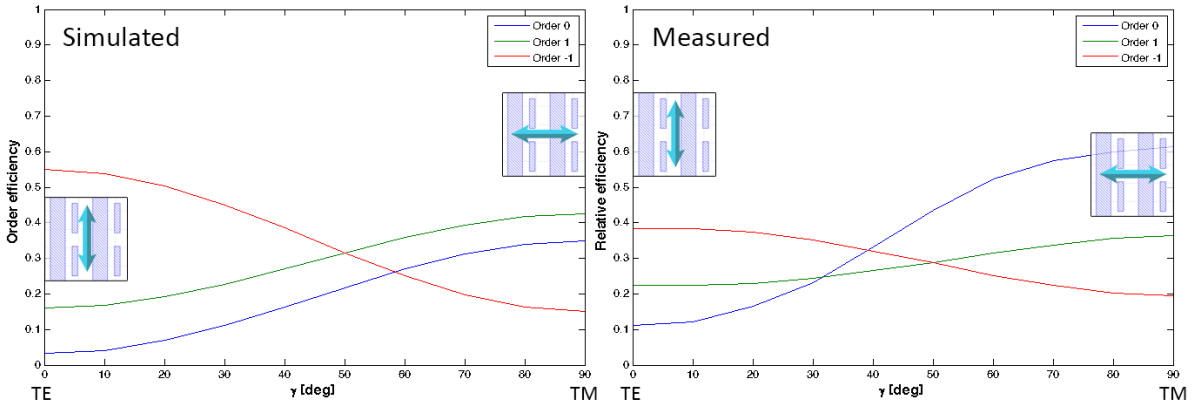

Figure 4.9 – Left: Simulated response of the diffraction order efficiencies transmitted through the metasurface to a variation in the incident polarization of γ with respect to the nominal TE incident polarization. Right: Measured relative efficiencies, with a 0th order that increases beyond its expected value for TM incident light, possibly due to a misalignment of the beam over the MS, leaking some of the light around it directly into the TIRF objective.

will have an efficiency of 0.96, rapidly contributing to the metasurface's η_0. This general agreement, in conjunction with the measured figures of merit and direct transmission (Subsection 4.1.2) contributed to build confidence on the structure's simulations.

Diffraction angles revisited

The diffraction angle for the ± 1 orders was measured again for a small selection of samples using an indirect technique that relies on the same images captured for the diffraction efficiency measurements.

Using the 1D MS array fabrication shown in Figure 4.10 that included multiple MS periods (with 5 different 1^{st} order angles), BFP images obtained the same way as for the FoM measurements (Subsection 4.1.3) were stacked in the single composite image shown in Figure 4.11, all around the central 0^{th} order (the rotation is only meant to avoid the dots overlapping with each other).

Finally, by manually shining light in all directions in close proximity to the coverslip surface with a LED torch, we can capture a final BFP calibration image of the largest radius corresponding to the highest angle that can be collected with the objective (corresponding to its NA). The last step uses a MATLAB script to detect this 'Max NA' circle, transform it on its corresponding incidence angle, and map all the angles captured by the objective into the radial direction of the composite image. With this method the resulting angles of the 1D MS array matched its theoretical values within a 4% error, most likely attributable to the low precision of the calibration image. By using TM-polarized light instead of the usual TE, we are sure to clearly see both 1^{st} orders instead of just one.

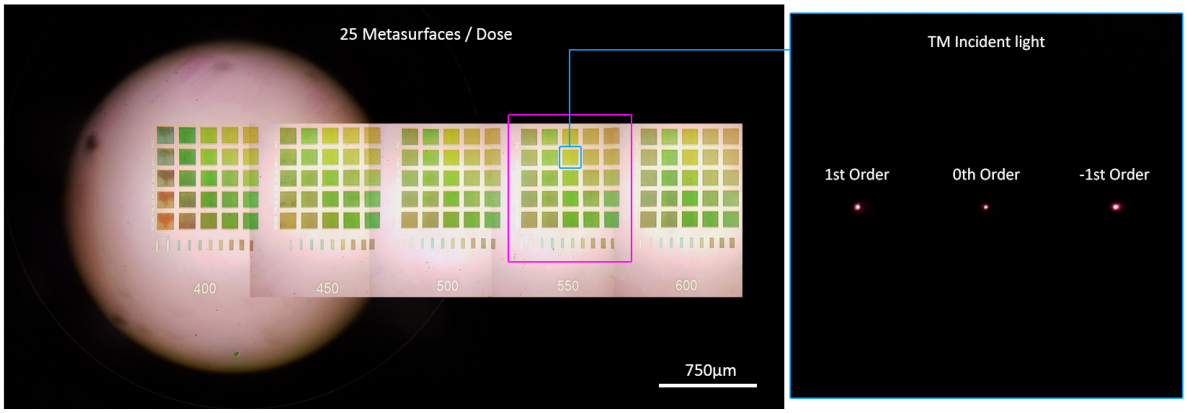

Figure 4.10 – Left:Optical composite image of a MS dose-test sample with 25 metasurfaces per dose, each column with a different grating period. Their theoretical diffraction angles are 39.6°, 44.1°, 50.0°, 58.3° and 73.1° with 675nm TM-polarized incident light to assure both first orders are visible and measurable. Right:Single frame out of the 25 back focal plane images of a NA=1.46 TIRF oil objective.

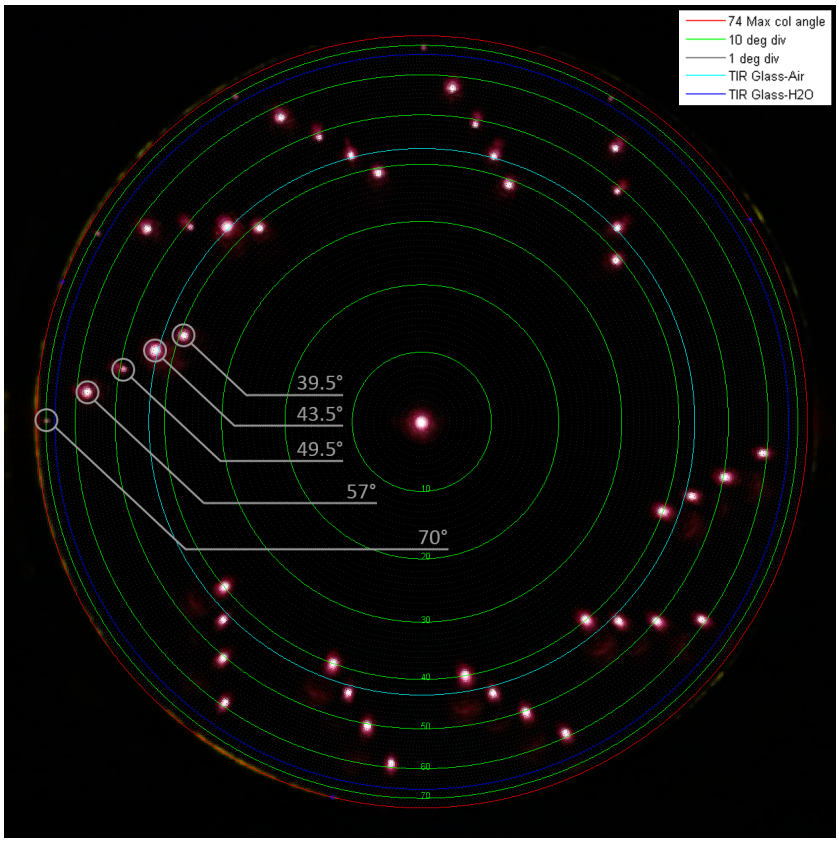

Figure 4.11 – Stack of 25 back focal plane images through a NA=1.46 TIRF objective capturing all 3 diffraction orders transmitted by 25 metasurfaces with 5 different periods (i.e. 5 different 1^{st} order angles). Using the largest radius visible on the BFP corresponding to the largest angle that can be captured by the objective, the individual angle of each MS diffraction order can be obtained with an error under 4%.

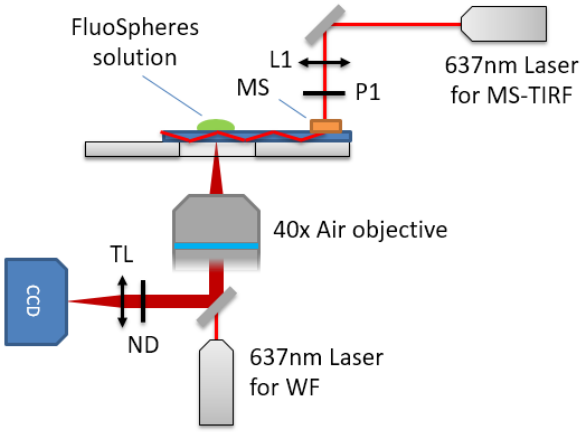

Figure 4.12 – The setup used allows to illuminate the sample independently and simultaneously with a TIR evanescence field or WF illumination using two 637nm CW lasers. An Olympus UPlanSApo 40X NA 0.95 air objective and an ANDOR iXon Ultra camera are used to image the fluorescent sample mounted on a custom motorized stage.

4.2 MS-TIRF Microscopy experiments

4.2.1 Setup

By measuring the order efficiencies η_n for each individual metasurface, generally fabricated in groups of 10 to 40 per substrate, we could identify those MS with the best performance, i.e. coupling the maximum amount of light into the coverslip in the right direction, and use them to empirically verify our ability to selectively excite molecules on the surface.

For this purpose we modified the experimental setup of the Third experiment (Order efficiencies and figures of merit, Subsection 4.1.3) into a new configuration shown in Figure 4.12. This 'comparison' setup was based on the same X-Y motorized platform, two 637nm CW lasers for simultaneous wide-field illumination (Figure 4.13 **a**) and MS-TIRF (the beam reaching the metasurface from above and being coupled into the substrate, Figure 4.13 **b**), an Olympus UPlanSApo 40X NA 0.95 air objective and the same ANDOR iXon Ultra camera. This configuration gave us firstly the capability to show we can excite some fluorescent particles using only the laser coupled into the substrate through the metasurface, i.e. with MS-TIRF, and secondly it also allowed us to compare the signal-to-noise ratio (SNR) difference between traditional wide-field and TIRF illumination. The typical distance between the MS and the center of the substrate where the fluorescent sample is placed is 20mm (in green and orange color in Figure 4.12).

4.2.2 TIRF Condition

The first task carried out with the setup described in Subsection 4.2.1 was to verify that we could indeed use our fabricated metasurfaces to selectively excite fluorophores in close proximity to the substrate's surface, while keeping the bulk of the specimen

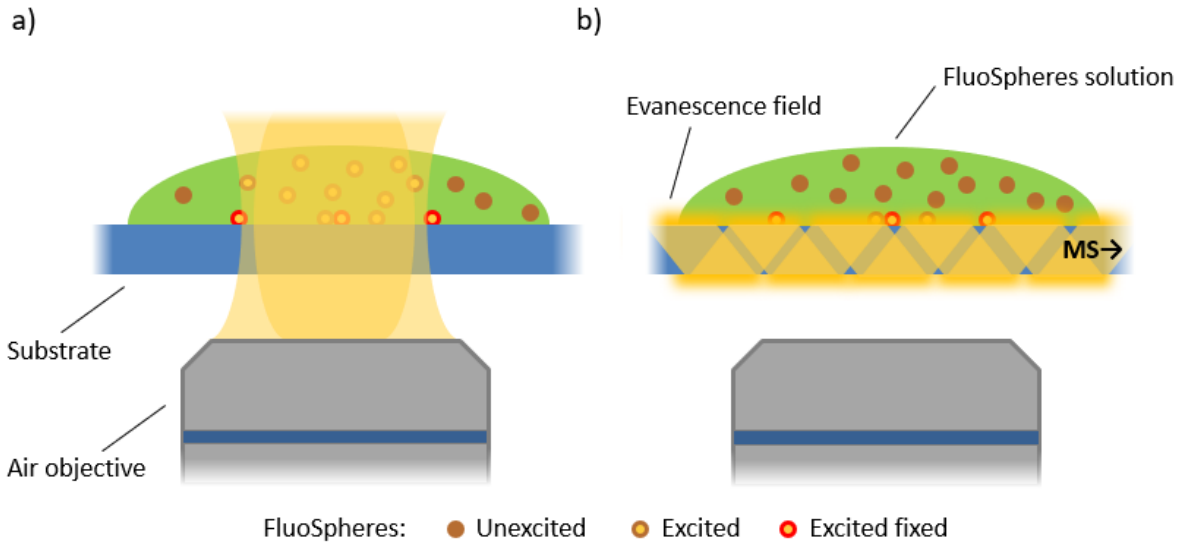

Figure 4.13 – Inverted microscope scheme with two 637nm lasers for 2 possible configurations, WF illumination (**a**) where both fixed and diffusing FluoSpheres are excited, and MS-TIRF illumination (**b**) where the MS, not shown in the image is responsible for the necessary evanescent field.

unaffected, in the dark as is the case with traditional TIRF techniques.

For this purpose a highly diluted solution of fluorescent particles (Invitrogen™ FluoSpheres™ Carboxylate-Modified Microspheres, 0.2 µm, dark red fluorescent 660/680 0.0001% in volume) was prepared and used for a simple qualitative TIRF test:

1. A microdoplet of the solution was deposited on the center of the coverslip, followed by the same volume of water to further dilute it, and left to dry fixing some fluorescent particles onto the surface.

2. By depositing a second, larger (5-10µl) droplet of the solution, we obtain a state in which some particles are immobile in the surface, and a much larger number of particles are diffusing in water with some of them occasionally bumping against the surface but the vast majority several microns to millimeters away from the glass.

3. We captured series of hundreds of images, with a total acquisition time of 12 seconds during which we alternated between widefield illumination, MS-TIRF illumination or both.

Figure 4.14 shows two frames of a series of 200 frames, each with a 100ms integration time, for a resulting 20 seconds video. With 10 seconds of WF illumination, followed by 10 seconds of MS-TIRF illumination, we observed a clear distinction between a bright and effervescent rapid diffusion activity of the microspheres in the bulk of the solution, followed by an almost static image of those particles fixed to the surface, and markedly improved contrast of those in-focus FluoSpheres. While at 100ms integration time per frame on MS-TIRF illumination we rarely saw the rapid event of a free microsphere touching the surface, reducing the integration time let us visualize the 'blinking' effect of particles diffusing down and entering the evanescent field, becoming visible for an

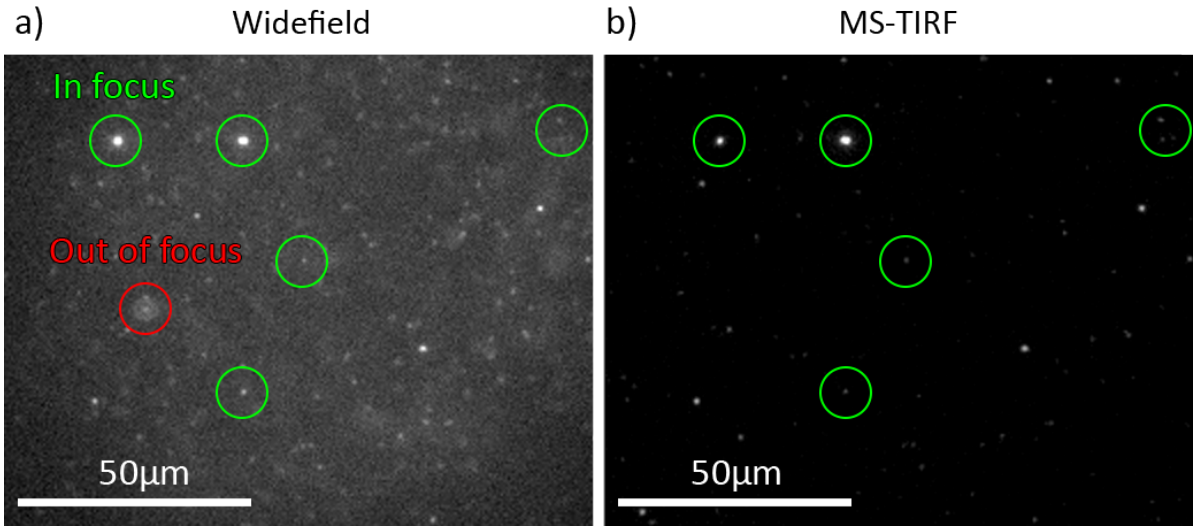

Figure 4.14 – Two frames of an image series before (**a**) and after (**a**) switching from WF illumination to MS-TIRF as the only excitation source for the 0.2 µm Invitrogen FluoSpheres. Integration time: 100ms/frame. While WF allows us to see the rapid movement of the diffusing particles in the bulk of the solution, it also partially hides the fixed particles in focus in the glass surface. MS-TIRF illumination manages to selectively excite those focused microspheres, removing the intense background produced by the diffusing particles. For shorter integration times, the occasionally particle bumping into the surface and blinking for an instant, during its stay within the evanescent field is also visible.

instant, to quickly continue their path returning to their dark state. Finally, by analyzing the MS-TIRF frame in 4.14**b** we can obtain the maximum and mean pixel value of the bright fluorescent particles and the background noise standard deviation, resulting on a signal-to-noise ratio of 55 and peak-signal-to-noise ratio (PSNR) of 120[96].

4.2.3 Bioimaging

In order to exploit the unusually large field of view offered by MS-TIRF, the biological sample consisted on bone marrow Human Mesenchymal Stem Cells (hMSC-bm) immunostained[3] with anti-Paxillin and anti-rabbit IgG Atto 647N and finally mounted (i.e. encapsulated in aqueous media). When cultured these cells can reach several hundred microns in size, often well beyond the FOV of TIRF objectives. While fixed cells have been the preferred option for this initial biological long-lasting experiment, no performance difference is to be expected for live samples of the same type.[4]

With the biological sample in place in the MS-TIRF setup (Figure 4.12), we successfully obtained a series of high-contrast images with the immunostained cells exclusively excited by the MS-generated evanescent field. Similarly to the test with FluoSpheres™ in Subsection 4.2.2, the observable section of the cells is reduced to only a thin slice in close proximity with the glass surface, greatly reducing the out-of-focus light captured

[3] The use of an antibody-based method to detect a specific protein in a sample.

[4] *The sample preparation work was generously done by Lara Hauke at Georg-August-Universität, Göttingen, Germany. The detailed process can be found in Appendix .5.*

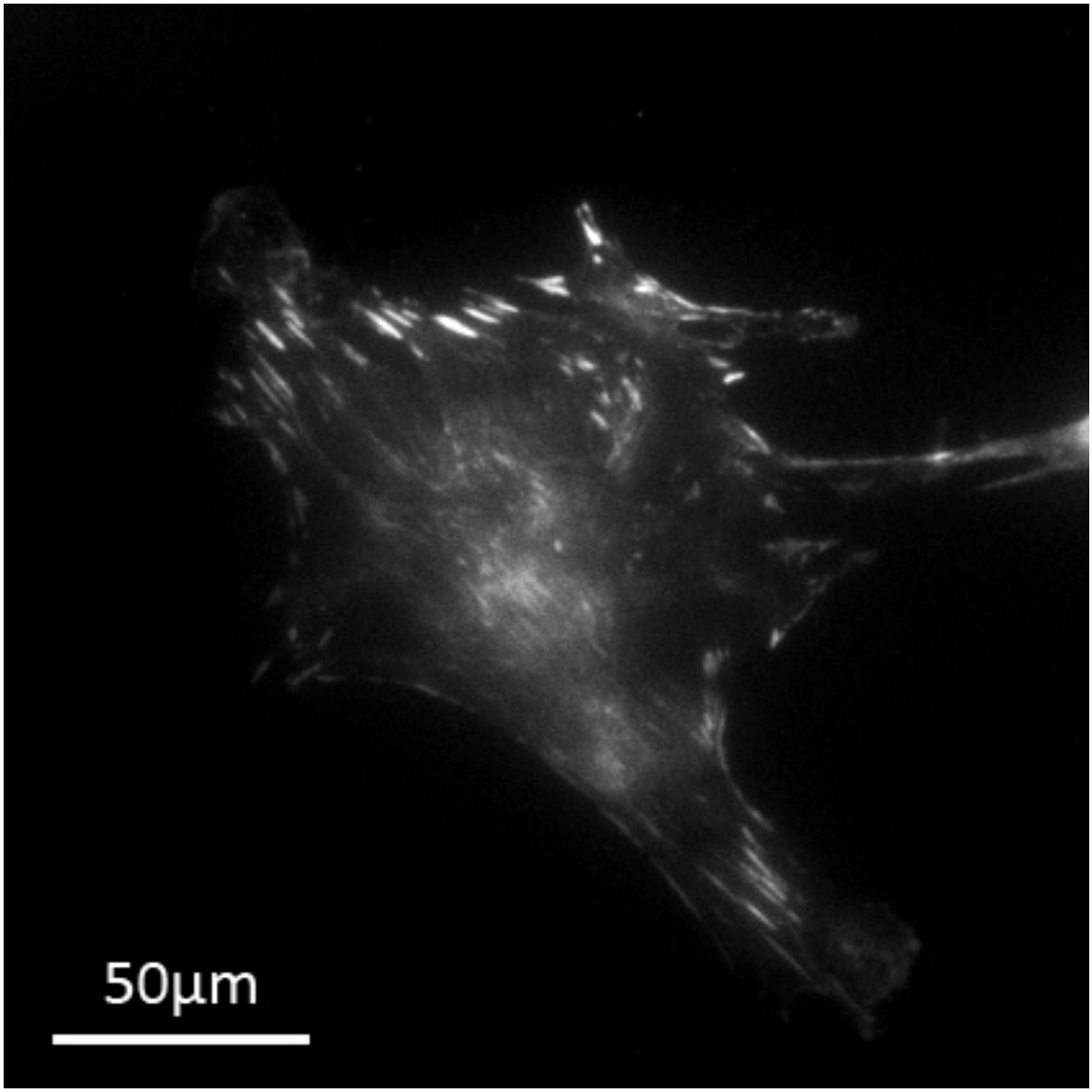

Figure 4.15 – A single 200µm-large bone marrow Human Mesenchymal Stem Cell imaged using our 2D metasurface substrate for MS-TIRF. Despite the fluorophore concentration is higher on the cell's focal adhesions, their intensity can often be too dim in relation to the out-of-focus light captured from the bulk of the cell. A direct comparison with a standard widefield image can be seen in Figure 4.16

.

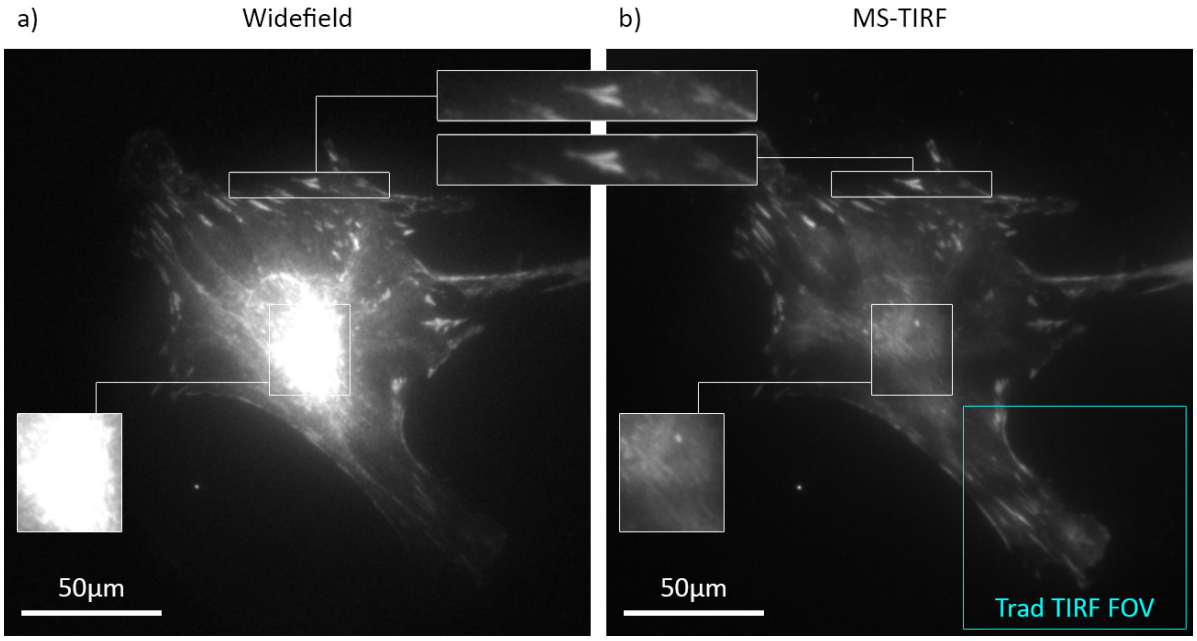

Figure 4.16 – Bone marrow Human Mesenchymal Stem Cells stained with Atto 647N imaged with (**a**) a standard widefield microscope and (**b**) a MS-TIRF substrate.

by the air objective. Figure 4.15 is one of such images, where there is a clear intensity distinction between the focal adhesions and the rest of the cell. Despite those specific points having a higher fluorophore concentration which could justify their relative brightness, Figure 4.16 show us the existence of an even higher concentration on the cell's nucleus, which is virtually invisible on the MS-TIRF image. With a visible square surface of 250µm, these MS-TIRF images are only using less than 1/3 of the FOV of the 40X objective (assuming a square CCD within the FOV), while showing already ten times the surface obtained with our 100X TIRF objective (a 80µm wide square image).

In Figure 4.16 we compare one cell's image obtained with a Olympus UPlanSApo 40X (NA 0.95 Air) objective with widefield illumination (**a**) and MS-TIRF (**b**). Considering the staining technique employed was chosen to preferably mark the cell's focal adhesions[5] in the membrane, some of which are in direct contact with the glass, we used one of these sites of interest in the images to normalize their intensities (inset top center). In particular, we can observe a significant different in contrast around all these sites (seen as short bright lines) and also how the relative extreme brightness of the cell's nucleus completely saturates the central part of the WF image. MS-TIRF illumination can almost completely eliminate the effect of such bright points well inside the bulk of the cell, letting the user capture the texture and detail of the membrane underneath.

Space-Bandwidth Product

The Space-Bandwidth Product (SBP) is a mean to quantify the combination of resolution and field of view of an objective, which can also be translated into the amount of information that in can transmit. With existing techniques exploiting large SBP

[5]Sub-cellular structures that mediate the regulatory effects of a cell in response to extracellular matrix adhesion.

objectives to go beyond the resolution usually obtained with low magnification air objectives[97] (using different illumination angles) a large-FOV, high-SBP MS-TIRF could offer some unique potential. Figure 4.17 is a cropped section of an objective-based TIRF image taken with a 100X NA1.49 enlarged (with no interpolation) enough to be able to distinguish individual pixels[6]. The entire image in the green circle had its resolution digitally reduced 50% to emulate the resolution attainable by a NA∼0.95 objective[7], with the exception of the blue circle where the full resolution was kept. Simultaneously, two color circles have been proportionally scaled to visually represent the difference in FOV between a 100X FN=22 and a 40X FN=26.5 objectives, specifically the ones used for the experiments in this section, with a FOV of 660µm and 220µm respectively.

The SBP can be also expressed as the minimum amount of pixels needed to capture all the information provided by the objective's resolution and FOV. This is simply the FOV circle divided by the pixel size required to achieve Nyquist sampling at the resolution given by the objective's NA and illumination wavelength. Using the laser source and objectives described in Figure 4.17 we calculated a SBP of 2.2 megapixels (100X NA 1.49) and 8.2 megapixels (40X NA 0.95), almost 4 times as much information in favor of the lower magnification objective. This number could climb up to almost 6 by using a water 40X NA 1.2 objective (∼6500$), further reducing the resolution difference with a traditional TIRF objective. There are also special-oil and special-coverslip TIRF objectives with an extremely high numerical aperture of 1.7 costing more than 3 times the aforementioned water objective.

[6]Due to the proper matching between the optical and camera resolution, we can know we deal the minimum number of pixels to represent all the available information provided by the objective. Under this condition, a reduction in the number pixels for the same image emulates accurately a reduction in optical resolution.

[7]By turning 3 pixels into 2 by nearest neighbor.

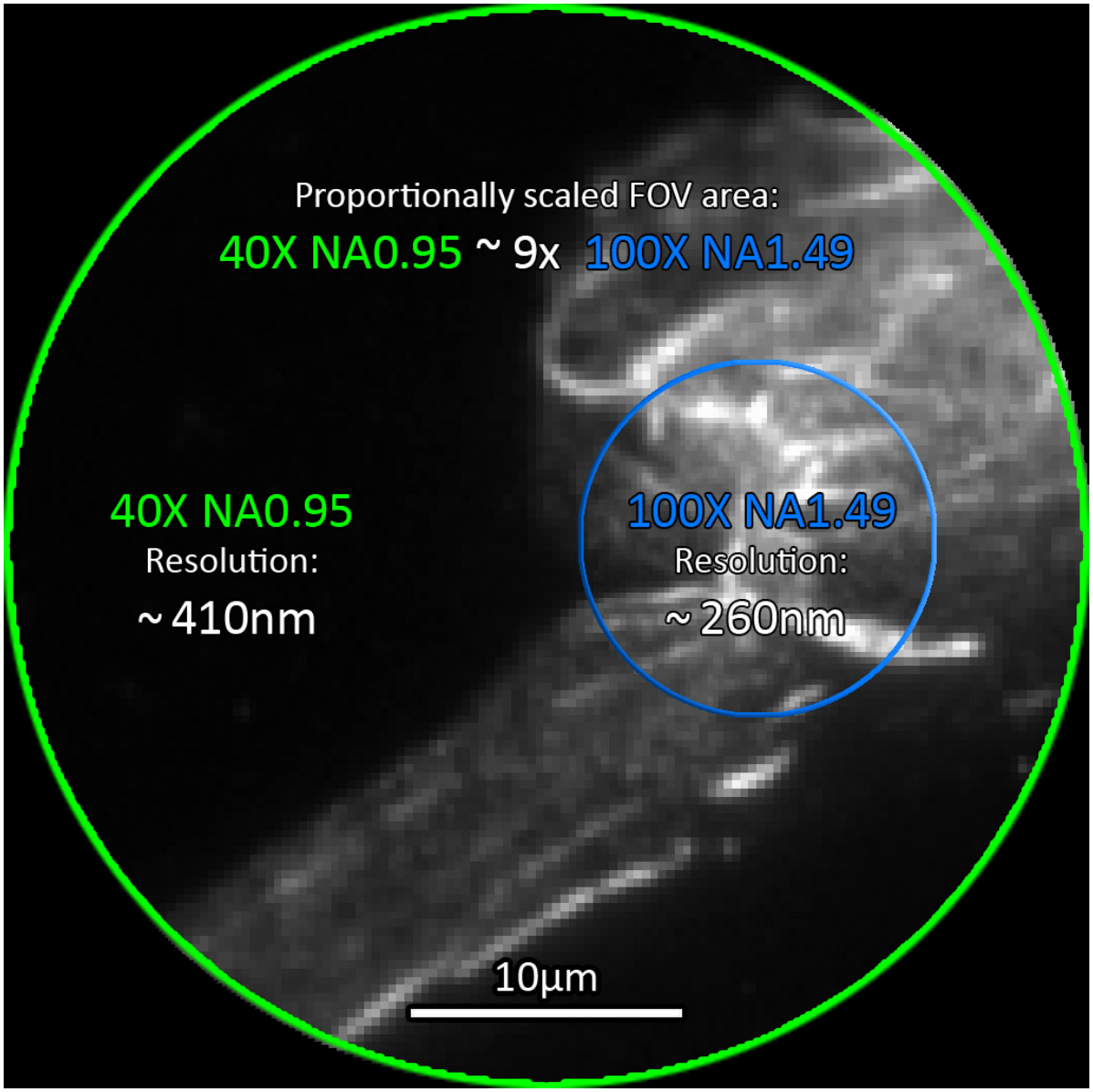

Figure 4.17 – The space-bandwidth product (SBP) of an objective, a combination of its resolution and FOV, express the amount of information that it can transmit. In this example we portrait the proportionally scaled down FOV of the objectives used in these experiments: An Olympus UPlanSApo 40X NA0.95 FN0.95 and a UApo 100X NA1.49 (in green and blue respectively), the later capable of resolving 35% smaller features that the former, but only on an area 9 times smaller. The SBP scales as NA^2/M^2 and results almost always favorable for lower magnifications objectives. Resolution shown for 640nm.

Chapter 5

Conclusions and perspectives

5.1 MS-TIRF

The ultimate goal of this project consisted on utilizing a metasurface as a light coupling instrument for TIRF microscopy, and it is safe to say that this objective was achieved. The Human Mesenchymal Stem Cells images obtained using one of our 2D MS showed the typical high contrast characteristic of TIRF microscopy on a single frame (measured peak SNR of 120), even with cells that extend well beyond the typical FOV of objective-based TIRF. The direct comparison with widefield illumination also reveals the optical sectioning achieved by an evanescent field, leaving unexcited the nucleus of the cell that otherwise would outshine any underlying part of the cell.

Using the microscopy objectives described in Chapter 4 we also calculated the space-bandwidth product available with our Ms-based TIRF implementation, resulting in almost 4 times more information being captured by the 40X air objective in comparison to a typical TIRF objective, with only a reduction factor of 1.5 in the horizontal resolution. As we mention in the perspectives for future MS designs in Section 5.2, one area that we think should be addressed is the field homogeneity, that is already a challenge on traditional TIRF microscopes and becomes increasingly challenging with a FOV 9 times larger, as we obtain with MS-TIRF. In that section we provide 2 strategies that could potentially help to tackle this effect with minimal changes, basically implemented on software. Figure 5.1 shows one of the most severe cases and Figure 5.2 a more typical case.

5.1.1 Diffraction order measurements

In subsection 4.1.3 we described the experimental setup employed to measure the angle and intensity of the transmitted diffracted orders, which relied on a high-NA TIRF objective to capture those high-angled orders, that otherwise would not escape the substrate. While effective to evaluate the performance of our designs and fabrication process, we did realize the need to obtain spectral information to further corroborate and strengthen our simulation accuracy. For this purpose we designed and mounted an upgraded version of said experiment, shown in Figure 5.3, adding two more CW lasers (532nm and 406nm) and one supercontinuum (KOHERAS SuperK Compact SCB-

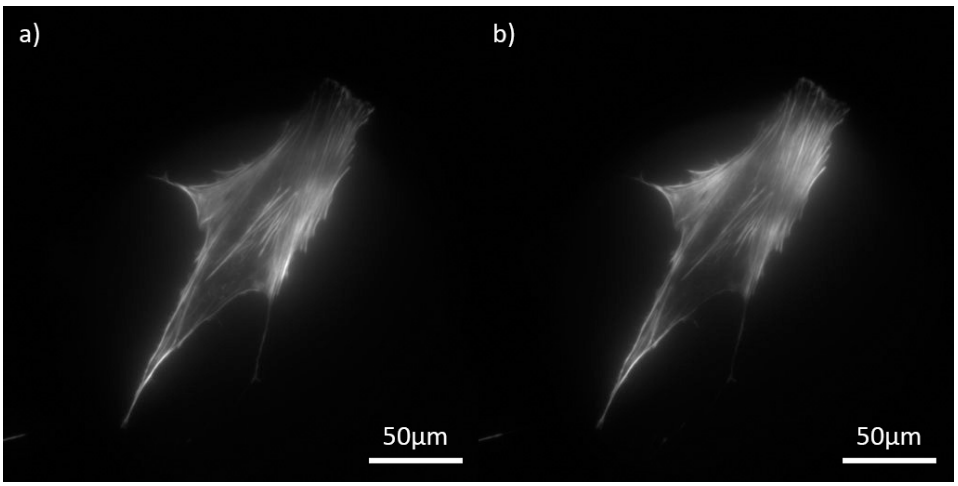

Figure 5.1 – The excitation field inhomogeneity observed in some cases like in these hMSC images (40X NA 0.95 obj.) could be addressed by minor modifications on the MS periodicity and shape, intentionally increasing the divergence of the coupled beam, detailed in Subsection 5.2.2.

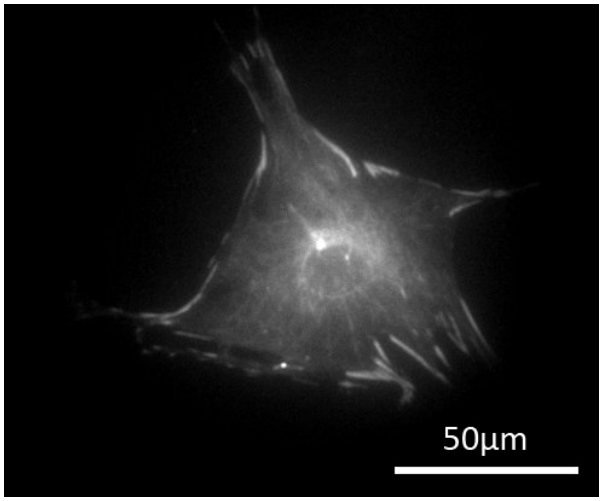

Figure 5.2 – While cases like those shown in Figure 5.1 can occur depending on the specific position of the cell with respect to one of the beam's internal reflections, we do not regularly observe such marked intensity changes across the image (60X NA 0.7 obj.).

Compact 100-PC) into the excitation side of the experiment, and sent the collected diffraction orders to 2 cameras (both first orders) and one spectrometer (zero order) instead of the single camera previously used.

With this supercontinuum source, in the BFP of the objective[1] where before we had one single monochromatic focus point for each diffraction order of the MS, now we have one white point for the 0^{th} order and two white beams refracted in a rainbow-like line, one on each side. This is caused by the different diffraction angle transmitted by the MS for different wavelengths, later focused by the objective in a different position of the BFP. The three monochromatic CW lasers function as calibration points to be able to overlap the images of the BFP taken while illuminating with the supercontinuum laser to those taken while illuminating with 3 known wavelengths (406nm, 532nm and 632nm). This allowed us to correlate different wavelengths to different positions on the cameras sensors, with the pixel intensity on such positions corresponding to the efficiency at that wavelength.

A custom MATLAB script was developed to load all those images coming from the set of 4 lasers and different MS samples, identify the white-laser lines and align them, as well as the monochromatic calibration positions to calculate and reconstruct a spectral measurement over the camera images. While the two first orders (positive and negative) are spread by color over a short line at the CCD1 and CCD2 sensors, that is not the case with the 0th order which is analyzed with a diffraction-grating-based spectrometer (Princeton Instruments ACTON SP2500).

Unfortunately we did not manage to obtain definitive results in time. Measurements, and its agreement with our simulations depends not only on the experimental setup but the overall quality of the MS tested. While we did obtain what seemed to be a spectral response matching our simulations for one individual MS, we did not find the same level of agreement in future measurements. Also, while not affecting the shape of the spectral curve retrieved from the image, we detected condensation on the cooled down sensor surface, generating sudden dips as light touched the droplets formed on the CCD. Considering the same software was used for all MS measurements, we regard a misalignment as the most likely cause for the later measurements. Nevertheless, we consider this measurement to have an important role to further solidify the numerical basis of our metasurface design process and should be continued wherever possible, ideally using the latest MS fabrications, not available at the time of this experiment.

5.1.2 Simplified order measurements

We think the method described in the previous subsection could potentially be enormously simplified. We envision a MS testing device (Figure 5.4) consisting on a glass spacer mounted directly in between a high resolution CCD and the MS substrate. When the MS is hit with a normal incident beam, the spacer thickness should be such that the 3 main diffraction orders fall within the surface of the CCD. By calibrating any possible angle dependency of the pixel's sensitivity, we could measure the angles and efficiencies for all spectral components of the light source in a matter of seconds. All the gaps between the glass surfaces and the CCD should be filled with immersion oil

[1] Or close to it due to the slight divergence of the incoming beam not portrayed in Fig. 5.3

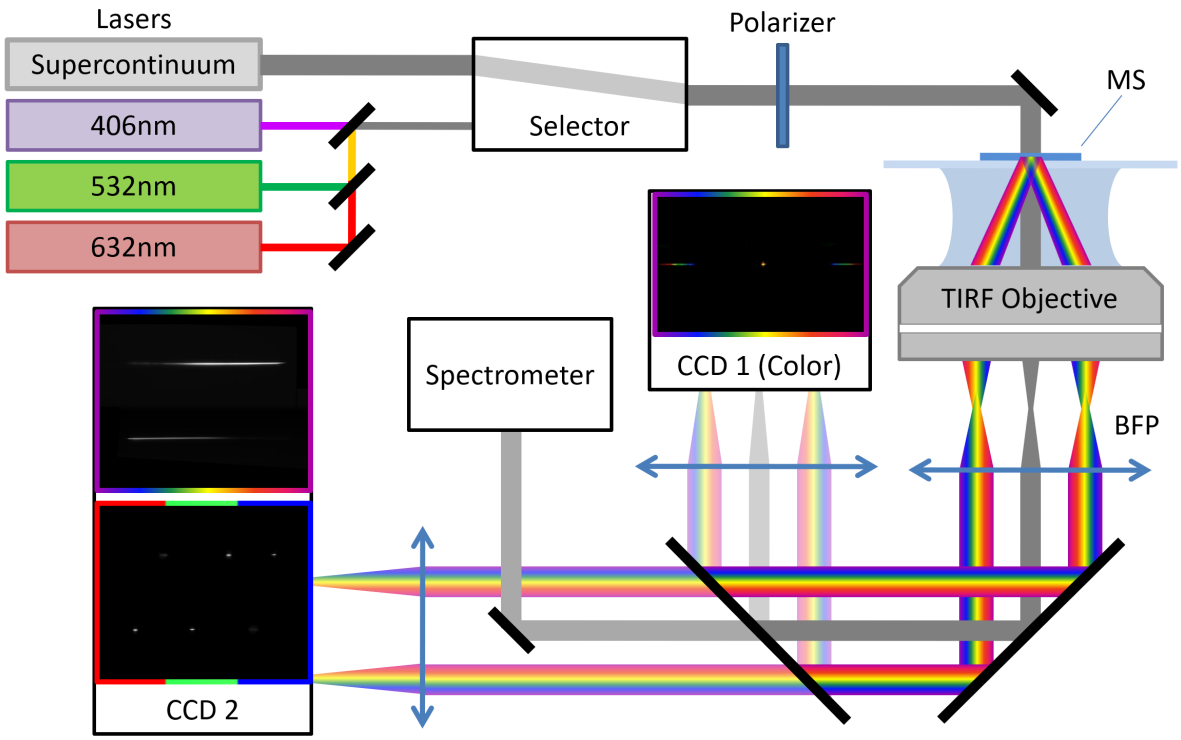

Figure 5.3 – Adaptation of the first setup (4.5) for a supercontinuum laser source, allowing to obtain spectral information of the metasurfaces. P1 is a linear polarizer cube, L1 a f=300mm achromatic doublet (AD), L2 a f=100mm AD, L3 a f=50mm AD, L4 a f=500mm lens and BS1 a 50/50 beamsplitter. CCD1 corresponds to a Canon M3 APS-C mirrorless camera and CCD2 to an Andor Zyla DG-152V-C1E-FI.

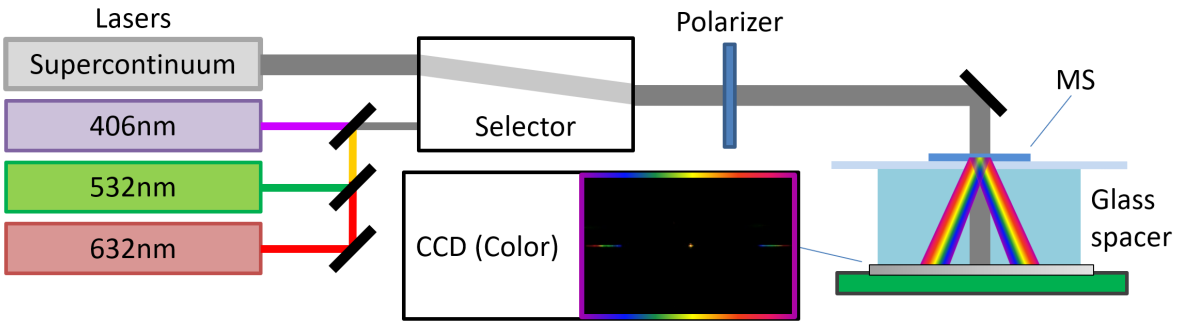

Figure 5.4 – A much simplified concept of Fig. 5.3's experiment using only a glass spacer and a high resolution CCD where all diffraction orders generated by the MS are projected and measured at once.

or optical adhesive to avoid spurious reflections. The sensitivity requirements for the sensor would be minimal, due to the relative high intensity of sources and negligible system losses, and a commercial 35mm sensor (36x24mm) could easily offer 6000 pixels along its width. Such sensor would be allocating approximately 1000 pixels for each of the 1^{st} diffraction orders, a short rainbow-like segment ranging from 400nm to 700nm in our third experiment (Subsection 4.1.3).

5.2 MS Design

Departing from a study of the behavior of double groove 1D gratings in 2014[65], we successfully conceived several novel 2D metasurfaces. This structures displayed first diffraction order efficiencies as high as $\eta_{-1}0.6$, while greatly suppressing the direct transmission ($0.005<\eta_0<0.04$), both required conditions for a powerful TIRF coupling device. Our bidimensional designs helped us to simplify the fabrication and gain more degrees of freedom for better MS-TIRF performance. These designs were developed taking into account current nanofabrication capabilities but not limited by them, as we believe some of the more challenging designs will be within reach as TiO_2 patterning processes continue to evolve.

Some of these designs were subsequently fabricated and characterized to validate our simulations, with the best performant metasurfaces later used for a MS-TIRF proof of concept. The experiments carried out on on those samples showed good agreement with the expected behavior of the metasurfaces, and we expect further developments on the fabrication process to continue to improve such agreement.

Even at this point with several TIRF metasurfaces proposed and fabricated, we consider that more efforts put into the software tools developed for this task could convey just as much gains as an enhanced fabrication process.

5.2.1 Optimization algorithms

In order to be able to find optimal designs in a space of 9 dimensions and trillions of points, a significant amount of effort was put into developing the fastest search strategy

possible. Although there is no direct causality between the efficiency of the algorithm and the performance of the resulting devices, in practice smarter and more efficient methods allow us to widen the scope of possible designs considered and more often than not, arrive to better and more intricate designs. In this project, all the metasurfaces designed beyond the very first 1D structures were only possibly thanks to these algorithms, which required their own battery of tests and analysis not discussed in this document. It is the author's belief that further refinement of the software tools used would most definitely lead to novel and more capable structure designs. Strategies more sophisticated than gradient ascent have already been tested with great success for similar applications, in particular inverse design optimization algorithms that allow for vastly more irregular pattern shapes than those considered in this work, including periodic and aperiodic structures[57, 66, 98], utilizing iterative methods such as adjoint-based topology optimization, artificial neural networks[99, 100, 101] and advanced evolutionary strategies and statistical learning[102].

5.2.2 Improvements on the design

We think the next generation of MS designs should accommodate for some relatively simple changes that we think could greatly improve the overall usability of these metasurfaces.

1. A very important point that is often problematic on traditional objective-based TIRF microscopes as well as MS-TIRF is the excitation field homogeneity, that carries the intensity profile of the excitation beam into the objective's FOV. This can lead to inaccurate measurements of fluorescence intensity or marker's density. With our MS-TIRF approach, there is no strong reason why we should operate at a single diffraction angle, and a slow period gradient on the MS grating (e.g. between $p = 450$ and $p = 460$) could generate a (3°) divergence on the first diffracted order, enlarging each reflection point on the substrate (i.e. waveguide) and homogenizing the intensity in the observed FOV.

2. Following a similar strategy, by arching the MS (e.g. 1.5°) on each direction, we would generate a (3°) divergence in the plane of the substrate, without significantly altering the MS at a local microscopic level. This would homogenize the excitation area, at the expense of field intensity which could be compensated with a higher input laser power with relative ease. Figure 5.5 illustrates these 2 modification proposals.

Complementary to all these modifications, future samples will not need dose MS arrays or size MS arrays like those samples fabricated up to this point (e.g. Fig. 2.7) but will require just one single MS design for each different light source used, occasionally being just one. This in turn leaves an enormous amount of space in the glass substrate, whose typical commercial sizes range in the tens of millimeters (most commonly available slides measure 75x26mm) that can be used to extend the MS along the direction perpendicular to the beam. The advantage for such change is that it uncouples in one dimension the position of the biological sample with respect to the MS (and thus all the TIR points along the substrate), by being able to move the normally incident laser along the Y axis and excite any one point of the biological sample.

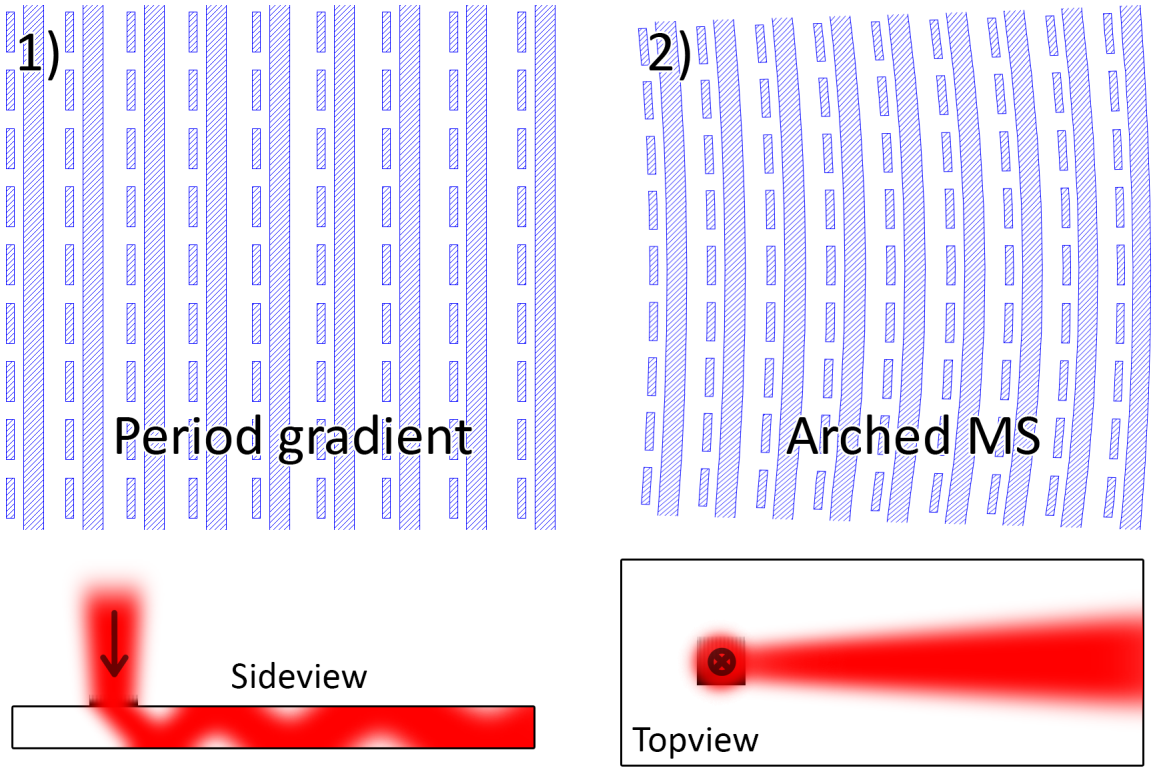

Figure 5.5 – For future MS designs we considered period gradients(1) to generate a divergence on the diffracted light and MS arching(2) to produce an equivalent divergence in the substrate plane.

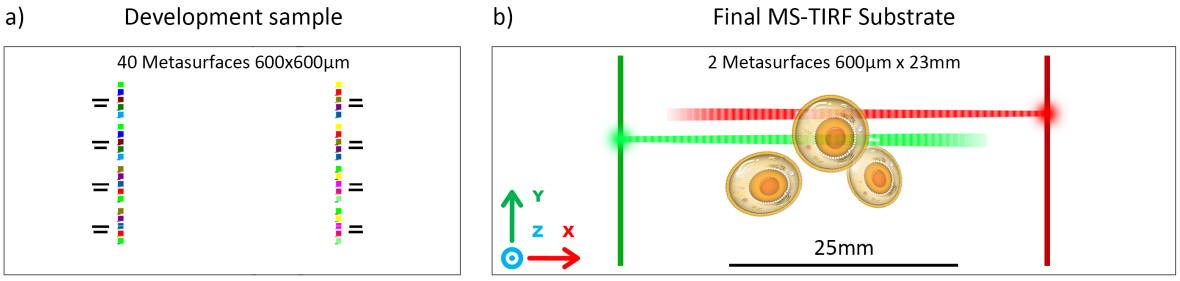

Figure 5.6 – Top view layout of one of our development samples that included dose and size shift arrays in order to fine-tune the fabrication process(a) vs. a proposed final substrate design with only 2 long MS fabricated from side to side of the standard-size microscopy slide(b), allowing the excitation of any point in the biological sample, which is placed in between the metasurfaces. On each side, each MS could be optimized for a different wavelength to have two-color TIRF.

As a final adjustment for future samples, a small 1-3% reduction on the MS period (from p=465nm to p=460/450nm) could improve the TIRF performance in some specific cases: With some exceptions[2], most cell organelles have a refractive index on the 1.36-1.39 range[104], which in contact with a $n = 1.52$ glass substrate could require minimum beam angles as high as 66° to attain total internal reflection (Eq. 2.1). Our current MS designs were optimized for a 65° angle, which could potentially be insufficient for the observation of some of these high-index organelles.

We are confident that our latest TIRF MS designs, with the implementation of the improvements described in this section, could prove to be a valuable addition to the universe of TIRF solutions with unique features that are not currently available for TIRF microscopy end-users.

5.3 Nanofabrication

While the objective of this project was the utilization of flat metasurfaces to perform TIRF microscopy, the complete dependence of this goal on our ability to develop a suitable fabrication process, made this later task effectively as important as our main objective.

We started early in this project evaluating our in-house TiO_2 fluorine-based fabrication process, a relatively common approach for this kind of material. While our metasurface designs had similar or even smaller aspect ratios than those structures for which said process had been developed[51], the difference in the critical dimension, smaller than 50% of the size of those previous patterns (48nm vs. 100nm), resulting in a weak repeatability, with several samples failing during the manual hard mask lift-off, tested both in aluminium and nickel. To improve the reliability of particular step, we implemented what we labeled as our '2^{nd} Generation process' a bilayer soft mask approach which has been reported to greatly improve the post resist-development undercut profile needed for a clean lift-off. We found this to be true in our case, obtaining a significantly higher success rate during the nickel lift-off using a PMMA-MMA soft mask (50+50nm) against the previous PMMA-only 100nm mask.

The following step, i.e. the 230nm-deep TiO_2 fluorine-based CCP etching, proved to be the next challenge. Firstly, the strong ARDE effect caused by intrinsic design of our 1D metasurfaces, constituted of features with aspect ratios as high as 5 in close proximity to others as low as 1 rendered impossible to etch the entire pattern to a even depth. Instead, we were consistently obtaining underetched narrow sections and overetched wide grooves, fully etching the TiO_2 layer and continuing on the glass substrate. This was not only problematic for its lack of fabrication repeatability, but also diminished the predictability power of our simulations and optimization algorithms. Secondly, the etching profile was not as vertical as we sought it to be. While this did not mean that one given MS design was not resilient to this effect, our fabrication objective was aimed to a robust TiO_2 fabrication process that could be used for a wide range of constantly-evolving metasurface designs.

[2]In some cases like lysosomes in EMT6 cells the estimated refractive index can be as high as 1.6[103], which is higher than our current substrate material.

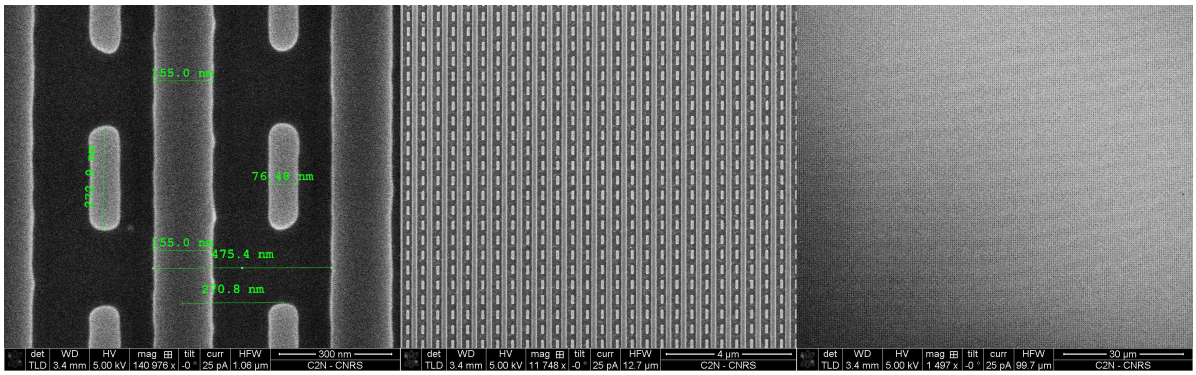

Figure 5.7 – Examples of aluminium hard masks generated by ICP chlorine-based etching. The image on the right has a charge-effect gradient often observed due to the non-conductive substrate.

This triggered two important changes, on one side on the MS design itself in order to make it less susceptible to ARDE effects (2D MS designs), and on the other side a different approach on the fabrication process, specifically conceived as a lift-off workaround. The core of these changes consisted on generating a hard mask by aluminium plasma etching, which thanks to being an highly automated operation produces much more replicable outcomes than a completely manual lift-off. This modification resulted very effective to generate high quality aluminium hard masks, homogeneous across large surfaces, with smooth edges, in a consistent and predictable form, with some examples shown in Figure 5.7. These new masks along with the previous fluorine plasma TiO_2 etching constituted our '3^{rd} Generation process'.

From this point onward, we almost simultaneously learnt that the selectivity of our CCP TiO_2 etching process was not high enough to fully etch our 230nm thick metasurfaces with an aluminium hard mask, even as thick as 80nm, and that by adjusting the ICP plasma process used for aluminium, we could fully etch our TiO_2 layer with a novel chlorine chemistry not previously reported in the literature, using nothing but a 130nm-thick ZEP-520A resist soft mask. This not only eliminated one pattern transfer (no hard mask nor lift-off involved) greatly simplifying the complete process, but produced an extremely vertical etching profile not achieved with any other tested process in the framework of this project, visible on Figure 5.8. Additionally, and despite we did not have the time to fully characterize it, we also used this ICP etching recipe with nickel hard masks generated with the older PMMA-MMA bilayer technique, and also showed a sufficient selectivity to fully etch those metasurfaces, a promising result that we consider worth exploring.

Despite the time limitations imposed by the temporal shut-down of our clean room facilities that did not allow an in-depth characterization of this novel TiO_2 etching chemistry, based on our last results we think this process could be further refined to easily etch beyond 230nm, high aspect ratio structures, offering great potential not only for our metasurfaces but other types of structures as well, predominantly metalenses, whose scope of application goes well beyond optical microscopy[43, 31, 42]. To the best of our knowledge, there are no records of HBr/BCl_3 chemistries used to etch TiO_2 thin films.

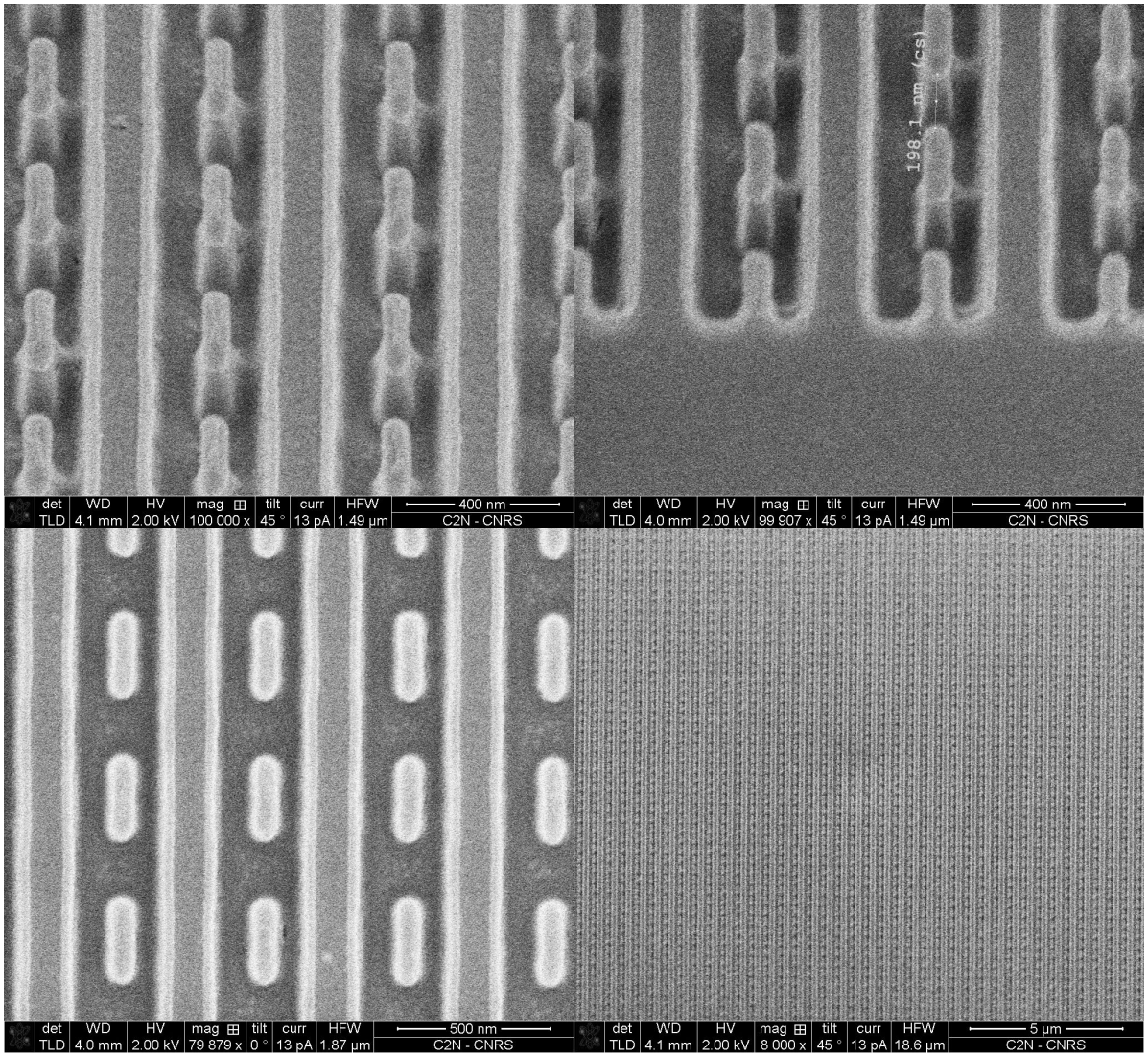

Figure 5.8 – Our last and final TiO_2 metasurface fabrication process based on a chlorine ICP etching chemistry resulted clean smooth edges, vertical walls and homogeneous millimeter-sized surfaces while requiring fewer steps and shorter times than all previously tested processes.

5.4 MS-TIRF Device

We define the concept of *'MS-TIRF device'* as the complete microscopy tool package that achieves a TIR evanescence field with the aid of one or more metasurfaces. For one specific MS design and fabrication, other factors such as the glass substrate size, its thickness, refractive index, shape, the position of the MS within it surface, or the illumination method could result on different devices, with varying degrees of functionality depending on the application or microscope type.

During the last three chapters we introduced and discussed the design, fabrication and testing methods of a series of metasurface gratings capable of couple an incident beam into a substrate to perform TIRF microscopy, with this last key step performed using one particular experimental configuration described in Section 4.12. While fully functional, such setup may not always be the optimal way to use these metasurfaces in the context of a wider audience operating a wide range of commercial optical microscopes with significant differences between them. We understand that in order to reach a high level of practicality, even a perfect MS (i.e. extremely high diffraction order efficiency for just one single transmitted first order, minimal efficiency for all the others) will require an effective and simple mean to use it.

5.4.1 External illumination

By 'External illumination' we specifically refer to a very weakly focused TE-polarized laser beam reaching the metasurface fabricated on the microscopy substrate. With this approach, the balance between the simplicity of the device and the external equipment required favors the device, that consist on a completely passive element and leaves to the user to find a way to reach the MS on the device with a laser beam. On this category we tested two possible configurations (i.e. 2 'devices') and conceived a third option that would require changes on the MS design.

1. **Device 1**: This device, being the simpler approach was the configuration used on our MS-TIRF imaging tests on Section 4.2 and is shown in Figure 5.9(**a**). As shown in Figure 2.7 it consists of one or many MS around the center of a 25x50mm coverslip (or a thicker slide, depending on the working distance of the objective). For a 170µm-thick coverslip, the maximum size of the MS is 0.6 x 25 mm[3], where the external laser source will reach the device. This approach requires the physical space close to the microscope's sample holder and optomechanics to have such beam polarized and weakly focused on the MS, a simple task on an experimental microscope but potentially inconvenient on a commercial microscope, where the space directly above and under the sample holder is often taken. The main advantages of such device are its simplicity and the long distance between the MS and the fluorescent sample, which further reduces the impact that any possible scattering or residual 0^{th} order transmission could have. The MS can be situated on either side of the substrate, with the added benefit that if it is placed on the opposite side of the biological sample, there is virtually no risk of stray light reaching the sample and downgrading the quality of the image.

[3]For λ = 640nm, and a substrate RI of 1.52.

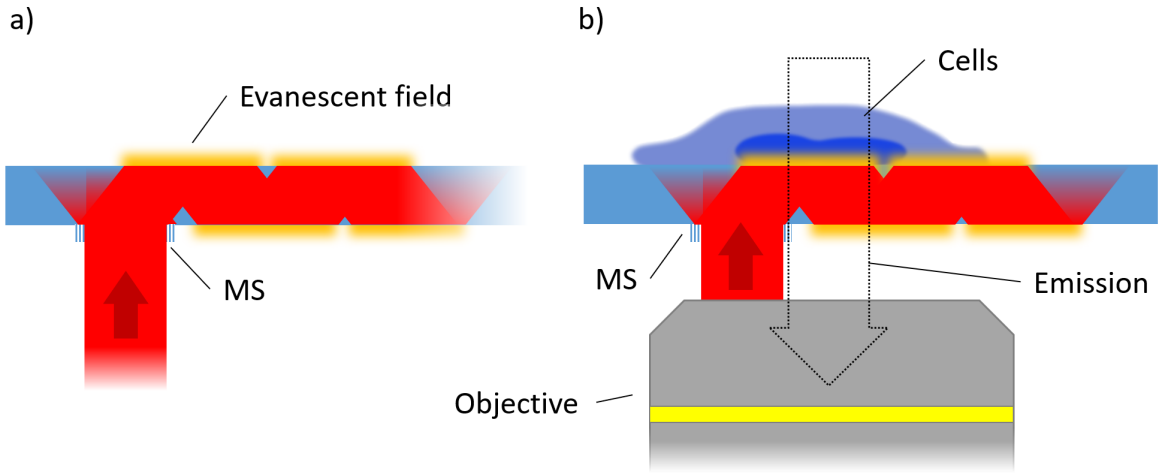

Figure 5.9 – The two device configuration tested in this project: A simpler approach (a - Device 1) consists in external optomechanics to reach the MS substrate with a normal incident beam is the faster option on research microscopes and environments but can be challenging on commercial microscopes with limited space around the sample holder. An alternative option (b - Device 2) uses the lateral port of often found on commercial microscopes to focus the excitation beam diagonally on the BFP of the objective, reaching the very edge of the objective's rear lens. In turn, in all objectives tested this generates a highly collimated beam exiting the front lens vertically, outside the FOV of the objective right under position of the MS. The glass coverslip is shown in light blue. In (a) the objective is not shown, taking any position at the right of the incident beam.

2. **Device 2**: A second alternative that still uses an external source but reduces to the minimum the amount of required mechanics to illuminate the MS consists on a "through the objective" approach, visible in Figure 5.9(**b**). Using one of the lateral ports found on many popular commercial microscopes, and focusing the excitation beam on the center of an air/water objective's BFP at an angle, it is possible to have a normally collimated beam exiting the objective's front lens. If the incident angle at the BFP is sufficiently high, the exiting beam will move away from the axis while staying parallel to it, even beyond the objective's FOV[4]. By placing the MS right on the very edge of the FOV, we can use this beam to excite it without being visible on the CCD image of the FOV. The collimated beam reaching the MS is then deflected towards the center of the FOV, generating the required evanescent field. The downside of this configuration at this stage is its difficult alignment and single excitation point (within the FOV), while its main advantage is the minimal external mechanics needed to implement it and the fact that any residual scattering takes place on the opposite side of the biological sample.

3. **Device 3**: While up to this point we have designed and fabricated metasurfaces aimed at diffracting light at angles over 60° to satisfy TIR in a glass-water interface, based on our experience reducing this requirement would translate into higher efficiencies and easier fabrications. On the other hand, it is also common to

[4]This non-standard use of an objective has been tested possible in all 4 of the air objectives available, with all showing a maximum exit circle for a collimated beam around twice as large as the FOV. To the best of our understanding, this should be the case with the majority, if not all, microscopy objectives.

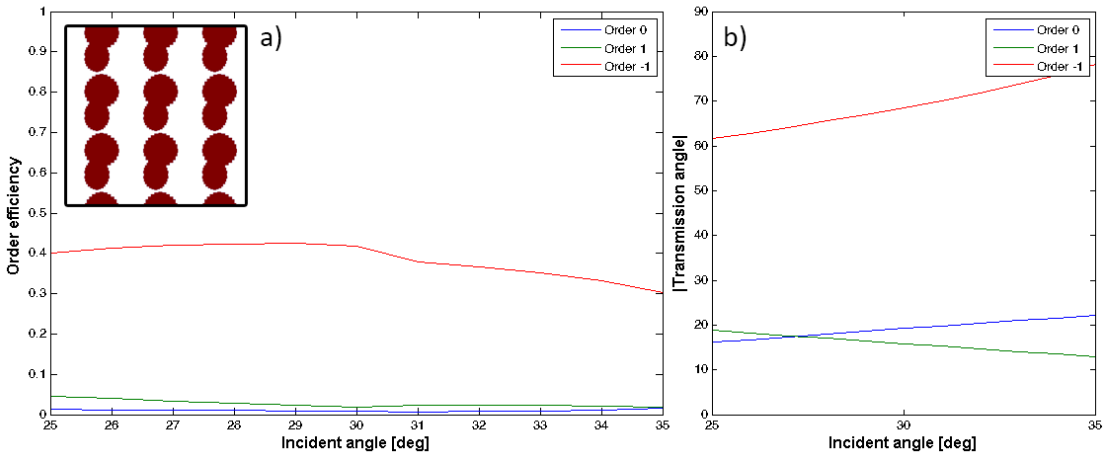

Figure 5.10 – Simulated diffraction order efficiencies(a) and transmitted angles(b) for a 2D MS design optimized for an oblique incidence at 30° that adds to the diffracted angle to reach the TIR in a glass-water interface. The relaxed angle requirement for the MS means that higher a ratio R_3 can be reached (15.2 in (a) at 30°). Inset: Design of such 2D MS, with p=700nm.

have commercial microscopes where there is limited room for any external element directly above or under the sample holder, blocked by the objective on one side, and often some epi-illumination instrument on the other. With this in mind, we simulated a MS designed for a 30 degree incidence angle, which is added up to the 45 degree diffraction order angle and results on a beam that satisfies TIR condition. The less demanding angle requirement means that higher efficiency ratios (R_3=15.2 in Figure 5.10) can be attained and an oblique incidence could provide a unique way to access substrates in tight spaces. In particular, this configuration could also prove particularly valuable to perform TIRF where thermal isolation between the sample and objective are required, e.g. cryogenic microscopes (e.g. [105]).

5.4.2 Self-illuminated substrate

Going one step further and imagining a TIRF device that could completely decouple the evanescent illumination from the type of characteristics of the microscopy used for the observation, we propose a possible implementation in which the illumination source is not related to the microscope in any way:

1. Laser diode mounted on the substrate right above or under the MS. With a cost 0.30 USD for a standard 5mW diode, the power reaching the MS would be between largely higher than the 100µW to 2mW on our experimental setup. Such diodes can be powered from a battery, have a divergence of only 30°, dissipate a small amount of thermal energy into their environment ($\sim$ 35mW) and their potentially inaccurate wavelength would have a minimal impact on the 2D MS already designed (Fig. 2.29) which are also very robust to small polarization deviations from TE (Fig. 4.9).

2. If those 5mW provided with a laser diode mounted in the substrate were not

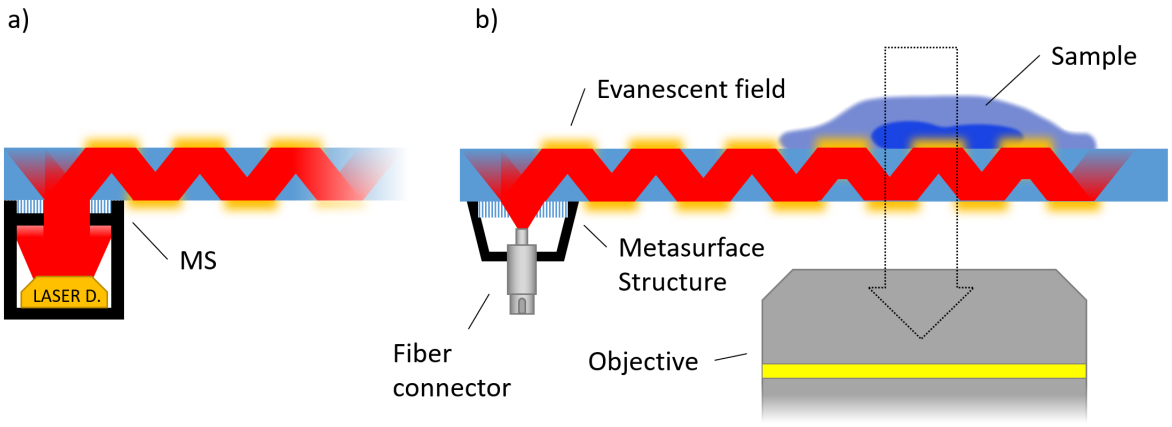

Figure 5.11 – A concept of a MS-TIRF device that incorporates its own illumination source, either on the substrate with a compact inexpensive laser diode (a) or by connecting a fiber-coupled laser (b) when a more powerful source is necessary. Both of this sources could be placed on either side of the substrate to make it compatible with most commercial microscopes.

sufficient, another feasible option would be an adapter that locks in a standard-sized microscopy slide with an optical fiber connector that places the output of an external fiber-coupled laser directly in front of the MS. Such configuration would provide largely more power than regularly found on objective-based TIRF systems due to the direct nature of the illumination system, and in combination with the MS design improvements described in Subsection 5.2.2 the objective's FOV could be fully covered with a large, intense and homogeneous evanescent field.

5.4.3 Next steps for MS-TIRF

Out of range of paths described in this chapter as possible continuations of this work, is the author's opinion that the most promising direction consists of either a MS design on a slightly thicker TiO_2 layer (260nm for λ=640nm based on Fig. 2.17) aiming for R_3 values of around 10, that should be feasible exploiting the high quality etching obtained with the 4^{th} generation process or relaxing the normal incidence condition, which not only would allow for better figure of merit, as shown in Fig. 5.10 but would render the device compatible with a broader range of commercial microscopes. In any case, all final devices should have the MS covering all the substrate width, as shown in Fig. 5.6 with the improvements presented in Subsection 5.2.2 to achieve a field homogeneity superior to traditional objective-based TIRF.

Finally, we consider the laser diode self-illuminated device approach to be a relatively accessible and inexpensive concept to turn into a prototype.

List of Figures

Bibliography

[1] E. J. AMBROSE. "A Surface Contact Microscope for the study of Cell Movements". In: *Nature* 178 (1956), p. 1194.

[2] DANIEL AXELROD. "Cell-substrate contacts illuminated by total internal reflection fluorescence". In: *The Journal of Cell Biology* 89.1 (1981), pp. 141–145.

[3] Berginski ME1 et al. "High-resolution quantification of focal adhesion spatiotemporal dynamics in living cells". In: *PLOS One* 6 (2011), e22025.

[4] Ke Hu et al. "Differential Transmission of Actin Motion Within Focal Adhesions". In: *Science Magazine* 315 (2007), pp. 111–115. DOI: 10.1126/science.1135085. URL: https://science.sciencemag.org/content/315/5808/111.

[5] Ankur Jain et al. "Single molecule pull-down for studying protein interactions". In: *Nature Protocols* 7 (2013), pp. 445–452.

[6] Xiaoqing Liu et al. "Coupling electrochemistry and TIRF-microscopy with the fluorescent false neurotransmitter FFN102 supports the fluorescence signals during single vesicle exocytosis detection". In: *Biophysical Chemistry* 235 (2018), pp. 48–55.

[7] Jos Buijs and Vladimir Hlady. "Adsorption Kinetics, Conformation, and Mobility of the Growth Hormone and Lysozyme on Solid Surfaces, Studied with TIRF". In: *Journal of Colloid and Interface Science* 190.1 (1997), pp. 171–181.

[8] Seamus J. Holden et al. "Defining the Limits of Single-Molecule FRET Resolution in TIRF Microscopy". In: *Biophysical Journal* 99.9 (2010), pp. 3102–3111. DOI: 10.1016/j.bpj.2010.09.005.

[9] Jacqueline Flores-Otero et al. "Ligand-specific endocytic dwell times control functional selectivity of the cannabinoid receptor 1". In: *Nature Communications* (2014). DOI: 10.1038/ncomms5589. URL: https://www.nature.com/articles/ncomms5589.

[10] Andrea L. Stout and Daniel Axelrod. "Evanescent field excitation of fluorescence by epi-illumination microscopy". In: *Applied Optics - OSA* 28.24 (1989), pp. 5237–5242.

[11] Yoshihiro Kawano et al. "High-numerical-aperture objective lenses and optical system improved objective type total internal reflection fluorescence microscopy". In: *Proceedings, Optical Devices and Diagnostics in Materials Science*. Vol. 4098. San Diego, CA, United States: SPIE, 2000.

[12] Jordan R. Beach et al. "Nonmuscle Myosin II Isoforms Coassemble in Living Cells". In: *Current Biology* 24 (2014), pp. 1160–1166. DOI: http://dx.doi.org/10.1016/j.cub.2014.03.071.

[13] Laurence J. Young, Florian Ströhl, and Clemens F. Kaminski. "A Guide to Structured Illumination TIRF Microscopy at High Speed with Multiple Colors". In: *Journal of Visualized Experiments* 111 (2016). DOI: http://dx.doi.org/10.3791/53988. URL: https://www.jove.com/video/53988.

[14] Peter Kner et al. "Super-resolution video microscopy of live cells by structured illumination". In: *Nature Methods* 6.5 (2009), p. 339. DOI: http://www.nature.com/doifinder/10.1038/nmeth.1324.

[15] Min Guo et al. "Single-shot super-resolution total internal reflection fluorescence microscopy". In: *Nature Methods* 15 (2018), pp. 425–428. DOI: https://doi.org/10.1038/s41592-018-0004-4.

[16] Reto Fiolka, Markus Beck, and Andreas Stemmer. "Structured illumination in total internal reflection fluorescence microscopy using a spatial light modulator". In: *Optical Society of America* 33.14 (2008), pp. 1629–1631. DOI: https://doi.org/10.1364/OL.33.001629.

[17] Euiheon Chung et al. "Two-Dimensional Standing Wave Total Internal Reflection Fluorescence Microscopy: Superresolution Imaging of Single Molecular and Biological Specimens". In: *Biophysical Journal* 93 (2007), pp. 1747–1757. DOI: 10.1529/biophysj.106.097907.

[18] Abir M. Kabbani and Christopher V. Kelly. "The Detection of Nanoscale Membrane Bending with Polarized Localization Microscopy". In: *Biophysical Journal* 113 (2017), pp. 1782–1794. DOI: http://dx.doi.org/10.1016/j.bpj.2017.07.034.

[19] Anne Beghin et al. "Localization-based super-resolution imaging meets high-content screening". In: *Nature Methods* 14 (2017), pp. 1184–1190. DOI: http://dx.doi.org/10.1038/nmeth.4486. URL: https://www.nature.com/articles/nmeth.4486.

[20] Natalie S. Poulter et al. "Platelet actin nodules are podosome-like structures dependent on Wiskott–Aldrich syndrome protein and ARP2/3 complex". In: *Nature Communications* 6.7254 (2015). DOI: 10.1038/ncomms8254.

[21] Jian Liu et al. "Elliptical mirror-based TIRF microscopy with shadowless illumination and adjustable penetration depth". In: *Optic Letters* 4.13 (2017), pp. 2587–2590. DOI: 10.1364/OL.42.002587. URL: https://doi.org/10.1364/OL.42.002587.

[22] Srinivasan Ramachandran et al. "High performance, LED powered, waveguide based total internal reflection microscopy". In: *Scientific Reports* 3.2133 (2013). DOI: 10.1038/srep02133.

[23] Felix Jünger, Philipp v.Olshausen, and Alexander Rohrbach. "Fast, label-free super-resolution live-cell imaging using rotating coherent scattering (ROCS) microscopy". In: *Scientific Reports* 6.30393 (2016). DOI: DOI:10.1038/srep30393.

[24] Pierre Bon et al. "Label-free evanescent microscopy for membrane nanotomography in living cells". In: *Journal of Biophotonics* 7.11 (2014), pp. 857–862. DOI: 10.1002/jbio.201300095. URL: https://www.ncbi.nlm.nih.gov/pubmed/25538972.

[25] Guillaume Maire et al. “Phase imaging and synthetic aperture super-resolution via total internal reflection microscopy”. In: *Optics Letters* 43.9 (2018), pp. 2173–2176. DOI: 10.1364/OL.43.002173. URL: https://doi.org/10.1364/OL.43.002173.

[26] D. R. Smith et al. “Composite Medium with Simultaneously Negative Permeability and Permittivity”. In: *Physical Review Letters* 84.18 (2000), pp. 4184–4187.

[27] Veselago V G. “The electrodynamics of substances with simultaneously negative values of ϵ and μ”. In: *Sov. Phys. Usp.* 10 (1968), pp. 509–514. DOI: 10.1070/PU1968v010n04ABEH003699. URL: https://ufn.ru/en/articles/1968/4/d/.

[28] Muamer Kadic et al. “3D metamaterials”. In: *Nature Reviews Physics* 1 (2019), pp. 198–210. DOI: https://doi.org/10.1038/s42254-018-0018-y. URL: https://www.nature.com/articles/s42254-018-0018-y.

[29] J. P. Balthasar Mueller et al. “Metasurface Polarization Optics: Independent Phase Control of Arbitrary Orthogonal States of Polarization”. In: *Physical Review Letters* 118.113901 (2017). DOI: http://dx.doi.org/10.1103/PhysRevLett.118.113901.

[30] Mohammadreza Khorasaninejad et al. “Metalenses at visible wavelengths: Diffraction-limited focusing and subwavelength resolution imaging”. In: *Science* 352 (2016), pp. 1190–1193.

[31] Wei Ting Chen et al. “A broadband achromatic metalens for focusing and imaging in the visible”. In: *Nature Nanotechnology* 13 (2018), pp. 220–226.

[32] Prasad P. Iyer, Mihir Pendharkar, and Jon A. Schuller. “Electrically Reconfi gurable Metasurfaces Using Heterojunction Resonators”. In: *Advanced Optical Materials* 4 (2016), pp. 1582–1588. DOI: DOI:10.1002/adom.201600297.

[33] Fei Ding et al. “Broadband High-Efficiency Half-Wave Plate: A Supercell-Based Plasmonic Metasurface Approach”. In: *ACS Nano* 9.4 (2015), pp. 4111–4119. DOI: 10.1021/acsnano.5b00218.

[34] Amir Arbabi et al. “Dielectric metasurfaces for complete control of phase and polarization with subwavelength spatial resolution and high transmission”. In: *Nature Nanotechnology* 10.937 (2015). DOI: http://dx.doi.org/10.1038/nnano.2015.186.

[35] ANDERS PORS, MICHAEL G. NIELSEN, and SERGEY I. BOZHEVOLNYI. “Plasmonic metagratings for simultaneous determination of Stokes parameters”. In: *Optica* 2.8 (2015), pp. 716–723. DOI: http://dx.doi.org/10.1364/OPTICA.2.000716.

[36] Dirk Taillaert et al. “Grating Couplers for Coupling between Optical Fibers and Nanophotonic Waveguides”. In: *Japanese Journal of Applied Physics* 45.8A (2006), pp. 6071–6077. DOI: http://dx.doi.org/10.1143/JJAP.45.6071.

[37] Connie J. Chang-Hasnain and Weijian Yang. “High-contrast gratings for integrated optoelectronics”. In: *Advances in Optics and Photonics* 4 (2012), pp. 379–440. DOI: 10.1364/AOP.4.000379.

[38] Bo Han Chen et al. "GaN Metalens for Pixel-Level Full-Color Routing at Visible Light". In: *Nano Letters* 17.10 (2017), pp. 6345–6352. DOI: 10.1021/acs.nanolett.7b03135. URL: https://pubs.acs.org/doi/abs/10.1021/acs.nanolett.7b03135.

[39] Patrice Genevet and Federico Capasso. "Holographic optical metasurfaces: a review of current progress". In: *Reports on Progress in Physics* 78 (2015). DOI: 10.1088/0034-4885/78/2/024401. URL: http://dx.doi.org/10.1088/0034-4885/78/2/024401.

[40] Haoran Ren et al. "Metasurface orbital angular momentum holography". In: *Nature Communications* 10.2986 (2019). DOI: 10.1038/s41467-019-11030-1.

[41] Dasol Lee et al. "Resolution enhancement of fluorescence microscopy using encoded patterns from all-dielectric metasurfaces". In: *Applied Physics Letters* 115 (2019). DOI: 10.1063/1.5119006. URL: https://aip.scitation.org/doi/10.1063/1.5119006.

[42] Wei Ting Chen et al. "A broadband achromatic polarization-insensitive metalens consisting of anisotropic nanostructures". In: *Nature Communications* 10 (2019). DOI: https://doi.org/10.1038/s41467-019-08305-y.

[43] M. Khorasaninejad et al. "Visible Wavelength Planar Metalenses Based on Titanium Dioxide". In: *IEEE Journal of Selected Topics in Quantum Electronics* 23 (2016).

[44] Liang Y et al. "High-Efficiency, Near-Diffraction Limited, Dielectric Metasurface Lenses Based on Crystalline Titanium Dioxide at Visible Wavelengths". In: *Nanomaterials* 8 (2018).

[45] Maxwell D. Aiello et al. "Achromatic varifocal metalens for the visible spectrum". In: *ACS Photonics* (2019). DOI: 10.1021/acsphotonics.9b00523. URL: https://pubs.acs.org/doi/10.1021/acsphotonics.9b00523.

[46] Wei Ting Chen et al. "Immersion Meta-Lenses at Visible Wavelengths for Nanoscale Imaging". In: *Nano Letters* 17.5 (2017), pp. 3188–3194. DOI: 10.1021/acs.nanolett.7b00717. URL: http://dx.doi.org/10.1021/acs.nanolett.7b00717.

[47] David Fattal et al. "Flat Dielectric Grating Reflectors with High Focusing Power". In: *Nature Photonics* 4 (2010), pp. 466–470. URL: https://www.nature.com/articles/nphoton.2010.116.

[48] Anders Pors et al. "Broadband Focusing Flat Mirrors Based on Plasmonic Gradient Metasurfaces". In: *NANO Letters* 13.2 (2013), pp. 829–834. DOI: 10.1021/nl304761m. URL: https://doi.org/10.1021/nl304761m.

[49] Amir Arbabi et al. "Efficient dielectric metasurface collimating lenses for mid-infrared quantum cascade lasers". In: *Optics Express* 23.26 (2015), pp. 33310–33317. DOI: 10.1364/OE.23.033310. URL: https://doi.org/10.1364/OE.23.033310.

[50] Dianmin Lin et al. "Optical metasurfaces for high angle steering at visible wavelengths". In: *Scientific Reports* 7.2286 (2017). DOI: 10.1038/s41598-017-02167-4.

[51] Philippe Lalanne et al. "Design and fabrication of blazed binary diffractive elements with sampling periods smaller than the structural cutoff". In: *Journal of the Optical Society of America* 16 (1999), pp. 1143–1156.

[52] U YANG et al. "High-efficiency all-dielectric transmission metasurface for linearly polarized light in the visible region". In: *Photonics Research* 6.6 (2018), pp. 517–524. URL: https://doi.org/10.1364/PRJ.6.000517.

[53] Shang Sun et al. "All-Dielectric Full-Color Printing with TiO2 Metasurfaces". In: *ACS Nano* 11 (2017), pp. 4445–4452.

[54] Philippe Lalanne and Pierre Chavel. "Metalenses at visible wavelengths: past, present,perspectives". In: *Laser and Photonics Reviews* 1600295 (2017). DOI: 10.1002/lpor.201600295.

[55] Nanfang Yu et al. "Light Propagation with Phase Discontinuities: Generalized Laws of Reflection and Refraction". In: *Science* 334.6054 (2011), pp. 333–337. DOI: 10.1126/science.1210713.

[56] David Sell et al. "Ultra-High-Efficiency Anomalous Refraction with Dielectric Metasurfaces". In: *ACS Photonics* 5 (2018), pp. 2402–2407. DOI: 10.1021/acsphotonics.8b00183. URL: http://dx.doi.org/10.1021/acsphotonics.8b00183.

[57] David Sell et al. "Large-Angle, Multifunctional Metagratings Based on Freeform Multimode Geometries". In: *Nano Letters* 17 (2017), pp. 3752–3757. DOI: http://dx.doi.org/10.1021/acs.nanolett.7b01082.

[58] Simion Astilean et al. "High-efficiency subwavelength diffractive element patterned in a high-refractive-index material for 633 nm". In: *Optics Letters* 23 (1998), pp. 552–554.

[59] Alexander V. Kildishev, Alexandra Boltasseva, and Vladimir M. Shalaev. "Planar Photonics with Metasurfaces". In: *Science* 339 (2013), p. 1232009. DOI: 10.1126/science.1232009.

[60] Manuel Decker et al. "High-Efficiency Dielectric Huygens' Surfaces". In: *Advanced Optical Materials* 3.6 (2015). DOI: 10.1002/adom.201400584. URL: https://onlinelibrary.wiley.com/doi/abs/10.1002/adom.201400584.

[61] Zhongyi Guo et al. "Dielectric metasurface based high-efficiency polarization splitters". In: *RSC Advances* 7 (2019), pp. 9872–9879. DOI: 10.1039/c6ra27741a.

[62] Robert C. Devlin et al. "High efficiency dielectric metasurfaces at visible wavelengths". In: *PNAS* 113.38 (2016), pp. 10473–10478. DOI: 10.1073/pnas.1611740113. URL: https://www.pnas.org/content/113/38/10473.

[63] Philippe Lalanne and Dominique Lemercier-lalanne. "On the effective medium theory of subwavelength periodic structures". In: *Journal of Modern Optics* 43 (1996), pp. 2063–2085.

[64] Philippe Lalanne and Dominique Lemercier-lalanne. "Depth dependence of the effective properties of subwavelength gratings". In: *Journal of Modern Optics* 14 (1997), pp. 450–458.

[65] Takayuki Matsui et al. “Experimental investigation of double-groove grating satisfying total internal reflection condition”. In: *Opt. Express* 22.21 (Oct. 2014), pp. 25362–25370. DOI: 10.1364/OE.22.025362. URL: http://www.opticsexpress.org/abstract.cfm?URI=oe-22-21-25362.

[66] Raphaël Pestourie et al. “Inverse design of large-area metasurfaces”. In: *Optic Express* 26.26 (2018). DOI: https://doi.org/10.1364/OE.26.033732.

[67] Federico Capasso. “The future and promise of flat optics: a personal perspective”. In: *Nanophotonics* (2018). DOI: http://orcid.org/0000-0003-4534-8249.

[68] et al M.G. Moharam. In: *JOSAA 12* 1068 (1995).

[69] M.G. Moharam et al. In: *JOSAA 12* 1077 (1995).

[70] P. Lalanne and G.M. Morris. In: *JOSAA 13* 779 (1996).

[71] G. Granet and B. Guizal. In: *JOSAA 13* 1019 (1996).

[72] L. Li. In: *JOSAA 13* 1870 (1996).

[73] Takayuki Matsui. In: *JOSAA 14* 2758-2767 (1997).

[74] E. Popov and M. Nevière. In: *JOSAA 17* 1773 (2000).

[75] N Donkov et al. “Biocompatibility of dielectric Ta2O5 coatings in in vitro tests”. In: vol. 223. 2010. URL: https://iopscience.iop.org/article/10.1088/1742-6596/223/1/012030/meta.

[76] D. L. Wood et al. “Optical properties of cubic hafnia stabilized with yttria”. In: *Applied Optics* 29.4 (1990), pp. 604–607. URL: https://www.osapublishing.org/ao/abstract.cfm?uri=ao-29-4-604.

[77] D. L. Wood and K. Nassau. “Refractive index of cubic zirconia stabilized with yttria”. In: *Applied Optics* 21.16 (1982), pp. 2978–2981.

[78] A. S. Barker, Jr., and M. Ilegems. “Infrared Lattice Vibrations and Free-Electron Dispersion in GaN”. In: *Physical Review B* 7.2 (1973), pp. 743–750.

[79] Akihiro Matsutani et al. “SF6-Based Deep Reactive Ion Etching of (001) Rutile TiO2 Substrate for Photonic Crystal Structure with Wide Complete Photonic Band Gap”. In: *Japanese Journal of Applied Physics* 51 (2012).

[80] Hao Yang et al. “The design and optimization of high-contrast all-dielectric metastructures for visible-range applications”. In: *High Contrast Metastructures VIII SPIE OPTO*. 10928. 2019.

[81] S.Norasetthekul et al. “Dry etch chemistries for TiO2 thin films”. In: *Applied Surface Science* 185 (2001), pp. 27–33.

[82] Kyung-Rok Choi et al. “Dry etching properties of TiO_2 thin films in $O_2/CF_4/Ar$ plasma”. In: *Vacuum* 91 (2012), pp. 85–89. DOI: http://dx.doi.org/10.1016/j.vacuum.2012.11.009.

[83] Kyung-Rok Choi et al. “The Dry Etching Characteristics of TiO2 Thin Films in $N_2/CF_4/Ar$ Plasma”. In: *Transactions on Electrical and Electronic Materials* 15.1 (2014), pp. 32–36. DOI: http://dx.doi.org/10.4313/TEEM.2014.15.1.32.

[84] Jong-Chang Woo, Young-Hee Joo, and Chang-Il Kim. “Etch Characterization of TiO_2 Thin Films Using Metal-Insulator-Metal Capacitor in Adaptively Coupled Plasma”. In: *Japanese Journal of Applied Physics* 50.8 (2011), 08KC02. DOI: 10.1143/jjap.50.08kc02.

[85] Ahmed N. Noemaun et al. "Inductively coupled plasma etching of graded-refractive-index layers of TiO_2 and SiO_2 using an ITO hard mask". In: *Journal of Vacuum Science and Technology A* 29 (2011). DOI: 10.1116/1.3620494.

[86] Junghoon Yeom et al. "Maximum achievable aspect ratio in deep reactive ion etching of silicon due to aspect ratio dependent transport and the microloading effect". In: *Journal of Vacuum Science and Technology B* 23 (2005), pp. 2319–2329. DOI: https://doi.org/10.1116/1.2101678. URL: https://avs.scitation.org/doi/abs/10.1116/1.2101678.

[87] S. L. Lai, D. Johnson, and R. Westerman. "Aspect ratio dependent etching lag reduction in deep silicon etch processes". In: *Journal of Vacuum Science and Technology A* 24.4 (2006), p. 1283. DOI: 10.1116/1.2172944.

[88] Chad M. Huard et al. "Role of neutral transport in aspect ratio dependent plasma etching of three-dimensional features". In: *Journal of Vacuum Science and Technology A* 35.5 (2017). DOI: http://dx.doi.org/10.1116/1.4973953.

[89] Jack R Franco, Janos Havas, and Harold A Levine. *Method of depositing thin film utilizing a lift-off mask*. US Patent US3873361A. 1973. URL: https://patents.google.com/patent/US3873361A/en.

[90] Alexei L. Bogdanov and Eva Karin Andersson. "Fine undercut control in bilayer PMMA-P(MMA-MAA) resist system for e-beam lithography with submicrometer resolution". In: *Electron-Beam, X-Ray, and Ion-Beam Submicrometer Lithographies for Manufacturing*. 1465. 1991.

[91] R. Hsiao. "Fabrication of magnetic recording heads and dry etching of head materials". In: *IBM Journal of Research and Development* 43.1 (1999), pp. 89–102.

[92] Isao Nakatani. "Ultramicro Fabrications on Fe-Ni Alloys Using Electron-Beam Writing and Reactive-Ion Etching". In: *IEEE Transactions on Magnetics* 32.5 (1996), pp. 4448–4451.

[93] Zhiwei Zhao, Beng Kang Tay, and Guoqing Yu. "Roomtemperature deposition of amorphous titanium dioxide thin film with high refractive index by a filtered cathodic vacuum arc technique". In: *The Optical Society* 43.6 (2004), pp. 1281–1285.

[94] Christophe Cardinaud. "Fluorine-based plasmas: Main features and application in micro-and nanotechnology and in surface treatment". In: *Comptes Rendus Chimie* 21.8 (2018), pp. 723–739. DOI: 10.1016/j.crci.2018.01.009. URL: https://doi.org/10.1016/j.crci.2018.01.009.

[95] Badih El-Kareh and Lou N. Hutter. *Fundamentals of Semiconductor Processing Technology*. 1994, p. 228.

[96] Bushberg J. T. et al. *The Essential Physics of Medical Imaging*. Lippincott Williams & Wilkins, 2003.

[97] Guoan Zheng, Roarke Horstmeyer, and Changhuei Yang. "Wide-field, high-resolution Fourier ptychographic microscopy". In: *Nature Photonics* 7.9 (2013), pp. 739–745. ISSN: 1749-4893. DOI: 10.1038/nphoton.2013.187. URL: https://doi.org/10.1038/nphoton.2013.187.

[98] Thaibao Phan et al. "High-efficiency, large-area, topology optimized metasurfaces". In: *Light: Science and Applications* 8.48 (2019). DOI: 10.1038/s41377-019-0159-5. URL: https://doi.org/10.1038/s41377-019-0159-5.

[99] Dianjing Liu et al. "Training deep neural networks for the inverse design of nanophotonic structures". In: *ACS Photonics* 5.4 (2018), pp. 1365–1369. DOI: 10.1021/acsphotonics.7b01377. URL: https://doi.org/10.1021/acsphotonics.7b01377.

[100] Zhaocheng Liu et al. "Generative Model for the Inverse Design of Metasurfaces". In: *Nano Letters* 18.10 (2018), pp. 6570–6576. DOI: 10.1021/acs.nanolett.8b03171. URL: https://doi.org/10.1021/acs.nanolett.8b03171.

[101] Sandeep Inampudi and Hossein Mosallaei. "Neural network based design of metagratings". In: *Applied Physics Letters* 112.241102 (2018). DOI: 10.1063/1.5033327. URL: https://doi.org/10.1063/1.5033327.

[102] Mahmoud M R Elsawy et al. "Global optimization of metasurface designs using statistical learning methods". working paper or preprint. July 2019. URL: https://hal.archives-ouvertes.fr/hal-02156881.

[103] Wilson JD, Cottrell WJ, and Foster TH. "Index-of-refraction-dependent subcellular light scattering observed with organelle-specific dyes". In: *Journal of Biomedical Optics* 12.1 (2007). DOI: 10.1117/1.2437765. URL: https://www.ncbi.nlm.nih.gov/pubmed/17343485.

[104] P. Y. Liu et al. "Cell refractive index for cell biology and disease diagnosis: past, present and future". In: *Lab on a Chip* 4 (2016). URL: https://pubs.rsc.org/en/content/articlelanding/2016/lc/c5lc01445j#!divAbstract.

[105] Weixing Li et al. "Ultra-stable and versatile widefield cryo-fluorescence microscope for single-molecule localization with sub-nanometer accuracy". In: *Optical Society of America* 23.3 (2014), pp. 3770–3783. DOI: 10.1364/OE.23.003770.

[106] Graham J. Triggs et al. "Chirped guided-mode resonance biosensor". In: *Optica* 4.2 (Feb. 2017), pp. 229–234. DOI: 10.1364/OPTICA.4.000229. URL: http://www.osapublishing.org/optica/abstract.cfm?URI=optica-4-2-229.

[107] Dasol Lee et al. "All-dielectric metasurface imaging platform applicable to laser scanning microscopy with enhanced axial resolution and wavelength selection". In: *Opt. Mater. Express* 9.8 (Aug. 2019), pp. 3248–3259. DOI: 10.1364/OME.9.003248. URL: http://www.osapublishing.org/ome/abstract.cfm?URI=ome-9-8-3248.

[108] Ehsan Arbabi et al. "Two-Photon Microscopy with a Double-Wavelength Metasurface Objective Lens". In: *Nano Letters* 18.8 (2018). PMID: 30016110, pp. 4943–4948. DOI: 10.1021/acs.nanolett.8b01737. eprint: https://doi.org/10.1021/acs.nanolett.8b01737. URL: https://doi.org/10.1021/acs.nanolett.8b01737.

[109] Mikael P. Backlund et al. "Removing orientation-induced localization biases in single-molecule microscopy using a broadband metasurface mask". In: *Nature Photonics* 10 (May 2016), pp. 459–462. URL: https://doi.org/10.1038/nphoton.2016.93.

[110] Philippe Lalanne et al. "Blazed binary subwavelength gratings with efficiencies larger than those of conventional échelette gratings". In: *Opt. Lett.* 23.14 (July 1998), pp. 1081–1083. DOI: 10.1364/OL.23.001081. URL: http://ol.osa.org/abstract.cfm?URI=ol-23-14-1081.

Appendices

.1 Lift-off technique

Two small beakers with TCE are warmed up to 70-80 degrees on a hot plate, while a third beaker is prepared with IP alcohol and left at room temperature. The metalized sample ready of lift-off is submerged and left in the first TCE bath for 5 minutes. If there is good separation of the different levels of the hard-mask layer, 5 minutes is long enough for the solvent to creep in between the gaps and dissolve the soft mask resist, causing a visible rugosity of the metallic layer, with a bubbling effect. If this is not the case, our experience would signal problems with the soft-mask profile (see Section 3.3 and Figure 3.3). At this point, both TCE beakers are placed in an stopped ultrasonic bath, configured to low power and 80 kHz. We then use a pair of tweezers to gently put and hold the sample on its side, with the MS vertically on the beaker, turn on the ultrasonic bath and immediately transfer the sample into the second TCE beaker while keeping the surface under a soft jet of TCE with a wash bottle to finally turn the bath off. The goal of this key step is to avoid the recurrent problem had when the sample was placed horizontally on the bottom of the beaker, where the lifted-off metal strings entangled between them and with the irregular surface of the metasurface, deteriorating the quality of the mask. The short sonication, lasting just a few seconds, helps to mechanically separate the hard-mask residue from the surface just before the sample is transferred into clean TCE. The second TCE bath provides time for a visual inspection of the hard mask before moving the sample to the final IPA bath to be quick and easily dried up afterwards. A proper Nickel lift-off of these metasurface patterns results in a distinctively semitransparent, homogeneous, dark rectangle.

.2 First generation process: Single layer Lift-Off

1. Thorough cleaning of the borosilicate glass coverslips that will act as the substrate for the device. This is achieved using a 3-minutes sonication on isopropyl alcohol followed by a 10 minutes immersion in Piranha solution. This combination of mechanical and chemical cleaning was effective enough to avoid potential fluorescent contamination to be embedded in the structures.

2. Once the glass substrate is clean a 230nm-thick layer of amorphous titanium dioxide (TiO_2) is deposited on the surface with a Plassys MEB 800 ion-assisted electron beam evaporator (Source material: Ti_3O_5, rate 1-2 Å/s).

3. A 100nm-thick layer of A3 Polymethyl methacrylate resist (PMMA) is spin-coated during 30 seconds at 5000RPM (Acc. 2000RPM/s) and followed by a 30-minute baking at 160° C.

4. A reflective layer required for the EBPG 5000+ electron beam lithography's focusing system is fabricated with a 20nm-thick deposition of aluminium using a Plassys MEB 550SL e-gun evaporator. This layer is also responsible of evacuating the incoming electrons to avoid charge-related issues (lack of resolution, distortion, etc).

5. The metasurface design is transfer into the PMMA resist with a EBPG 5000+ electron beam lithography system. Depending on the specific design a dose is

chosen in the range 300-500µC/cm^2. Proximity dose corrections may be necessary, specially if there is a significant fraction of the total surface closer than 15µm from a border.

6. Once the PMMA resist has been exposed, the aluminium layer is no longer necessary and it is removed with a 1-minute immersion in NaOH solution (20gr/l).

7. The development of the exposed PMMA is done with a 50-second immersion in a solution composed of 1 part of Methyl isobutyl ketone (MIBK) and 3 parts of Isopropyl alcohol (IPA) at 20° C, immediately followed by a 10-second rinse in IPA. Very gentle movements avoiding rotations can be applied to facilitate the process. Finally the surface is dried up with a low-pressure nitrogen spray gun.

8. A resist stripping of surface is performed. For this step two options were tested with a low-power, oxygen plasma offering generally better results than a Ar-Ion Beam Etching.

9. A Nickel layer is deposited with an e-beam evaporation system (Plassys MEB 550SL). The thickness of this layer has to suffice to etch the desired TiO_2 thickness, which in our case translated to 20nm of Ni. This is also dependent on the etching process which is going to be used afterwards, and there is a direct benefit on being able to use a thinner hard mask.

10. Lift-off: Possibly the less repeatable step of the process and highly susceptible to the individual technique of the person doing it. Our technique evolved along this project but best results were achieved using an initial static Trichloroethylene (TCE) bath at 85° C to dissolve the exposed resist (5min) followed by a short (1-3s) medium-power sonication while the sample is being extracted from the TCE bath into a new TCE bath leaving all the residual metal-layer fragments behind. Even if this transition only takes a few seconds, it was performed with the sample under a continuous soft jet of TCE in order to keep the surface wet at all times and avoid any metal fragment sticking into it. If this step was performed successfully, the metasurface hard mask will have a translucent and homogeneous appearance, in which case the sample can be rinsed with IPA and dried with nitrogen.

11. Any residues adhered to the surface could mask and transfer its shape into the TiO_2. To eliminate organic residues a 3-min oxygen plasma cleaning of the hard mask is performed right before the TiO_2 etching in the same reactor (with the sample remaining under after the cleaning).

12. Finally the TiO_2 is etched with a capacitively coupled plasma reactive ion etching system (Nextral-Unaxis NE100) and a mixture of SF_6 and CHF_3. The pressure, plasma power and exact gas-ratio will define the type of etching achieved. The etching depth is tracked in real-time trough laser interferometry.

13. The final step consists on removing the remaining nickel with a 1-min immersion in nitric acid (HNO_3) 26% in water.

.3 Third generation process: Etched Aluminum hard mask

1. Thorough cleaning of the borosilicate glass coverslips that will act as the substrate for the device. This is achieved using a 3-minutes sonication on isopropyl alcohol followed by a 10 minutes immersion in piranha solution.

2. Once the glass substrate is clean a 230nm-thick layer of amorphous titanium dioxide (TiO_2) is deposited on the surface with a Plassys MEB 800 ion-assisted electron beam evaporator (Source material: Ti_3O_5, rate 1-2 Å/s).

3. An aluminium layer is deposited using a Plassys MEB 550SL e-gun evaporator. The thickness of this layer ranged between 20 nm and 40 nm depending on the structure size and TiO_2 etching ICP-RIE process. This layer, that will be turned into the hard mask for the TiO_2, is also reflective and conductive enough for the sample to be focused and discharged during the electron beam exposure.

4. Any possible moisture on the surface is removed after 5-min in an oven at ∼160° C.

5. A 100nm-thick layer of ZEP-520A resist (ZEONREX Electronic Chemicals) is spin-coated during 30 seconds at 4000RPM (Acc. 2000RPM/s) and followed by a 2-minute baking at 160° C.

6. The metasurface design is transfer into the ZEP-520A resist with a EBPG 5000+ electron beam lithography system. Depending on the specific design a dose is chosen in the range 160-200µC/cm^2.

7. The exposed ZEP-520A is developed for 45 seconds in ZED-N50 (also manufactured by ZEONREX Electronic Chemicals), rinsed in IPA for 30 seconds and finally dried up low-pressure nitrogen spray gun.

8. The aluminium layer is etched on an TPSA-ICP RIE reactor using a chlorine-based dry etching process (HBr/BCl_3 40/60 ICP Power 150W, 100V DC Polarization, Pressure 1-2mTorr).

9. The TiO_2 layer is etched with an CCP RIE system (Nextral-Unaxis NE100) and a SF_6/CHF_3 chemistry.

10. Any aluminium mask remaining (and eventually ZEP-520A) is removed with a 1-minute immersion in NaOH solution (20gr/l).

.4 Fourth generation process: Direct soft mask etching

1. Substrate cleaning with 3-minutes sonication on isopropyl alcohol followed by a 10 minutes immersion in piranha solution.

2. Amorphous titanium dioxide (TiO_2) deposition on the surface with a Plassys MEB 800 ion-assisted electron beam evaporator (Thickness h= 230nm, source material: Ti_3O_5, rate 1-2 Å/s).

3. A 140nm-thick layer of ZEP-520A resist (ZEONREX Electronic Chemicals) is spin-coated during 30 seconds at 3000RPM (Acc. 2000RPM/s) and followed by a 2-minute baking at 160° C.

4. An aluminium layer is deposited using a Plassys MEB 550SL e-gun evaporator for discharge and focusing during the e-beam exposure.

5. Electron beam exposure on a EBPG 5000+ system. Dose in the range 160-200 $\mu C/cm^2$ depending on the specific design.

6. The aluminum layer is removed with a 1-minute immersion in NaOH solution (20gr/l) and the underlying ZEP-520A is developed for 45 seconds in ZED-N50, rinsed in IPA for 30 seconds and finally dried up low-pressure nitrogen spray gun.

7. The TiO_2 layer is etched with an ICP-RIE system and a chlorine based recipe. The remaining ZEP-520A is removed with ZDMAC (ZEONREX Electronic Chemicals).

.5 Stem Cells preparation

The sample preparation consisted on the hMSC-bm cells (Lonza Ref. #PT-2501) grown in T75 cell culture flasks (Corning Inc., New York,NJ, USA, 43061) in Dulbecco's Modified Eagle Medium (DMEM Gibco, Thermo Fisher Scientific Inc., Waltham, MA, USA, A18967-01) supplemented with 10% fetal bovine serum (Sigma-Aldrich Co., St. Louis, MO, USA, F2442-500ML) and 1% antibiotics (penicillin/streptomycin, Life Technologies, Thermo Fisher Scientific Inc., Waltham,MA, USA, 15140- 122) at 37°C and 5% CO2 passaged every 2-3 days, with passage #5 was used for this experiment.

Cells were seeded on 25 mm glass coverslips at a density of 10.000 hMSCs per glass in 6- well plates (Sarstedt AG & Co., Nuembrecht, Germany, 83.3920) with 2mL growth medium per well and grown at 37°C and 5% CO2. Cells were chemically fixed 24 h after seeding in a 10% formaldehyde (Sigma- Aldrich Co., St. Louis, MO, USA, 47608-250ML-F) in PBS for 10 min. Subsequently, cells were permeabilized using 0.5% Triton X 100 (Carl Roth GmbH & Co. KG, Karlsruhe, Germany, 6683.1) in PBS for 10 min and blocked with 3% BSA (Sigma-Aldrich Co., St. Louis, MO, USA, A9418-100G) in PBS for 30 min, incubated again with Triton X for 5 min and thoroughly washed with PBS. All antibodies were kept in a 3% BSA PBS solution. Immunostaining was performed either with anti-Paxillin (Abcam, ab32084) [1:400] for 10 h, then anti-rabbit IgG Atto 647N (Sigma-Aldrich Co., St. Louis, MO, USA, 40839) [1:400] for 2 h or with Phalloidin Atto 647N (ATTO-TEC GmbH, Siegen, Germany, AD647N-82) [1:150] for 2 h. Finally, the samples were covered with 24 mm glass coverslips using Fluoroshield mounting medium (Sigma- Aldrich Co., St. Louis, MO, USA, F6182-20ML).

5.6 Résumé en Français

5.6.1 Introduction

Au cours des trois dernières décennies, la microscopie à fluorescence par réflexion interne totale (TIRF) a été la technique la plus répandue parmi les techniques de microscopie optique à haute résolution axiale disponibles dans le commerce, en raison de sa relative simplicité et de ses performances pratiquement inégalées pour l'étude de la membrane cellulaire. Les systèmes TIRF, basés en grande partie sur des objectifs à grande ouverture numérique (ou NA pour 'Numerical aperture' en anglais), reposent sur un champ évanescent qui atteint quelques centaines de nanomètres de profondeur dans la région d'intérêt, sans lumière dans la majeure partie de l'échantillon, ce qui améliore considérablement le contraste de l'image tout en minimisant le photoblanchiment et photodommage. Cette approche utilisant des objectifs présente plusieurs avantages par rapport aux précédents microscopes TIRF basés sur des prismes, mais amène également son propre ensemble de limitations, telles que la nécessité d'un contact physique direct avec l'échantillon, un faible champ de vision (FOV) ou le coût élevé de ces objectifs, parmi les plus coûteux de tous les objectifs de microscopie optique disponibles dans le commerce.

D'autre part, récemment il y a eu un développement florissant d'une nouvelle génération de composants optiques, qui devrait avoir un impact majeur sur un large éventail de systèmes optiques de nouvelle génération: les métasurfaces (MS), l'équivalent bidimensionnel des métamatériaux, sont généralement constitués de réseaux de nanorésonateurs périodiques ou quasi-périodiques conçus pour conférer un changement de phase hautement localisé et arbitraire à chaque point de la MS, ce qui permet une personnalisation complète du profil de front d'onde transmis ou réfléchi. Contrairement aux composants optiques réfractifs traditionnels, où les modifications de la lumière s'accumulent progressivement sur des distances relativement grandes, les MSs offrent une modification abrupte des propriétés du faisceau, généralement dans une distance inférieure à une longueur d'onde. Cette caractéristique unique, associée à la possibilité d'obtenir des comportements non conventionnels qui n'existaient jamais sur les composants optiques traditionnels, s'est révélée utile pour une vaste gamme d'applications allant de la spectroscopie[35] à l'optique intégrée[36], le filtrage optique[37], les capteurs d'image[38], l'holographie [39, 40] et les détecteurs biologiques[106].

En particulier dans le contexte de la microscopie optique, les MSs modernes adaptées au spectre visible auront très certainement un impact majeur, malgré l'absence relative de travaux actuellement destinés à cette application. En dehors des progrès impressionnants en cours dans le développement des complexes métalentilles achromatiques, dont le champ d'application va bien au-delà de la microscopie, il n'y a pas beaucoup de développements qui peuvent être mentionnés. Certaines exceptions récentes notables sont l'utilisation des MSs pour améliorer la résolution axiale sur la microscopie à balayage laser [107], des métalentilles pour la microscopie à deux photons [108] et la suppression du biais de localisation induit par l'orientation sur la microscopie en molécule unique[109].

Le pilotage de faisceau a été l'un des premiers objectifs poursuivis dans tous les développements des MSs, généralement en tant qu'étape intermédiaire nécessaire pour

cibler ultérieurement des réponses plus complexes (par exemple, la focalisation), certaines des premières réalisations expérimentales remontant à 1998 [110]. Alors que l'efficacité et la complexité de ces systèmes de direction de faisceau ont considérablement augmenté, avec l'avènement d'outils de conception plus avancés (par exemple, les algorithmes de conception inverses, les technologies de [57, 56, 102]) et la nanofabrication , la mise en œuvre complète de la technique de microscopie TIRF basée sur MS n'a jamais été réalisée ni proposée.

Le dispositif TIRF conçu dans ce projet consiste en un substrat spécial ne nécessitant pas d'objectif particulier à NA élevé pour obtenir la réflexion interne totale et le champ évanescent d'excitation. Au lieu de cela, un réseau MS conçu à dessein redirige la majeure partie de l'énergie laser entrant dans l'espace libre vers l'un des premiers ordres de diffraction, agissant comme un coupleur de lumière pour une grande microscopie FOV TIRF peu coûteuse. Nous démontrons expérimentalement que ces MS peuvent coupler jusqu'à 70% de la lumière transmise dans le premier ordre de diffraction à un angle de 65° à l'intérieur du substrat de verre, ce qui suffit aux conditions de réflexion interne totale pour une interface verre-eau. Nous avons finalement utilisé ces MS pour obtenir une image de cellules souches mésenchymateuses humaines de grande taille 200µm immunocolorées, généralement très larges pour être visualisées dans un seul cadre TIRF basé sur un objectif.

5.6.2 Conception de métasurfaces

Afin de concevoir un dispositif utilisant uniquement des matériaux biocompatibles, transparents dans le visible, tout en maximisant le contraste de l'indice de réfraction entre la MS et son support, nous avons choisi TiO_2 comme matériau de la structure et le verre borosilicate comme substrat.

Pour la conception de la métasurface, nous avons utilisé le logiciel RETICOLO de J.P. Hugonin et P. Lalanne pour calculer les efficacités de diffraction et les amplitudes de réseaux superposés en 2D à l'aide de la méthode modale du domaine fréquentiel appelée 'Rigorous coupled-wave analysis' (RCWA). En partant d'une structure 1D 'double groove' (similaire à celles de [65] et de [50]) et en utilisant un algorithme du gradient modifié sur des centaines d'ensembles de 9 paramètres dimensionnels initiaux aléatoires définissant une structure générique, convergé vers le modèle présenté dans la Figure 5.12 (a) et (b). À cette fin, nous avons défini et utilisé un facteur de mérite consistant en un rapport entre l'efficacité de diffraction de l'un des premiers ordres (-1) et la somme des deux autres ordres (soit 0^{th} et 1^{st}), résultant en un agencement composite asymétrique de lignes continues et segmentées alternées. L'échantillon final est présenté à la Figure 5.12(d).

Les MSs ont été caractérisées à l'aide d'un objectif d'huile Olympus UApo N 100X 1.49 pour collecter tous les ordres de diffraction transmis de l'autre côté du substrat de verre de 170µm (la paire de premiers ordres à un angle de 65°aurait été reflétée en interne sans cette huile). Les trois faisceaux transmis sont donc focalisés par l'objectif sur son plan focal arrière (BFP), ce qui nous permet de mesurer leurs intensités par imagerie dudit plan sur un capteur CCD.

Lorsque la lumière externe polarisée TE à $\lambda_0 = 640nm$ atteint la MS, qui peut être

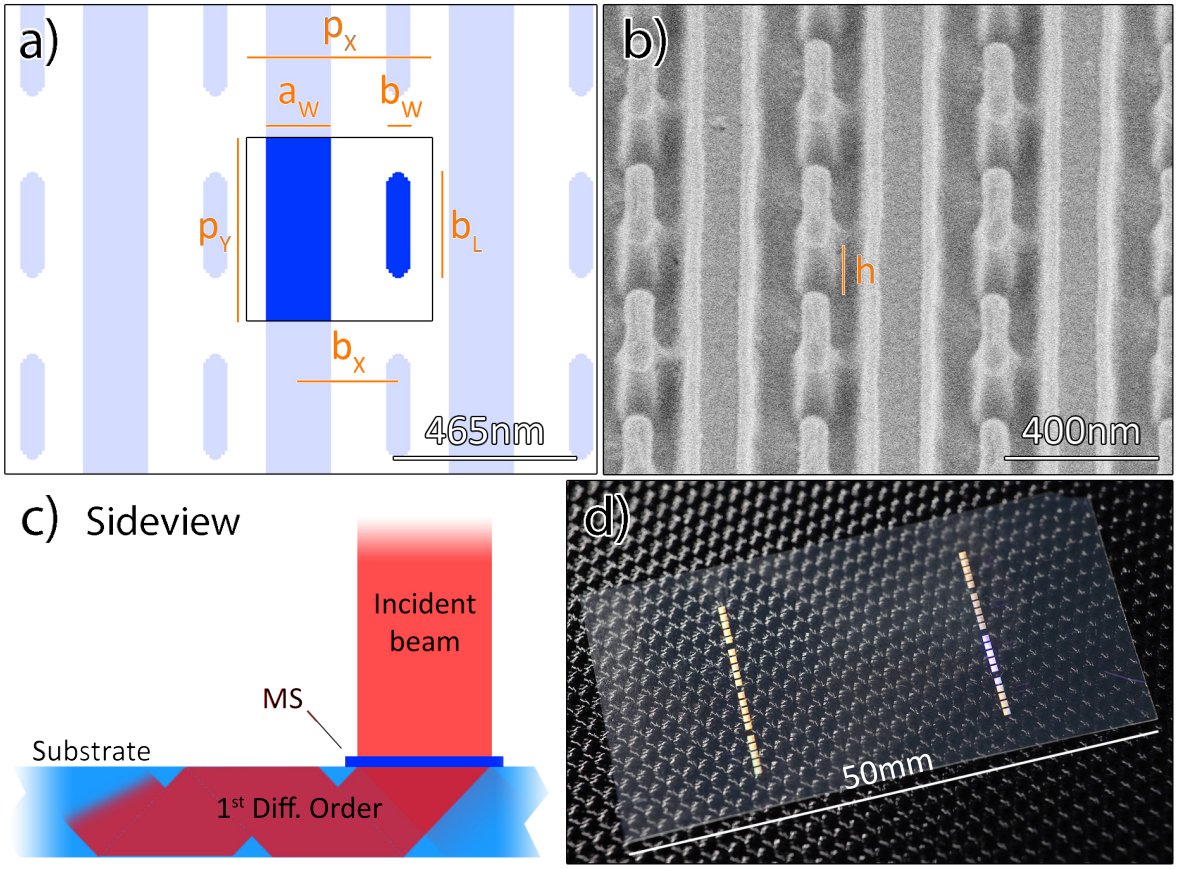

Figure 5.12 – (a) La géométrie horizontale de la conception de métasurface 2D choisie pour $\lambda_0 = 640nm$, avec $p_X = p_Y = 465nm = 0.73\lambda_0$, $a_W = 160nm$, $b_W = 61nm$, $b_X = 186nm$ et $b_L = 322nm$ et une hauteur $h = 230nm$ avec (b) une image au microscope électronique à balayage (MEB) (inclinaison de 45°) de l'échantillon fabriqué. (c) Lorsque la lumière polarisée par TE frappe la MS, jusqu'à 70% de la lumière transmise est couplée dans l'un des premiers ordres de diffraction vers le centre du substrat, 21% sont couplés dans le premier ordre opposé et seulement 9% dans l'ordre zéro traversant. (d) L'ensemble du substrat 25x50mm peut accueillir plusieurs MS, avec 40 visibles dans cet exemple.

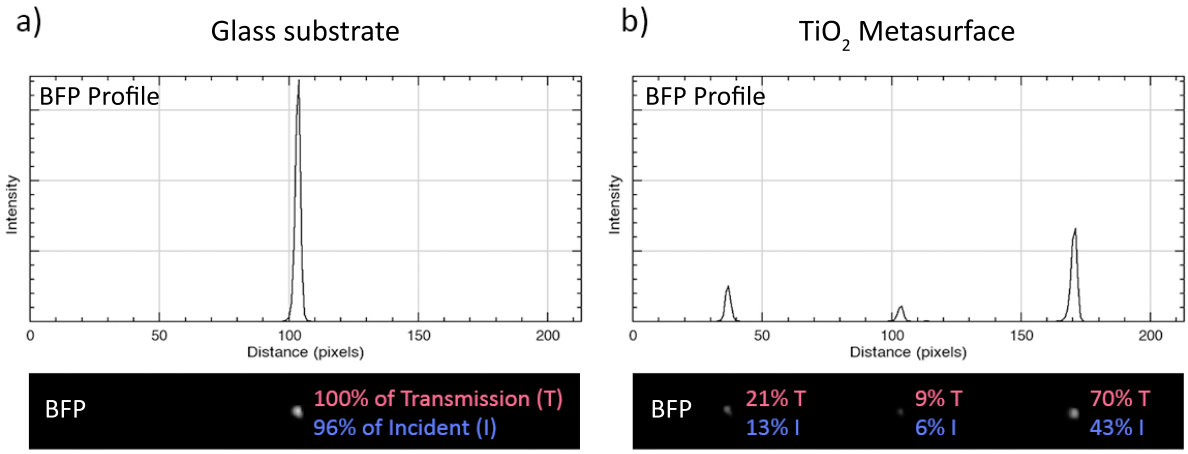

Figure 5.13 – Lorsqu'un faisceau incident polarisé TE atteint le (a) substrat en verre (référence) ou (b) la MS, les images du BFP capturées permettent de voir et de mesurer la distribution de la lumière transmise. En utilisant l'une de nos MS, jusqu'à 70% de la lumière transmise est couplée dans un ordre de diffraction, qui sort de la MS à un angle de 65° et est donc totalement réfléchie sur les côtés du substrat de microscopie.

située de part et d'autre du substrat en fonction de la configuration du microscope, nous mesurons 70% de la lumière transmise diffractée dans le premier ordre d'intérêt (de par sa conception celui qui est dirigé vers le centre du substrat), 21% couplés dans le premier ordre négligé et seulement 9% dans l'ordre de diffraction zéro (voir la figure 5.13). Bien que ce soient les valeurs les plus pertinentes pour notre application spécifique dans lesquelles la lumière réfléchie ou absorbée joue un rôle très limité, nous pouvons également mesurer chaque ordre de diffraction par rapport à l'intensité de l'incident (efficacité de diffraction absolue), auquel cas les valeurs obtenues sont respectivement 43%, 13% et 6% . Ces valeurs ressemblent beaucoup aux efficacités obtenues sur les simulations RCWA, à savoir 55%, 16% et 4%. Les 25% restants sont réfléchis par la MS. La transmission directe minimale de 4% est une caractéristique clé de toute conception de MS conçue pour la microscopie TIRF, en raison de la proximité éventuelle entre la MS et l'échantillon biologique et du fait que ce faisceau ne sera jamais couplé au substrat de verre, ce qui risque de détériorer le contraste de l'image si la lumière parasite atteignait l'échantillon observé.

5.6.3 Nanofabrication

Le processus de fabrication de nos métasurfaces est le suivant: Une couche épaisse de TiO_2 de 230nm est déposée (système de canon à faisceau électronique Plassys MEB 800 IAD) sur un substrat de 25x50mm de verre borosilicate. Deux résines positives à faisceau électronique (PMMA A2 et EL10 MMA) sont enduites par rotation afin de créer un empilement bicouche avec une section inférieure de sensibilité supérieure, métallisé avec 20nm d'aluminium et structuré à l'aide d'un graveur à faisceau électronique (Raith EBPG-5000+). Après développement dans du MIBK/IPA (1:3), les échantillons sont rincés à l'alcool IP et une couche de nickel est déposée (évaporateur à faisceau électronique Plassys MEB550SL). Un procédé de 'lift-off' est réalisé dans un bain de

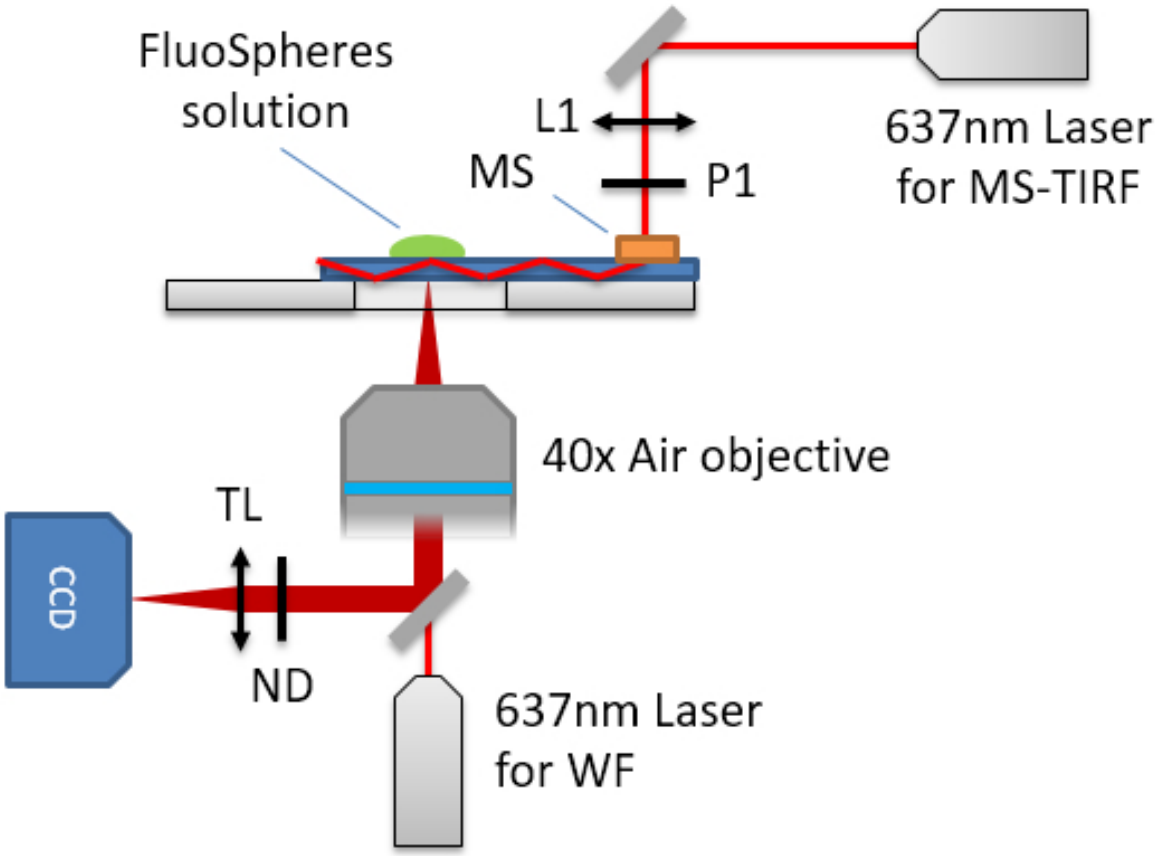

Figure 5.14 – La configuration utilisée permet d'éclairer l'échantillon de manière indépendante et arbitraire avec un champ à évanescence TIR ou une illumination WF avec deux lasers à onde continue de 637 nm. Un objectif à air Olympus UPlanSApo 40X NA0.95 et une caméra ANDOR iXon Ultra servent à enregistrer l'échantillon fluorescent monté sur une platine motorisée personnalisée. La lentille L1 focalise faiblement le faisceau entrant, polarisé linéairement par P1. La lentille TL focalise le plan de la MS dans le CCD.

trichloréthylène (85 °C) suivi par une gravure plasma du TiO_2 du type HBr/BCI_3 TPSA-ICP. Le Ni restant est finalement éliminé par une immersion dans de l'acide nitrique 26%.

5.6.4 Caractérisation

Cette configuration, visible dans la Figure 5.14, était basée sur une platine motorisée XY avec support de métasurface, un objectif pneumatique Olympus UPlanSApo 40X NA 0.95 monté sur une platine Z motorisée et une platine piézoélectrique (PIFOC, Physik Instrumente GmbH) permettant deux mouvements de diode laser à onde continue de 637nm pour l'éclairage unique ou simultané à grand champ (WF) ou TIR (OBIS Coherent 140 mW avec filtre de nettoyage laser ZET 640/10) et une caméra ANDOR iXon Ultra DU-897U-CS0-#BV avec capteur de 512 x 512 pixels (taille de pixel de 16 µm). Le faisceau atteignant la SM a été polarisé avec un cube séparateur de faisceau polarisant Thorlabs CM1-PBS251 et enfin légèrement focalisé avec un doublet achromatique Thorlabs AC254-300-A-ML de 300 mm.

L'étape suivante consistait à vérifier que nos métasurfaces pouvaient exciter sélectivement les fluorophores à proximité immédiate de la surface du substrat, tout en préservant le reste de l'échantillon dans l'obscurité, comme c'est le cas avec les techniques TIRF traditionnelles. À cette fin, une solution hautement diluée de particules fluorescentes (microsphères Invitrogen ™ FluoSpheres™, 0,2 µm 660/680 0,0001% en volume) a été préparée et utilisée pour un simple test TIRF qualitatif: Une gouttelette de solution (1-2 µl) a été déposée sur le centre de la lamelle, suivie du même volume d'eau pour la diluer davantage, puis laissée à sécher en fixant des particules fluorescentes sur la surface. Ensuite, une seconde gouttelette plus grosse (5-10 µl) de la solution a été déposée, donnant lieu à un état de fixation de certaines particules à la surface et à un nombre beaucoup plus important de particules diffusant dans l'eau, certaines heurtant parfois occasionnellement la surface. Enfin, une série d'images continues a été obtenue en alternant l'éclairage en WF, l'éclairage MS-TIRF ou les deux.

Les figures 5.15 (c) et (d) montrent deux images d'une série de 200 images, chacune avec un temps d'intégration de 100 ms, pour une vidéo résultante de 20 secondes. Avec 10 secondes d'éclairage WF, suivies de 10 secondes d'éclairage MS-TIRF, nous avons observé une nette distinction entre une activité de diffusion rapide brillante et effervescente des microsphères dans le volume de la solution, suivie d'une image presque statique de ces particules fixées à la surface, avec un contraste nettement amélioré de ces particules fixées sur le plan d'image dans la surface du substrat.

Alors qu'à un temps d'intégration de 100 ms par image sur l'éclairage MS-TIRF, il est difficile de voir l'événement rapide d'une particule libre touchant la surface, en réduisant le temps d'intégration, nous pouvons visualiser l'effet «clignotant» des particules qui diffusent vers le bas et pénètrent dans le champ évanescent, devenant visibles un instant, afin de poursuivre rapidement leur chemin et en revenant à leur état sombre.

Enfin, en analysant l'image MS-TIRF dans 5.15 (d), nous pouvons obtenir la valeur maximale des pixels des particules fluorescentes lumineuses et l'écart-type du bruit de fond, ce qui donne un pic de rapport signal sur bruit (PSNR) supérieur à 700 (le PSNR obtenu sur une image TIRF traditionnelle de l'échantillon présenté à la figure 5.16 est de 295).

Afin d'exploiter le champ de vision exceptionnellement large offert par MS-TIRF, nous avons sélectionné des cellules souches mésenchymateuses (hMSC) dérivées de la moelle osseuse comme échantillon biologique immunocoloré pour les adhésions focales avec l'anticorps (AB) anti-paxilline et l'anti-IgG de lapin correspondante Atto 647N AB et enfin monté (c'est-à-dire encapsulé en milieu aqueux). La paxilline est une protéine intégrale des adhérences focales de la cellule, choisie intentionnellement en raison de ses rôles essentiels dans des processus biologiques importants tels que la motilité, la prolifération, la différenciation, la régulation de l'expression des gènes et la survie des cellules. L'anticorps primaire utilisé contre la paxilline réagit généralement aussi avec les cibles du cytosol, ce qui rend l'imagerie TIRF particulièrement utile (voir Figure 5.16). En culture, ces cellules peuvent atteindre plusieurs centaines de microns de diamètre, souvent bien au-delà du FOV des objectifs TIRF. Bien que les cellules fixes aient été l'option privilégiée pour cette première expérience biologique longue durée, aucune différence de performance n'est à prévoir pour les échantillons vivants du même type.

Avec l'échantillon biologique en place dans la configuration MS-TIRF, nous avons réussi à obtenir une série d'images à contraste élevé avec les hMSC immunocolorées ex-

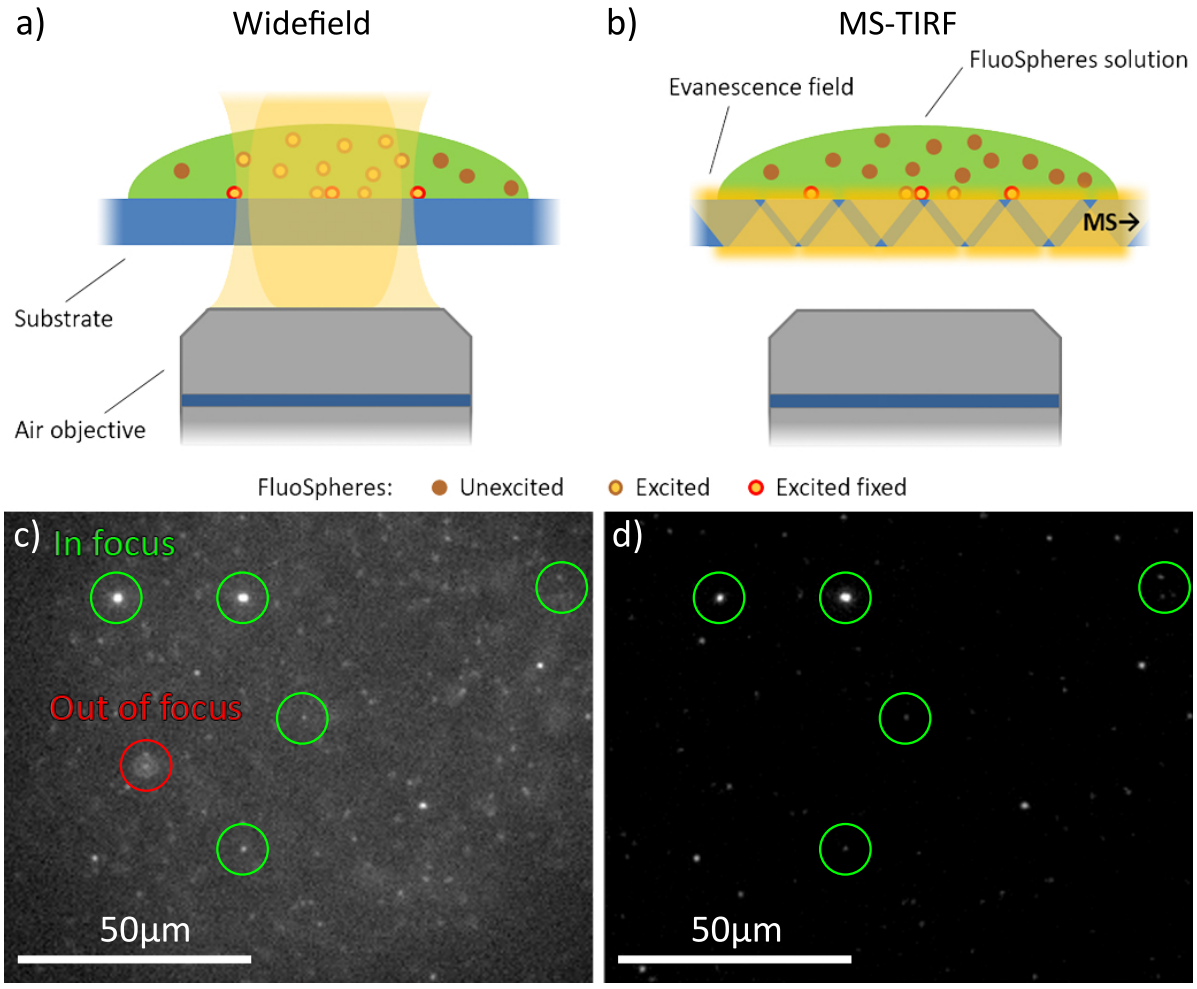

Figure 5.15 – Deux images consécutives d'une vidéo avant (**c**) et après (**d**) le changement d'éclairage WF à MS-TIRF en tant que source unique d'excitation pour les FluoSpheres de 0,2 µm. Temps d'intégration: 100ms / image. Alors que l'illumination WF nous permet de voir le mouvement rapide des particules diffusantes dans le volume de la gouttelette, il masque également partiellement les particules fixées dans la surface du verre. L'éclairage MS-TIRF parvient à exciter sélectivement ces microsphères fixées (et focalisées par l'objectif), éliminant ainsi la lumière de fond intense produite par les particules diffusantes. Avec des temps d'intégration plus courts sont également visible les particules qui heurtent la surface et clignotent un instant lorsqu'elles rentrent dans le champ évanescent.

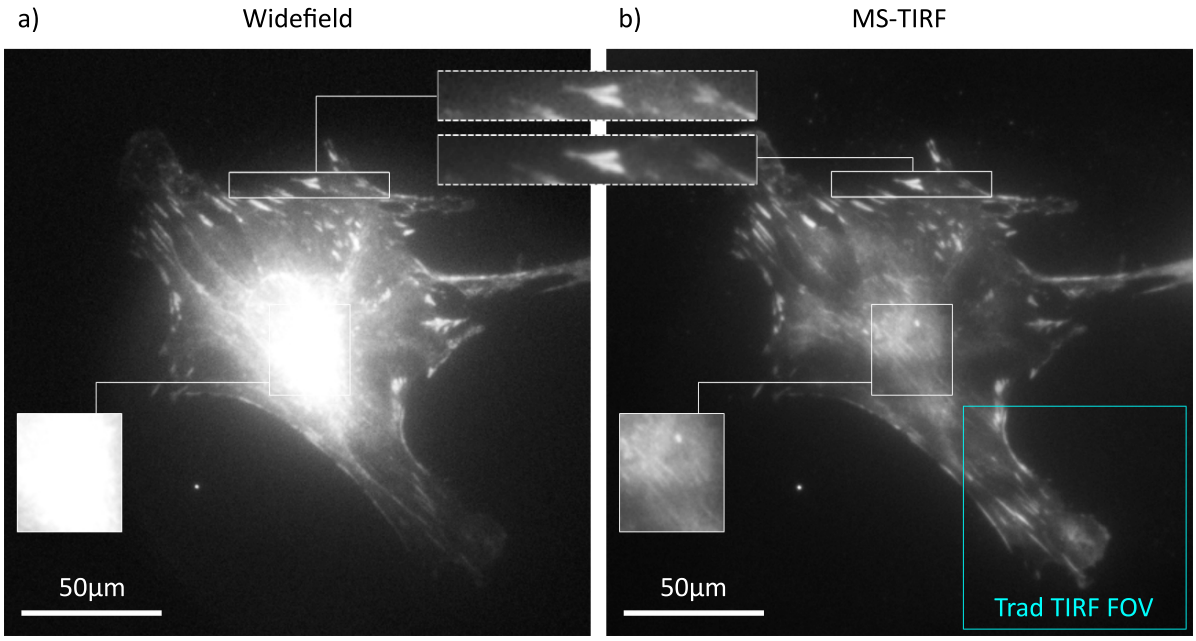

Figure 5.16 – Les hMSCs issues de la moelle osseuse immunocolorées dans les adhésions focales avec l'AB anti-paxilline et l'anti-IgG de lapin correspondante AB atto 647N, imagées avec (**a**) un microscope WF standard et (**b**) un substrat MS-TIRF. Lors de l'égalisation de l'intensité de l'image avec la luminosité des zones d'intérêt (cadres en pointillés en haut), la fluorescence de fond provenant du noyau de la cellule masque toute information de la membrane située dans cette région (centre dans (a) et (b)). Pour référence, le cadre bleu indique le champ de vision de 80 à 100 µm pouvant être atteint avec un objectif TIRF 100X typique.

clusivement excitées par le champ évanescent généré par la MS. De manière similaire au test avec FluoSpheres™, la section observable des cellules est réduite à une seule tranche mince se trouvant à proximité de la surface du verre, ce qui réduit considérablement la lumière de fond capturée par l'objectif à air. La figure 5.16 (b) est l'une de ces images, où il existe une nette distinction d'intensité entre les adhérences focales et le reste de la cellule. Bien que les adhérences focales aient une concentration plus élevée en fluorophores, Figure 5.16 (a) nous montre l'existence d'une concentration encore plus élevée dans le réticulum endoplasmatique autour du noyau de la cellule, pratiquement invisible sur l'image MS-TIRF, ce qui nous permet de voir des informations supplémentaires dans cette région.

Le produit SBP (Space-Bandwidth Product) est un moyen de quantifier la combinaison de la résolution et du FOV d'un objectif, ce qui peut également être traduit comme la quantité d'informations qu'il peut transmettre. Le SBP peut être exprimé comme la quantité minimale de pixels sur un capteur nécessaire pour capturer toute l'information fournie par la résolution et le FOV de l'objectif. Il peut être facilement calculé en divisant la surface du FOV par la surface d'un pixel requise pour obtenir un échantillonnage de Nyquist à la résolution donnée par la NA de l'objectif et la longueur d'onde d'éclairage. En utilisant la source laser et les objectifs décrits dans la figure 5.14, nous avons calculé un SBP de 2,2 mégapixels (100X NA1.49 FN = 22 FOV = 220 µm) et de 8,2 mégapixels (40X NA0,95 FN = 26,5 FOV = 660 µm), presque 4 fois plus d'informations en faveur de l'objectif de plus faible grossissement. Ce nombre pourrait atteindre 6 en utilisant un objectif à eau 40X NA 1.2, réduisant encore la différence

de résolution par rapport à un objectif TIRF traditionnel. Un tel élargissement du champ de vision et du SBP en TIRF pourrait être un atout précieux pour automatiser le processus d'imagerie de grands sujets ou en mouvement lent (par exemple, les cellules présentées dans ce travail), ainsi que pour les biopsies de grands spécimens.

5.6.5 Conclusions

Dans ce travail, nous avons introduit le concept de microscopie MS-TIRF. Nous avons conçu, fabriqué et testé expérimentalement des réseaux de métasurface TiO_2 capables de coupler jusqu'à 70% de la lumière transmise dans un premier ordre de diffraction, tout en supprimant considérablement la transmission directe, deux conditions importantes pour un puissant dispositif de couplage TIRF. Nous avons utilisé des microsphères fluorescentes pour vérifier l'illumination sélective de MS-TIRF et mesurer le rapport signal sur bruit obtenu, ce qui donne plus du double de celui d'une image similaire obtenue avec la TIRFM traditionnelle. Enfin, nous avons imagé des hMSCs issues de la moelle osseuse immunocolorées à l'aide de notre dispositif MS-TIRF et d'un objectif 40X à air, obtenant un contraste d'image très élevé avec un FOV neuf fois supérieur à celui des systèmes TIRF traditionnels et un facteur SBP maximal également quatre fois supérieur. En conclusion, nous avons montré que les substrats avec des métasurfaces en TiO_2 constituaient une alternative puissante aux objectifs à forte NA, qui étendaient les capacités de la microscopie TIRF moderne. La grande flexibilité de la conception des MSs pourrait également permettre des fonctionnalités de conception plus avancées permettant de remédier aux faiblesses communes de l'imagerie TIRF, telles que l'homogénéité du champ d'excitation, améliorant encore l'avantage du MS-TIRF par rapport aux techniques existantes.

Titre : Métasurfaces pour la bioimagerie

Mots clés : TIRF,MS-TIRF,Métasurface,Bioimagerie,Microscopie,Nanotechnologie

Résumé : Au cours des dernières années, des efforts importants ont été déployés pour développer des métasurfaces (MSs) électromagnétiques avec la possibilité de changer de manière abrupte les propriétés de la lumière. Ces avancées ont ouvert une nouvelle gamme de possibilités pour contrôler la lumière en utilisant des dispositifs optiques ultra-minces. Dans ce contexte, et plus spécifiquement dans le spectre visible,les applications en bio-imagerie s'avèrent particulièrement intéressantes. Une technique qui est particulièrement bien adaptée à l'étude de molécules proches d'une membrane cellulaire est la microscopie à fluorescence par réflexion interne (TIRFM), qui repose sur un champ évanescent d'excitation. Dans ce cas la lumière incidente est totalement réfléchie sur une interphase (généralement verre/eau) en raison de son angle d'incidence élevé. À ce jour, la TIRFM est généralement mise en œuvre à l'aide d'objectifs volumineux de grande ouverture numérique et de petit champ de vision. Dans ce travail de thèse, nous réalisons de substrats pour la microscopie TIRF à base de métasurfaces constituées de réseaux périodiques de structures asymétriques fabriquées en dioxyde de titane(TiO2) sur du verre borosilicaté. Ces structures, qui ne mesurent que 48 nm, ont été optimisées à l'aide de simulations numériques "Rigorous coupled-wave analysis" (RCWA) dans le but de coupler de 50 à 90% de la lumière incidente dans le premier ordre de diffraction avec des angles élevés ($\theta > 63°$). Le fait de pouvoir utiliser des objectifs de faible grossissement et d'avoir une grande zone de champ évanescent fournit des conditions TIRF uniques qui ne sont pas accessibles avec les méthodes traditionnelles. De plus, ces structures sont compatibles avec la lithographie par nanoimpression UV, ce qui permet d'envisager une fabrication à bas coût et à grande échelle. Outre la conception, et la fabrication, dans cette thèse nous aboutissons à une preuve de principe de la microscopie TIRF basée sur des metasurfaces en milieu biologique en imageant notamment des membranes fluorescentes de cellules souches. Ces métasurfaces permettent ainsi l'implémentation TIRFM à contraste élevé et à faible photo-blanchissement compatible avec des microscopes à champ large peu coûteux.

Title : Metasurfaces for bioimaging

Keywords : TIRF,MS-TIRF,Metasurface,Bioimaging,Microscopy,Nanotechnology

Abstract : In recent years there has been a significant effort to push electromagnetic metasurfaces with the ability to abruptly change light properties into visible wavelengths. These advancements have opened a new range of possibilities to reshape light using ultra-thin optical devices and there is one field that is starting to gather attention: bioimaging. One technique particularly well suited for the study of molecules near a cell membrane is Total Internal Reflection Fluorescence (TIRF) microscopy, which relies on an evanescence field created by light being totally internally reflected within a glass substrate due to its high incidence angle. As of today, TIRF is generally implemented using bulky high-NA, small field of view oil objectives. In this project we present the realization of metasurface-based TIRF microscopy substrates consisting of periodic 2D arrays of asymmetric structures fabricated in titanium dioxide on borosilicate glass. These patterns, as small as 48nm, were optimized through rigorous coupled-wave analysis to couple 50-90% of the incoming normally incident light into the first diffraction order, which outputs at an angle that suffices total internal reflection in water and eliminates the requirement for high NA objectives or prisms to achieve TIRF. Being able to utilize lower magnification air objectives and having a large evanescence field area provide unique TIRF conditions not accessible by traditional methods. Additionally, these structures are compatible with soft UV nanoimprint lithography, for cost-effective scale production, to give TIRF's high contrast, low photodamage and low photobleaching capabilities to inexpensive wide-field microscopes